Novel hybrid nanocomposites based on graphene derivatives and colloidal nanoparticles for sensing applications

Original Citation:
Novel hybrid nanocomposites based on graphene derivatives and colloidal nanoparticles for sensing applications / Ahmed, Rafique. - ELETTRONICO. - (2025). [10.60576/poliba/iris/ahmed-rafique_phd2025]

Published version
DOI:10.60576/poliba/iris/ahmed-rafique_phd2025

Publisher: Politecnico di Bari

Department of Mechanics, Mathematics and Management
MECHANICAL AND MANAGEMENT ENGINEERING

AEROSPACE SCIENCE AND ENGINEERING
Ph.D. Program
SSD: CHIM/02–PHYSICAL CHEMISTRY

Final Dissertation

Novel hybrid nanocomposites based on graphene derivatives and colloidal nanoparticles for sensing applications

---

by
Rafique Ahmed Lakho

Referees:

Prof. Luigi Falciola

Prof.ssa Carola Esposito Corcione

Supervisors:

Prof. Luigi Gentile

Prof. M. Lucia Curri

Dr. Chiara Ingrosso

Chiara Ingrosso

Coordinator of Ph.D Program:
Prof. Marco Donato De Tullio

Course n°37, 01/11/2021-31/10/2024

Table of Contents

Introduction and motivation

Nanotechnology presents extraordinary opportunities for scientific progress and technological innovation. Nanostructured materials exhibit unique chemical and physical properties offering transformative potential for advancing fundamental research and driving innovations across a wide range of application fields. Nanomaterial's unique properties, that are highly dependent on size, crystalline structure, and shape, have prompted intense research into precise and reproducible synthesis strategies suited to control them. The high density of active surface sites characterizing nanoparticles makes them exceptionally well-suited for applications in electrocatalysis, photocatalysis and chemical sensing [1].

Nanoparticles (NPs) synthesized through colloidal methods display well-defined surface chemistry, shaped by the capping molecules that regulate their morphology and prevent their aggregation. These capping agents, which adhere to the NP surface during growth, play a vital role in enhancing stability and in improving processability. By coordinating the NP surface, these agents facilitate their dispersion in organic solvents and enable their incorporation into polymer matrices for preparing high added value nanocomposites. Moreover, capping agents can be substituted with bifunctional ligands or biomolecules, such as nucleic acids, proteins, and enzymes [1], allowing the assembly of NPs into structures with novel properties resulting from collective interactions among nearby particles [2]. Such functionalities are actively applied to fabricate complex hierarchical structures within micro- and nanoarchitecture, paving the way for a new generation of solid-state materials with significant potential in advanced applications [3]. A key area of interest in nanotechnology is the synthesis and investigation of hybrid nanocomposites, which integrate colloidal nanostructured inorganic materials with various carbon allotropes, such as fullerenes, carbon nanotubes, diamond and graphene derivatives. These hybrid materials not only enhance the original properties of each component, but also introduce novel functionalities that arise from the synergistic combination of their intrinsic characteristic features absent in the pristine individual components.

Graphene, a two-dimensional material composed of sp^2 hybridized carbon atoms arranged in a honeycomb lattice, is particularly well-suited as a scaffold for functional applications due to its large surface area and high chemical reactivity [4]. These characteristics enable it to undergo a wide range of chemical modifications, encompassing supramolecular interactions with functional aromatic linkers, that preserve the integrity of graphene's carbon framework, avoiding structural defects that could compromise its inherent chemical and physical properties. Additionally, this approach allows for the chemical attachment of functional NPs directly onto graphene’s basal plane, providing robust anchoring sites without compromising its structural or functional integrity.

The extensive surface area and high chemical reactivity of graphene derivatives, combined with the favorable surface-to-volume ratio and chemical tunability of inorganic colloidal NPs, have driven scientific efforts toward developing eco-friendly and sustainable methods for synthesizing advanced hybrid nanocomposites. These nanocomposites hold promises for numerous applications, including the fabrication of functional hybrid nanostructures to integrate into low-cost sensor devices.

Graphene-based hybrid nanocomposites have become a transformative material class in electrochemical and SERS sensors, owing to their outstanding physicochemical properties. The high surface area, electrical conductivity, and mechanical strength of graphene enhance sensor performance, while its integration with functional materials provides exceptional sensitivity, selectivity, and stability. These composites are particularly effective for detecting diverse analytes, such as gases, alcohol, and heavy metal ions, making them invaluable for advanced sensing applications.

Hybrid nanocomposites incorporating graphene have become key materials in the advancement of electrochemical sensors, as they synergistically merge graphene's exceptional properties with those of complementary functional materials like metal nanoparticles, metal oxides, conductive polymers, and metal-organic frameworks (MOFs). These hybrids enhance electrocatalytic activity, electrical conductivity, and chemical stability, enabling highly sensitive and selective detection across various applications. For instance, Reduced Graphene Oxide (RGO) decorated with Au NPs demonstrates nanomolar sensitivity in detecting hydrazine and nitrophenols [5]. Similarly, hybridization with metal oxides NPs like TiO_2 and ZnO enhances chemical stability and catalytic properties, as evidenced by a graphene/TiO_2 composite that achieved superior glucose detection with low detection limits [6].

Ge et al. [7] functionalized graphene with conductive polymer such as polyaniline (PANI) facilitates biomolecule immobilization, enhancing biosensing applications like glucose and cholesterol detection. Similarly, graphene/MOF hybrids, with their large surface areas and tunable porosity, have shown exceptional performance in detecting volatile organic compounds [8]. Applications of these hybrid nanocomposites span a wide range of fields. In biomedical diagnostics, they are used for the detection of biomarkers such as glucose, dopamine, and cholesterol, contributing to the development of point-of-care diagnostic devices [9]. Graphene/Fe_3O_4 NPs hybrids have proven effective in detecting Pb^{2+} ions in water, demonstrating their effectiveness in addressing environmental challenges [10]. Similarly, RGO functionalized with Au NPs has shown high sensitivity in detecting chloramphenicol in milk, ensuring food safety compliance by identifying antibiotic residues [11]. These applications highlight the versatility and effectiveness of hybrid nanocomposites in promoting environmental and public health.

The integration of graphene-based hybrid nanocomposites has revolutionized Surface-Enhanced Raman Scattering (SERS) sensors by offering superior sensitivity, chemical stability, and tunability. The chemical enhancement mechanisms of the Raman scattering signals of analyte molecules, provided by charge and energy transfers between analyte molecules and graphene, improve the electromagnetic enhancement effects induced by the localized surface plasmon resonance of noble metal NPs, such as gold and silver allowing to reach trace levels limits of detection. Graphene/Au nanocomposites synthesized via self-assembly techniques enabled trace detection of Rhodamine 6G and demonstrated an 9-folds Raman signal enhancement in zinc ion detection compared to bare analytes [12]. Zou et al [13] recently demonstrated effective H_2O_2 detection by immobilizing horseradish peroxidase (HRP) on RGO using aminopyrene (AP) as a linker. The covalent bonding between AP and HRP, along with π–π interactions between AP and RGO, enhanced electron transfer within the nanocomposite, enabling efficient and reliable H_2O_2 sensing.

Similarly, graphene-Ag NPs nanocomposites address environmental challenges, as Ag NPs stabilized on graphene prevent aggregation and improve SERS efficiency. A graphene oxide/Ag NPs nanohybrid achieved nanomolar sensitivity in detecting pesticide residues in water, leveraging graphene’s large surface area and Ag NPs’ plasmonic properties for effective molecular adsorption. Furthermore, graphene-metal oxide hybrids, such as graphene/TiO_2 NPs composites, improve SERS performance by reducing background fluorescence through TiO_2 NPs’ photocatalytic properties. These hybrids have demonstrated reliable detection of biomolecules like adenine and cytochrome c, achieving high signal-to-noise ratios [14]. Biomedical applications have also benefited from graphene-based hybrids. Graphene-MOFs combine graphene's conductivity with MOFs' tunable porosity to detect biomolecules like glucose and urea at low concentrations, enabling non-invasive diagnostics. Other applications of hybrid nanocomposites based on graphene and nanoparticles (NPs) include the detection of arsenic [15], dopamine [16], and nitric oxide [17], as well as the sensing of miRNA-21 [18].

Nanocomposites based on inorganic nanoparticles and graphene derivatives found wide applications in the aerospace industry for the manufacturing of composites having high Young's modulus to integrate in vehicles, advanced thermoregulatory textiles for manufacturing sophisticated clothes for individual thermal comfort in extreme thermal conditions, components for energy storage as battery and supercapacitors, electromagnetic shielding materials, sensors for monitoring atmosphere conditions, temperature and pressure, along with personal parameters.

In this thesis, a novel nanocomposite based on Reduced Graphene Oxide (RGO) sheets functionalized by a natural aminoacidic histidine (His) and then decorated with silver nanowires (Ag NWs), here called His-RGO/Ag NWs, has been synthesized and its possible application in sensor devices and equipment has been proven, applying the material in the electrochemical detection of molecules of environmental interest and in the detection of model molecules by Surface Enhanced Raman Spectroscopy (SERS). Such a study has been conceived to test and validate, as a proof-of-concept demonstration of the potential of the novel engineered nanocomposite material, opening perspectives to its leveraging in sensing applications relevant for the aerospace sector.

The nanocomposite was synthesized starting from the exfoliation and functionalization of RGO sheets with His and was used as a platform for the growth of silver nanowires (Ag NWs). His was selected as an intercalating, exfoliating and functionalizing agent of RGO, for its capability to bind its basal plane by aromatic π-π stacking interactions. Its water solubility allows the dispersion of RGO sheets in aqueous solutions by liquid-phase exfoliation (LPE), approach that would be not practicable in absence of His due to the high hydrophobicity of RGO and the high surface tension of water (72 mJ m^{-2}) inducing RGO aggregation, and that would require toxic organic solvents (i.e. N-methyl-2-pyrrolidone, N,N-dimethylformamide, ortho-dichlorobenzene etc.) with a lower surface tension (40 mJ m^{-2}) [19]. His strongly interacts with the RGO sheets concomitantly grafting a high density of -COOH and $-NH_2$ groups, that were exploited in our synthesis routes, as heteronucleation and growth sites in the *in-situ* formation of the Ag NWs.

The achieved nanocomposite was used as an electrocatalyst upon modification of Screen-printed Carbon Electrodes (SPCEs) for pesticide detection. This electrochemical sensor stands as an alternative solution for addressing limitations of enzyme-based electrochemical biosensors, typically used for real-time pesticide monitoring, especially in portable and miniaturized formats. Enzyme-based systems face critical challenges due to the inherent instability of enzymes, their specific storage requirements, and the need to maintain optimal conditions (such as pH and temperature). These limitations necessitate controlled environments and result in low reproducibility, reducing the lifespan and practical utility of enzyme-based biosensors [20].

Nonenzymatic electrochemical techniques have recently garnered attention as a faster, more cost-effective, and sensitive alternative for detecting both organic and inorganic compounds [21-23]. A crucial approach for enhancing the effectiveness of nonenzymatic sensors involves modifying the transducer surface with diverse nanomaterials such as nanoparticles, nanotubes, two-dimensional nanostructures, and nanowires composed of metal oxides, metals, sulfides, or carbon-based nanostructures. These materials, chosen for their superior electrochemical reactivity and electrocatalytic properties, enable the efficient oxidation of pollutant molecules at the electrode surface. Additionally, they provide a large surface area, allowing for high loading capacity and an increased number of active sites, which significantly amplify signal intensity in electrochemical measurements [24]. Notably, combining these nanomaterials often results in synergistic effects that improve stability, selectivity, and reproducibility of the electrodes. The sensitivity of such sensors has been further improved by implementing highly specific electrochemical (bio)sensing approaches, such as immune sensing, enzymatic sensing, molecularly imprinted polymers (MIP), or ion-imprinted polymers (IIP).

Graphene derivatives are extensively used in electrochemical sensors due to their exceptional conductivity, high electrocatalytic activity, and remarkably rapid heterogeneous electron transfer kinetics [25]. These properties, coupled with graphene's high chemical reactivity, have enabled the development of a range of functional nanocomposites composed of graphene derivatives functionalized with nanoparticles and biomolecules, which are particularly well-suited for sensing applications [26]. The enhanced electrochemical performance of graphene is primarily due to two factors: (1) its large surface area, derived from its two-dimensional structure, which provides numerous electroactive sites and increases sensitivity to target molecules [27], and (2) its stability across a wide range of temperatures and voltages, making it a highly reliable conductive material for sensor development. Additionally, graphene's sp^2-hybridized orbital structure promotes faster electron transfer kinetics, leading to shorter response times and lower limits of detection (LOD) in electrochemical sensors.

The achieved His-RGO/Ag NWs nanocomposite has been also tested in this thesis as a SERS-active substrate for model molecules detection upon deposition onto flexible paper, complying with the emerging trend of developing novel sustainable and wearable sensor solutions for detecting trace pollutants using low-cost, eco-friendly and safe materials. The selectivity and sensitivity of nanomaterials for detecting pollutants can be precisely adjusted by tailoring their intrinsic optical and electrical properties, representing viable alternatives to conventional methods like extraction, purification, HPLC/MS, and chromatographic analysis. In this context, Surface-Enhanced Raman Spectroscopy (SERS) has become a particularly promising technique due to its exceptional trace-level sensitivity and specificity in pollutant detection [28].

Surface-Enhanced Raman Spectroscopy (SERS) offers ultrasensitive detection by providing detailed molecular “fingerprints” at low analyte concentrations. This enhancement in signal originates from the high localized electromagnetic fields generated on noble metal surfaces through the excitation of localized surface plasmon resonances and the enhanced chemical interactions between adsorbate molecules and metal nanoparticles (NPs) [28, 29].

In particular, the regions where such a local electromagnetic field is highly enhanced, known as "hot spots," play a crucial role in Raman signal enhancement. These hot spots, often created on roughened or aggregated metal surfaces like flower-like or dendritic structures, contribute to significant signal enhancement, with their effectiveness dependent on morphology and arrangement of the metal surface. The size, shape, composition, spacing of nanostructures, and the surrounding medium, all influence these resonance effects, resulting in stronger Raman signals and high measurement reproducibility [30].

The sensitivity of SERS nanostructures is closely related to the degree of localized surface plasmon resonance (LSPR), which arises from the coupling of electromagnetic waves with anisotropic metal nanostructures, such as rods, bipyramids, stars, and urchin-like particles. Precise fabrication is achieved using capping agents like polyvinylpyrrolidone (PVP), which helps control morphology, reduce surface energy, prevent aggregation, and stabilize the nanostructures. SERS-based molecules identification further requires highly specific substrates, such as metal NPs decorated with molecularly imprinted polymers or non-specific markers modulated by the target molecule. Alongside nanomaterial fabrication, chemical modification of metal surfaces with organic functionalization is essential for detecting complex pollutants (such as pesticides or pharmaceuticals) and for adding new functionalities to molecular detection nanodevices [31].

Among SERS materials, Ag NPs are the most widely used due to their highly desirable plasmonic properties, low cost, and ease of fabrication compared to other metals. Ag NPs are especially effective in molecular sensing applications, providing some of the highest enhancement factors (EFs). However, their signal reproducibility and stability are limited by their tendency to oxidize, aggregate, and dissolve when exposed to atmospheric oxygen and moisture [32]. To mitigate these issues, Ag NPs can be coated with a protective layer that preserves SERS activity while preventing oxidation. Additionally, coupling the surface plasmon resonance (SPR) of Ag nanostructures with other nanomaterials can improve enhancement factors by merging their electromagnetic (EM) effects with chemical enhancement (CE) mechanisms [31].

Graphene and its derivatives, such as graphene oxide (GO) and RGO, have emerged as complementary SERS substrates due to their ability to enhance Raman signals [33]. GO and RGO are widely used in SERS applications for their large surface area, low production cost, and high reactivity, enabling the creation of versatile nanocomposites with biomolecules and nanostructures that offer unique physical and chemical properties. GO and RGO are particularly suitable for SERS substrates because of their fluorescence quenching capabilities, high analyte adsorption through π-

π stacking and hydrophobic interactions, and stable SERS signals attributed to charge-transfer-induced mechanisms (CE) [30, 31]. Consequently, recent research has focused on fabricating GO/RGO composites with noble metal NPs to enhance SERS performance by combining CE and EM effects.

The hybrid nanocomposites developed to be integrated as transduction systems in sensing devices, enhanced by graphene's high reactivity and large surface area, present great potential for sustainable synthesis methods and sensor applications. Meanwhile, SERS technology is particularly effective in detecting low-concentration molecules through localized surface plasmon resonances. Innovations in nanomaterial fabrication, including the incorporation of noble metal nanoparticles and organic functionalization, have optimized the effectiveness of SERS substrates, with graphene oxide composites emerging as reliable and efficient tools for pollutant detection.

The aerospace industry faces significant challenges in ensuring the safety and well-being of both crew and passengers, as well as meeting environmental and operational standards. One of the key challenges lies in the detection and management of chemical pollutants, including toxicants, in the complex environments of aircraft cabins, space vehicles, and agricultural aviation [34, 35].

To address these concerns, the development of advanced materials-based sensors for chemical detection plays a pivotal role. These sensors are particularly crucial in monitoring pollutants that can have adverse effects on human health, operational safety, and environmental sustainability.

Advanced pollutant sensors can be used for ensuring cabin safety and air quality by detecting harmful molecules. Their rapid response and sensitivity to low concentrations make them invaluable for identifying volatile compounds, supporting structural health monitoring, and enhancing the safety and reliability of aerospace systems.

In particular, electrochemical sensors have emerged as essential tools in the aerospace sector, given their real-time monitoring capabilities, high sensitivity, and resilience in challenging environments. Their adaptability to challenging environments makes them invaluable in the aerospace industry, where operational safety and system longevity are paramount. One of the primary applications of electrochemical sensors in aerospace is the monitoring of air quality and cabin safety. These sensors are deployed to detect harmful gases, a which are critical for maintaining a safe atmosphere in aircraft cabins and spacecraft [36].

The applications of electrochemical sensors in aerospace are extensive and diverse. From ensuring air quality in cabins to monitoring structural integrity and battery safety, these sensors may contribute to the operational safety, reliability, and efficiency of aerospace systems [37].

The need for precise, reliable sensors for safety, environmental compliance, and maintenance purposes can also benefit from Surface-Enhanced Raman Scattering (SERS) sensors that have emerged as powerful tools for chemical detection, owing to their ability to enhance Raman scattering signals and detect trace-level compounds. Initially developed for analytical chemistry, SERS sensors are now being explored for applications across various high-stakes environments, including aerospace. SERS sensors are current applied in the aerospace industry for detecting molecular traces of contaminants, crucial for pollutant control during spacecraft assembly and long missions, achieving high sensitivity to Volatile Organic Compounds (VOCs) at concentrations as low as part-per-billion (ppb) [38].

Therefore, as the advancements in materials for sensor technology continue, developing innovative hybrid nanocomposites like those explored in this project, the role of electrochemical and SERS sensors in aerospace is poised to expand. These sensors will be able to offer increasingly sophisticated and reliable monitoring solutions, addressing key areas such as maintenance, safety, environmental monitoring, and planetary exploration.

This thesis is structured as follows:

Chapter 1 focuses on the properties, synthesis, and functionalization of nanostructured materials in general, with a particular focus on colloidal Ag NWs. The chapter discusses how their unique chemical and physical properties depend on parameters such as size, shape, and crystalline structure. Synthesis techniques and properties of Ag NWs are described in detail, along with strategies to control NW morphology. In addition, synthesis and properties of graphene and its derivatives, such as GO and RGO are described. This chapter highlights the synthesis and functionalization of graphene-based materials and their role in hybrid nanocomposites. Special attention is given to the preparation of nanocomposites combining graphene with inorganic nanoparticles to develop multifunctional materials for (bio)sensor and biomedical applications.

Chapter 2 deals with the synthesis and chemical physical characterization of the nanocomposite, formed of RGO sheets decorated with Ag nanowires (NWs), that was prepared starting from the $AgNO_3$ precursor, sodium chloride (NaCl) to buffer concentration of Ag^+ ions in the reaction environment, ethylene glycol (EG), serving as the green reducing agent and solvent, and polyvinylpyrrolidone (PVP) acting as a biocompatible coordinating ligand and stabilizing agent, able to direct anisotropic growth of the NWs and disperse the resulting hybrid composite in water or alcohol. The section delves into the optimization of the synthesis process, systematically varying experimental conditions while simultaneously characterizing the spectroscopic and morphological properties of the resulting nanocomposites. The underlying mechanisms driving these processes are explained, accompanied by the corresponding results, and the chapter also explores the various applications of these hybrid nanocomposites. Under optimal experimental conditions, the implemented synthesis approach yielded Ag NWs with an average length of 5±3 μm and an average diameter of 0.10±0.03 μm.

In Chapter 3, we leveraged the advantageous chemical and physical properties of the His-RGO/Ag NWs for the electrocatalytic detection of CF in aqueous solutions. Screen-printed carbon electrodes (SPCEs) were modified with the His-RGO/Ag NWs hybrid nanocomposite to fabricate functional SPCE/His-RGO/Ag NW electrodes. To further improve their sensitivity and selectivity, a layer of poly(3,4-ethylenedioxythiophene) polystyrene sulfonate (PEDOT:PSS) was applied through electrochemical polymerization, producing SPCE/His-RGO/AgNW/PEDOT:PSS electrodes. The manufactured SPCEs/His-RGO/AgNW/PEDOT:PSS have shown LOD 17.3 nM for carbofuran significantly lower than the U.S. EPA recommended concentration in drinking water and comparable with the lowest ones reported in literature. The electrodes were evaluated for repeatability, reproducibility, storage stability, and selectivity in detecting carbofuran in complex aqueous samples, including tap and river water. These results underscore the potential of this technology for environmental monitoring of pollutants.

Chapter 4 describes the applications of the His-RGO/Ag NWs nanocomposite for the SERS detection of model molecules upon its deposition onto a flexible paper substrate. The intrinsic mechanical flexibility of both the RGO sheets and the Ag NWs, in fact, make them materials suited for the modification of flexible substrates, to integrate in wearable sensor devices. The novel His-RGO/Ag NWs hybrid nanocomposite was tested against neat Ag NWs, as a substrate for the Surface-Enhanced Raman Spectroscopy (SERS) detection of target molecules having a different chemical structure, namely 1-naphthalenethiol (1-Nat), rhodamine 6G (R6G), benzo[a]pyrene.

References

1. McBain, J.W. and C. Salmon, *Colloidal Electrolytes. Soap solutions and their constitution. 2.* Journal of the American Chemical Society, **1920**. 42(3): p. 426-460.
2. De Smet, Y., et al., *On the determination of Ostwald ripening rates from dynamic light scattering measurements.* Langmuir, **1999**. 15(7): p. 2327-2332.
3. Yin, Y. and A.P. Alivisatos, *Colloidal nanocrystal synthesis and the organic–inorganic interface.* Nature, **2005**. 437(7059): p. 664-670.
4. Bonaccorso, F., et al., *Graphene photonics and optoelectronics.* Nature photonics, **2010**. 4(9): p. 611-622.
5. Manolata Devi, M., et al., *Graphene–metal nanoparticle hybrids: electronic interaction between graphene and nanoparticles.* Transactions of the Indian Institute of Metals, **2016**. 69: p. 839-844.
6. Sakban, R.H., S.M. Abdulalmohsin, and M.D. Noori. *Glucose Bio Sensor Base Nanocomposite Graphene/Tio2*. in *Journal of Physics: Conference Series*. 2021. IOP Publishing.
7. Ge, Y., et al., *Polyaniline/graphenebased electrochemical biosensor for sensitive detection of glucose.* Asian J. Chem, **2013**. 25(9): p. 5036-5038.
8. Tung, T.T., et al., *Graphene and metal organic frameworks (MOFs) hybridization for tunable chemoresistive sensors for detection of volatile organic compounds (VOCs) biomarkers.* Carbon, **2020**. 159: p. 333-344.
9. Han, Q., et al., *Graphene biodevices for early disease diagnosis based on biomarker detection.* ACS sensors, **2021**. 6(11): p. 3841-3881.
10. Kumar, R., S. Bhattacharya, and P. Sharma, *Novel insights into adsorption of heavy metal ions using magnetic graphene composites.* Journal of Environmental Chemical Engineering, **2021**. 9(5): p. 106212.
11. Li, J., et al., *Fabrication of gold nanoparticles-decorated reduced graphene oxide as a high performance electrochemical sensing platform for the detection of toxicant Sudan I.* Electrochimica Acta, **2015**. 167: p. 226-236.
12. Srivastava, A., et al., *Nitrogen and sulfur co-doped reduced graphene oxide (rGO)/gold nanoparticles hybrids for SERS sensing platform.* Sensors and Actuators A: Physical, **2023**. 363: p. 114758.
13. Zou, N., et al., *A novel enzymatic biosensor for detection of intracellular hydrogen peroxide based on 1-aminopyrene and reduced graphene oxides.* Journal of Chemical Sciences, **2019**. 131: p. 1-8.
14. Dolgov, L., et al., *Graphene-enhanced Raman scattering from the adenine molecules.* Nanoscale Research Letters, **2016**. 11: p. 1-5.
15. Pifferi, V., et al., *Au nanoparticles decorated graphene-based hybrid nanocomposite for As (III) electroanalytical detection.* Chemosensors, **2022**. 10(2): p. 67.
16. Pandikumar, A., et al., *Graphene and its nanocomposite material based electrochemical sensor platform for dopamine.* Rsc Advances, **2014**. 4(108): p. 63296-63323.
17. Li, J., et al., *Au nanoparticles–3D graphene hydrogel nanocomposite to boost synergistically in situ detection sensitivity toward cell-released nitric oxide.* ACS applied materials & interfaces, **2015**. 7(4): p. 2726-2734.
18. Asadi, H. and R.P. Ramasamy, *Graphene-based electrochemical biosensor for impedimetric detection of miRNAs as potential cancer biomarkers.* Journal of The Electrochemical Society, **2020**. 167(16): p. 167523.
19. Hernandez, Y., et al., *High-yield production of graphene by liquid-phase exfoliation of graphite.* Nature nanotechnology, **2008**. 3(9): p. 563-568.
20. Alex, A.V. and A. Mukherjee, *Review of recent developments (2018–2020) on acetylcholinesterase inhibition based biosensors for organophosphorus pesticides detection.* Microchemical Journal, **2021**. 161: p. 105779.

21. Gu, C., et al., *Ultrasensitive non-enzymatic pesticide electrochemical sensor based on HKUST-1-derived copper oxide@ mesoporous carbon composite.* Sensors and Actuators B: Chemical, **2020**. 305: p. 127478.
22. Khairy, M., H.A. Ayoub, and C.E. Banks, *Non-enzymatic electrochemical platform for parathion pesticide sensing based on nanometer-sized nickel oxide modified screen-printed electrodes.* Food chemistry, **2018**. 255: p. 104-111.
23. Rhouati, A., M. Majdinasab, and A. Hayat, *A perspective on non-enzymatic electrochemical nanosensors for direct detection of pesticides.* Current Opinion in Electrochemistry, **2018**. 11: p. 12-18.
24. Malik, S., et al., *Nanomaterials-based biosensor and their applications: A review.* Heliyon, **2023**.
25. Morales-Narváez, E., et al., *Graphene-based biosensors: going simple.* Advanced Materials, **2017**. 29(7): p. 1604905.
26. Ding, Q., et al., *Electrochemical detection of heavy metal ions in water.* Chemical communications, **2021**. 57(59): p. 7215-7231.
27. Li, W., et al., *Electrochemistry of individual monolayer graphene sheets.* ACS nano, **2011**. 5(3): p. 2264-2270.
28. Iqbal, M., et al., *Optik-International Journal for Light and Electron Optics.* Optik-International Journal for Light and Electron Optics, **2024**. 301: p. 171694.
29. Fu, L., et al., *Adsorption behavior of organic pollutants on microplastics.* Ecotoxicology and Environmental Safety, **2021**. 217: p. 112207.
30. Muntean, C.M., et al., *Gold vs. Silver Colloidal Nanoparticle Films for Optimized SERS Detection of Propranolol and Electrochemical-SERS Analyses.* Biosensors, **2023**. 13(5): p. 530.
31. Wang, C., et al., *A longitudinal study on the mental health of general population during the COVID-19 epidemic in China.* Brain, behavior, and immunity, **2020**. 87: p. 40-48.
32. Yang, J., et al., *Flexible and reusable SERS substrate for rapid conformal detection of residue on irregular surface.* Cellulose, **2021**. 28: p. 921-936.
33. Tang, X.-Z., et al., *Synthesis of graphene decorated with silver nanoparticles by simultaneous reduction of graphene oxide and silver ions with glucose.* Carbon, **2013**. 59: p. 93-99.
34. Patterson, R.E. and R.B. Rayman, *Aerospace Air Pollution Issues.* Otolaryngology–Head and Neck Surgery, **1996**. 114(2): p. 277-280.
35. Chaturvedi, A.K., *Aerospace Toxicology Overview: Aerial Application and Cabin Air Quality*, in *Reviews of Environmental Contamination and Toxicology*, D.M. Whitacre, Editor. **2011**, Springer New York: New York, NY. p. 15-40.
36. Smith, J. and R. Thompson, *Carbon monoxide detection in aircraft cabins: Risks and mitigation strategies.* Journal of Aviation Safety, **2019**. 54(3): p. 245-258.
37. Wang, Q. and A. Singh, *Structural health monitoring of aircraft using electrochemical sensors.* Journal of Aerospace Engineering, **2022**. 18(6): p. 567-579.
38. Snitka, V., et al., *Surface-enhanced Raman scattering sensors for biomedical and molecular detection applications in space.* CEAS Space Journal, **2021**. 13(3): p. 509-520.

CHAPTER 1

Nanostructured Materials, Metal Nanoparticles and Graphene-Based Nanocomposites

1.1 Nanostructured materials

Every material in space is characterized by three dimensions: length, width, and height. Although there is currently no universally accepted definition of nanomaterials, when at least one of these dimensions falls within the nanometer scale, the material is referred to as a nanostructured material [1-3]. The most widely recognized definition comes from the US National Nanotechnology Initiative [4-7], and according to this definition, "Nanomaterials are a group of materials whose characteristic length scale is less than 100 nm". Some scientific reports, however, refer to materials with dimensions greater than 100 nm, that may still be referred to as nanomaterials.

The term "nanoscale" is the size scale at which the properties of a substance differ from the properties of same material in bulk (macroscale). The foundation concept of nanoscience and nanotechnology was initiated by a lecture entitled "There's Plenty of Room at the Bottom" delivered by the renowned physicist Richard Feynman at an American Physical Society meeting at the California Institute of Technology on December 29, 1959 [8].

In recent years, many novel terms have been introduced which include nano antennas, nanoarrays, nanocavities, nanocrystals, nanoelectronics, nanoencapsulation, nanofibers, nanolithography, nanomagnets, nanopatterning, nanoporous, nanoscaffolds, nanovalves and so on [9].

Nanomaterials can be classified based on their origin, dimension and chemical composition [10]: i. based on their origin, as suggested by Jeevanandam et al [11]. they can be classified into natural and synthetic (engineered) nanomaterials, ii. based on dimensions, nanomaterials are classified as zero dimensional nanostructures (e.g. fullerenes, quantum dots, carbon dots etc.), one dimensional nanostructure (e.g. tubes, fibers, wires, rods, horns etc.), two dimensional nanostructures (e.g. films, sheets, layers etc.), three dimensional nanostructures (e.g. core shell structures, nanotubes arrays etc.), iii. based on chemical composition, nanomaterials can be categorized into four types that are carbon-based materials, materials based on metals, oxides, semiconductors, dendrimers.

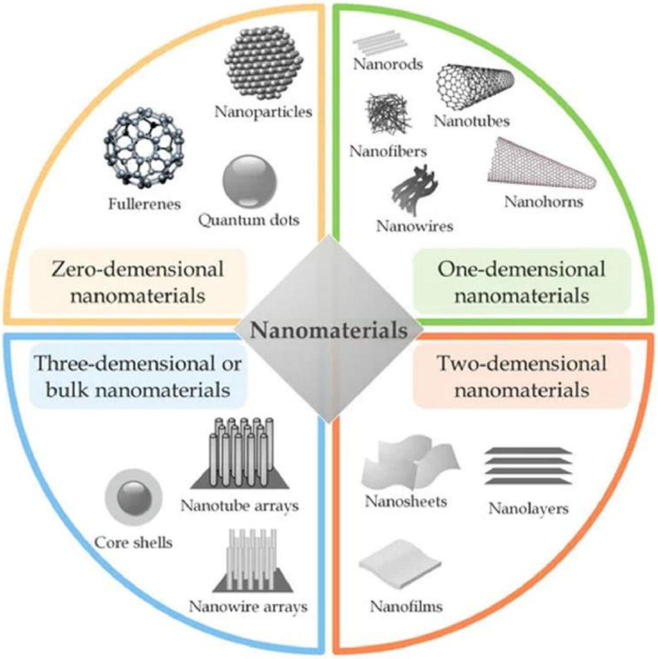

Figure 1.1 Schematic of types of zero, one, two, and three-dimensional nanostructures [12].

Properties of nanomaterials: Nanostructures exhibit distinct characteristics when compared with both individual atoms or molecules at a smaller scale and with macroscopic bulk materials. The physical and chemical properties of nanomaterials (i.e. optical absorption and fluorescence, melting point, magnetism, catalytic activity, thermal and electrical conductivity, etc.) typically differ significantly from those of their bulk counterparts.

By precisely controlling the construction of the materials at the atomic level, it is possible to develop new or improved mechanical, chemical and optical properties. In this context, both surface structure and particle size at the nanoscale are crucial. Developments of new theories, models and characterization methods are important to recognize the relationship between structure and function.

Nanostructured materials are often in a metastable state because their small size, high surface energy, and rapid synthesis processes favor kinetically trapped or energetically higher phases that are distinct from bulk thermodynamic equilibrium states. Their precise atomic arrangement is highly dependent on the kinetic processes involved in their fabrication. Therefore, the properties of nanostructures can be extensively tuned by changing their shape, size and processing conditions [13]. One of the key advantages of nanoscale materials is their large surface to volume ratio, which is significantly greater than that of bulk materials. Thus, nanostructures are believed to have better performances than materials in the micro- or larger scales for sensing and (photo)catalysis applications. A common example of nanostructured materials is zinc oxide, which can appear in various morphologies such as nanowires, nanobelts, nano propellers, nano combs and nanotubes. These diverse morphologies show different physical properties underscoring the versatility and potential of nanostructures in various technological applications.

Synthesis techniques: Nanostructures can be synthesized by using two major approaches "*top-down*" and "*bottom-up*", as shown in figure 1.2 The top-down method involves breaking down bulk materials into smaller particles, by physical processes such as mechanical milling, laser ablation, sputtering, etching and electro-explosion. However, this method is not suitable for producing nanostructures with uniform shapes, and it is very challenging to obtain very small nanoparticles even with high energy consumption [14-16]. A key challenge of this method is to control and maintain a well-defined surface structure, as it does not provide enough control over the precision, smoothness, and uniformity of the nanostructures' surfaces. This can be problematic, because the surface structure is essential for determining the material's behavior in many applications, and a poorly defined surface can lead to suboptimal physical and chemical properties.

In contrast, the bottom-up approaches produce nanomaterials atom by atom or molecule by molecule in large quantities [16, 17], they include physical and chemical routes and are effective in producing nanomaterials with better size distribution and morphology [16, 18]. Among the chemical approaches, various synthesis techniques have been used, such as chemical vapor deposition (CVD), hydrothermal and solvothermal methods, sol-gel, hot-injection, soft and hard templating methods and reverse micelle approaches. Suitably tuning the experimental conditions, these techniques allow the reproducible control over chemical composition and particle size and shape, resulting in nanomaterials with relatively uniform distribution and morphology.

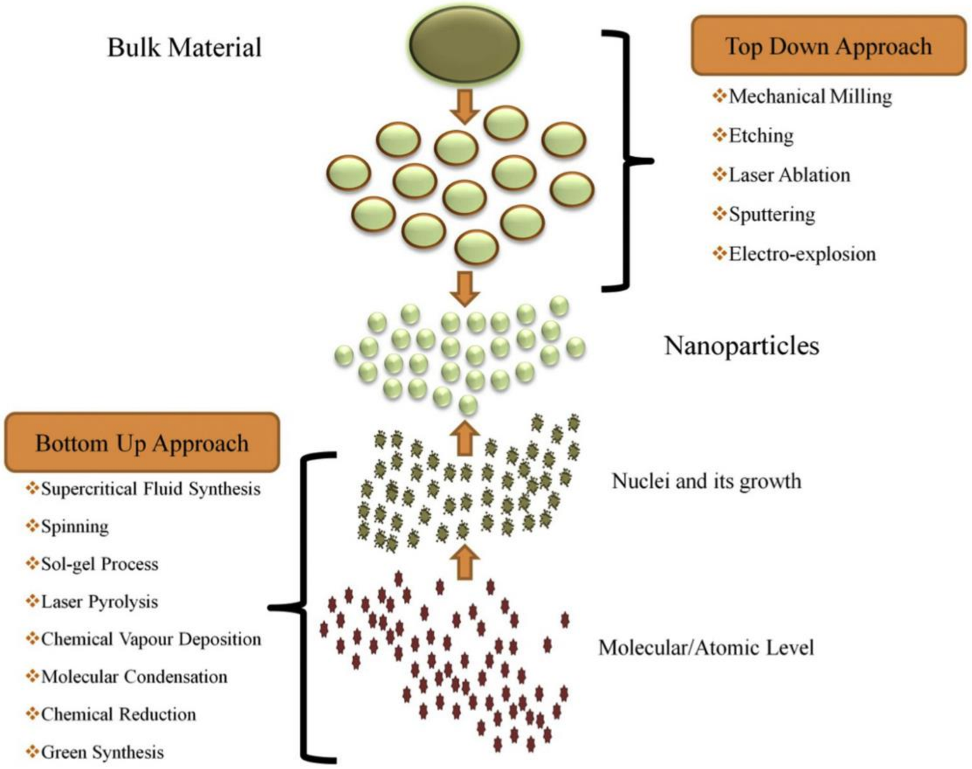

Figure 1.2 Sketch of the synthesis of nanomaterials via *top-down* and *bottom-up* approaches [19].

Applications of nanostructures: Due to their original size and shape dependent properties, nanostructures are increasingly utilized across various fields, significantly advancing nanotechnology applications.

In nanoelectronics, silicon may soon be replaced by carbon nanotubes or monolayer graphene to develop lighter and more efficient microchips and devices. Given the rising energy demands, nanostructured components are being integrated into solar panels and hydrogen fuel cells to increase their efficiency. The use of such renewable resources will be environmentally friendly and can help to limit CO_2 emissions, which is a critical concern today.

In the field of nanomedicine, biocompatible tunneling nanotubes are being explored for targeted drug delivery and health monitoring. The creation of functional organic or synthetic nanostructures for medical implanted devices is certainly challenging, yet breakthroughs are being made in developing artificial joints, larynxes, bone prostheses, pacemakers, and so on.

To address air quality issues, nanoparticles are employed as catalysts to transform hazardous gases released from industries and automotive into harmless gases. Nanoscale structures including rods, rings, beams, plates, and shells have been implemented in fundamental structural parts of various nanoelectromechanical systems (NEMS). Devices based on NEMS including nanomechanical resonators, nanoscale mass sensors, electromechanical nanoactuators, and nano energy harvesters, hold promises for applications in nanoelectronics, nanomachines, and nanomedicine.

It is worth investigating the dynamic characteristics of such nanostructures when subjected to external mechanical loads, pressures, or even stresses [20]. However, conducting precise experiments at this scale is both challenging and costly [21]. Therefore, the continuum-based modeling and simulations related to molecular dynamics have attracted different researchers worldwide to address such complicated issues.

1.2 Colloidal nanoparticles: synthesis, shape control and surface functionalization

Graham et al. [22] introduced the term “colloid” to describe a homogeneous, non-crystalline substance consisting of large molecules. It has been broadly applied to various systems, including polymer suspensions in solution [23], emulsions by amphiphilic molecules in aqueous and organic phases [24], and dispersions of colloidal inorganic particles [25-27]. The term originally referred to the suspension of a solid or liquid phase within a second medium, where the dispersed phase does not spontaneously precipitate.

It is generally accepted that colloidal particles are larger than molecular or ionic clusters (i.e., greater than 1 nm), yet remaining smaller than 1 μm, a size range that imparts distinctive material properties due to their size-dependent characteristics [28]. The unique size- and shape-dependent material properties of inorganic colloids and colloidal metal and metal oxide nanoparticles attracted and allowed scientists and engineers to make substantial progress on a wide range of technological applications such as optoelectronics, catalysis, medicine, and energy and environmental areas [29].

Colloidal nanoparticles are often prone to aggregation, which can result in the loss of their characteristic properties. Therefore, the means to sustain their dispersed state is a critical consideration in synthesis design. One of the major interactions of colloidal metal nanoparticles is the van der Waals force. When two colloidal nanoparticles come within a short interparticle distance, the van der Waals forces, which scale inversely as the sixth power of the interparticle distance, will attract them to each other. In the absence of counteracting repulsive forces, they will collapse and aggregate.

To ensure the stability of colloidal nanoparticles in solutions, it is necessary to introduce a repulsive force that resists the van der Waals attractions [29]. The stability of colloidal systems consisting of nanomaterials can be explained by the Derjaguin-Landau-Verwey-Overbeek (DLVO) theory [30], which often provides reliable estimate for inter surface forces for surface separations as small as 5 nm. Based on their theory, electrostatic and steric stabilization are known as two main approaches for stabilizing colloidal nanoparticles.

The precise control of nanoparticle shape is a critical focus in nanotechnology, as it allows for the fine tuning of properties important for a wide range of applications. Numerous studies have explored various methodologies to manipulate nanoparticle shapes effectively. For instance, Sun et al. [31] demonstrated the shape transitions of nanoparticles based on charge-patterned surfaces, while Zamkov et al. [32] highlighted a thermodynamically driven growth strategy for shape-selective syntheses of semiconductor nanocrystals. Beaton et al. [33] explored the application of Ag NPs in surface-enhanced Raman scattering (SERS) for chemical sensing, emphasizing their advantageous plasmonic properties but limited stability due to oxidation. The study demonstrated that supporting Ag NPs on alumina significantly improves their *resistance* to oxidation while allowing for photochemical shape control. Notably, these Ag NP-alumina substrates proved effective in detecting the pesticide thiram, with a detection limit of 96 ppb (m/v).

Additionally, Varanda et al. [34] emphasized the significance of synthesis methodologies for achieving monodisperse nanoparticulate systems with precise shape control. Shuang et al. [35] introduced an innovative approach for preparing small-sized fluorescent carbon nanoparticles with tunable shapes, attributing the shape control mechanism to interionic interactions-induced self-assembly. Collectively, these studies contribute to advancing the understanding and techniques for precise shape control of colloidal nanoparticles, essential for optimizing their functionalities in various fields.

The synthesis of engineered colloidal nanoparticles (NPs) with precisely tailored surface characteristics leads to well defined physicochemical properties, enabling their use for multifunctional applications. Functionalization techniques, both in-synthesis and post-synthesis, allow for the tuning of nanoparticle properties such as size, shape, and functionality, impacting bioavailability, specificity, and catalytic performance [36] . Surface functionalization influences the catalytic properties of metal nanoparticles by controlling surface-coordinated species, which in turn modulates catalytic intermediates, catalyst-electrolyte interfaces, and active site accessibility, crucial for processes like artificial photosynthesis [37] .

Surface engineering of colloidal NPs can improve their stability in diverse solvents by mitigating attractive interparticle forces, thus providing a prerequisite for further particle manipulation, material fabrication and biological applications. Over the past decades, significant advancements have been made in the surface engineering of colloidal NPs. However, achieving precise control over surface properties remains a critical challenge.

The emerging DNA/protein nanotechnology offers additional possibility of surface modification of NPs and programmable particle self-assembly [38]. Surface-functionalized nanoparticles find extensive applications in healthcare, imaging, drug delivery, antimicrobial activity, biosensing, and environmental monitoring, showcasing their versatility and potential in various fields. Moreover, the controlled surface functionalization of nanoparticles can also enhance their stability, biocompatibility, and targeting capabilities, making them promising candidates for advanced drug delivery systems and targeted therapies in precision medicine.

1.3 Synthesis techniques, properties and applications of Ag nanowires (NW)

For several decades, silver has been widely recognized for its notable antibacterial activity and low toxicity towards human cells [39]. These attributes have facilitated its successful implementation in prophylactic burn treatment and water purification system [40, 41]. Considering the growing prevalence of antibiotic-resistant bacteria [42], and rapid advancement in nanoscale technology, scientific focus has shifted toward silver nano species, due to their unique electrical, optical, chemical and physical properties and their potential in a variety of fields spanning from consumer products like toothpastes, to advance materials such as electrodes [43], including potential future biomedical applications [44, 45].

Among the most synthesized silver nano species there are silver nanowires (Ag NWs), silver nanorods, silver nanocubes and silver nanospheres [46-48], with more recent development including silver nanocoils [49]. Due to their increased surface area to volume ratio, silver nanospecies offer enhanced characteristics compared to bulk silver [50, 51] and may therefore provide a valuable enhancement to our current antibacterial arsenal. To date, these silver nanospecies have been shown to be effective against a variety of bacteria's such as *Escherichia coli* [52], *Staphylococcus aureus*, *Klebsiellia pneumoniae [53]* and *methicillin-resistant Staphylococcus aureus [54]*.

The template method is a versatile approach for synthesizing nanomaterials with desired aspect ratio and achieving highly directional arrangement of NWs. The template is convenient to synthesize and determines the quality of the final synthesized NWs [55]. The template methods are broadly categorized into hard template and soft template methods.

The hard-template method employes nanoporous membranes, such as carbon nanotubes, nanoporous silica and alumina membranes, zeolites and track-etched polycarbonate, to guide the growth of Ag NWs [54]. The key advantage of this method is its ability to synthesize Ag NWs in a controlled manner, with uniform dimensions. Additionally, the synthesized NWs are already immobilized on a substrate, which is particularly advantage to produce nanodevices.

Anodic aluminum oxide (AAO) is the most frequently used hard template for the synthesis of Ag NWs arrays due to its uniform nanometer-size holes, which are tunable in diameters and its pores density can be controlled by adjusting the oxidation conditions [56-58]. Zhang et al. [59]

successfully synthesized single-crystalline Ag NW arrays using AAO templates at 970°C. They introduced CuO as a supplement to enhance the infiltration height by improving the wetting behavior between the molten Ag and the AAO template. AAO template was removed using a sodium hydroxide (NaOH) solution in a high-pressure autoclave.

Hard templates offer significant advantages in the preparation of ultrathin NWs, providing excellent control over size, shape, and overall morphology of NWs because of their predesigned well-distributed, and uniform aperture and channel length. However, the removal of these templates involves complex procedures, and a purification step can lead to a significant loss of the synthesized NWs. This reduction in yield and *potential* damage to the NWs limits the suitability of the hard template method for the large-scale industrial production [60].

The soft template methods utilize chemicals such as surfactants, polymers, and micelles that are dissolvable or dispersible in solvents and can be absorbed onto the growing crystal surfaces. These templates control kinetically the growth rates of NWs through their adsorption and desorption from the crystal surface. One of the significant advantages of soft templets is the easy purification of NWs from the solvent phase, leading to enhance efficiency and scalability in NWs production. Murphy et al. [61] successfully synthesized silver nanorods and NWs using rodlike micellar cetyltrimethylammonium bromide (CTAB) as templates [61, 62]. The aspect ratio of the resulting NWs could be adjusted by the size and shape of the CTAB templates, as well as the molar ratio of surfactants, precursors and salts. Hong et al. [63] reported the synthesis of atomic sized and highly stable single-crystalline Ag NWs using a soft template in an ambient aqueous phase. These ultrathin Ag NWs, with a diameter of 0.4 nm, extended to micrometer lengths within the pores of self-assembled calix [4] hydroquinone nanotubes (CHQs) via electrochemical or photochemical redox reactions. The CHQ moieties have a rich π-electron density, which enables them to trap metallic Ag ions in their pores with high affinity through cation-π interactions.

The traditional synthesis of Ag NWs involves using Pt NPs as seeds for heterogeneous nucleation. Pt NPs are first prepared and act as nucleation sites for silver atoms. A solution containing silver precursors, such as silver nitrate, and reducing agents like ascorbic acid is then introduced to the Pt seeds. Silver ions reduce onto the Pt surfaces, promoting the growth of elongated nanowires in preferred directions.

Polyol synthesis of Ag NWs: [64, 65] The polyol method, developed over the past three decades, is now the widely recognized approach to synthesis Ag NWs due to its plenty of advantages, including high quality, low cost, ease of control and importantly its suitability for large scale industrial production. Xia et al. were the first to validate the synthesis of Ag NWs using poly (vinyl pyrrolidone) (PVP) as the soft template, overcoming the limitations of previous methods that relied on the use of platinum (Pt) nanoparticle seeds to induce heterogeneous nucleation. This approach presents significant advantages over the traditional Pt nanoparticle seed method, primarily in terms of cost, simplicity, and control over the synthesis process. The Pt-based process was not only complex, but also cost-prohibitive due to the high price of Pt nanoparticles.

The introduction of PVP allowed for a simplified self-seeding method; PVP was initially dissolved in ethylene glycol, which acts both as a reducing agent and green solvent, and silver nitrate ($AgNO_3$) precursor, that was carefully injected into the reaction mixture at a control rate using a syringe actuated by a peristaltic pump. The rate of addition of the Ag+ source was crucial for controlling the size of the produced nano species [64].

Researchers conducted extensive and in-depth studies on the preparation of Ag NWs by the polyol method to synthesis Ag NWs with high aspect ratio, high purity and small diameter, although, it is still challenged to control the reaction parameters well to achieve a shape-controlled synthesis of uniform Ag NWs with high aspect ratios.

Ye et al. [66] successfully synthesized Ag NWs with a diameter of 20 nm and an aspect ratio larger than 1500 using a polyol method under nitrogen-protected atmosphere. The reaction system was heated up to 180°C for effectively initiating the reaction and promoting nucleation and then the temperature was lowered down to 160 °C to enhance uniform growth. This way of lowering the temperature of the subsequent reaction stages promoted the uniform nucleation of Ag nanoparticles, resulting in Ag NWs of high purity, approximately 94.5%.

Several studies have also been carried out to clarify the molecular mechanisms involved in the formation of Ag NWs; the complexities of this process were thoroughly reviewed by Xia et al. [67]. The soft-template method, central to this process, involves reducing the silver salt to metallic silver within the polyol reducing solvent. At elevated temperatures, the polyol oxidizes to an aldehyde, which acts as the actual reducing agent [68] of the silver precursor. The formed Ag clusters assemble to form multiply twinned particles with a decahedron structure [69] (Figure 1.3 a,b). Additionally, Ag atoms adsorb onto these particles, and growth occurs both axially and radially until a critical phase is reached, at which point radial growth ceases, and only axial growth continues along the [111] facets. In this mechanism, PVP acts as a capping agent, thanks to the ability of its carbonyl groups to bind Ag atoms on the {100} facets (Figure 1.3 c), which helps to drive the growth exclusively in the axial direction [67, 70-72] (Figure 1.3 d).

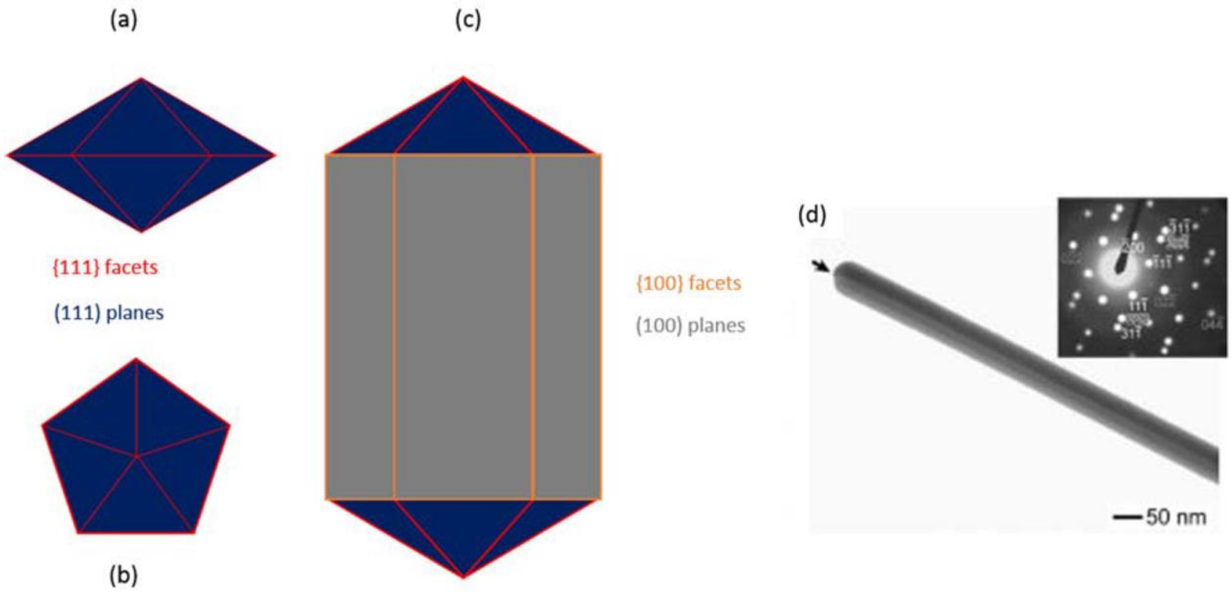

Figure 1.3 Crystal structure of AgNWs: (a) side and (b) top view of a multiply twinned particle of decahedral structure with {111} facets and (111) planes highlighted; (c) side view of an axially elongated crystal grown by passivation of the {100} facets; (d) typical TEM image of a single AgNW [73].

Despite successful synthesis at a small scale, carefully and accurately controlling the injection rate of $AgNO_3$ into the reaction mixture proved challenging to scale up such an approach for industrial applications.

To address this issue, Korte et al. [74] suggested that the addition of trace amounts of salts could slow down the reaction rate and improve control over the growth of the Ag NWs. Specifically, CuCl2 was added to the reaction mixture after the addition of the Ag precursor. It was found an improvement in the deposition of Ag by removing oxygen atoms that blocked growth sites at the Ag NWs surface. On the other hand, Cl- ions acted as a rate-determining step of the overall reaction, by forming temporary AgCl precipitates, whose slow dissolution provided further control over the reaction rate [75].

1.4 Synthesis and properties of graphene

The molecular structure of carbon can manifest in different allotropic forms depending on its morphology: (a) when folded into a 0D structure, it forms spherical compounds known as fullerenes or carbon dots; (b) when rolled into a 1D structure it forms carbon nanotubes; (c) when arranged as a single 2D atomic sheet, it is graphene and (d) when it is stacked into a 3D bulk structure it is graphite [76].

In 2004, Geim and Novoselov used a scotch tape to exfoliate a block of graphite in graphene, a breakthrough in the field of material science and ultimately earned them the Nobel Prize in physics in 2010 [77].

Since this discovery, graphene has become the quintessential nanostructure among carbon-based materials. The European Union's Horizon 2020 program funded, with a budget of €1 billion, research activities aiming to bring studies on graphene and other layered materials from fundamental research to industrial and societal applications [78, 79]. Graphene is known as the thinnest material, possessing a high charge mobility at low temperature ($\mu \sim 2\times10^5$ $cm^2V^{-1}s^{-1}$) with charge carriers that could be more than 10^{12} cm^{-2}. It is notable that the mobility of graphene on a silicon substrate is ~800 $cm^2V^{-1}s^{-1}$ at room temperature.

Graphene can be considered as a solid or a macromolecule with molecular weights exceeding 10^7 g/mol. It has high thermal conductivity ($K \sim 5\times10^3$ $Wm^{-1}K^{-1}$) and low anisotropic thermal expansion coefficient, high optical transparency (~97.7%) in the visible spectra range, minimal reflectivity (<0.1%), large surface area (~2630 m^2/g), and remarkable mechanical properties ($E \sim 1$ TPa), including flexibility up to 30%. Graphene also demonstrates high electrical conductivity

(~20,000 S/cm) and remains stable in air up to 400°C, while acting as an effective gas barrier [79-81].

These extraordinary properties of graphene make it a highly attractive material for a vast number of applications, including solar cells, hydrogen storage, displays, spintronics, drug delivery, field effect transistors, sensors, electrodes, batteries and capacitors, composites, desalination and water treatment [82, 83], tissue engineering, bioimaging, biosensing, delivery of anti-cancer agents, gene therapy, and antibacterial applications [84].

Single layer graphene (SLG) specifically is ideally defined as an infinite hexagonal network of sp^2 carbon atoms with a unit cell that covers an area of approximately 0.052 nm^2 and consists of two non-equivalent atoms that form bipartite lattice with a distance of 1.42Å, which is the mean value of a single (C-C) and a double (C=C) covalent bond [76]. In the sp^2 hybridized C atoms of SLG, the s, px and py orbits are combined to form three orbits in the plane. The covalent bond resulting from the interaction of these orbitals between neighboring carbon atoms convey supreme mechanical properties to SLG [85]. In addition, the delocalization of the px orbitals above and below the basal plane, convey to SLG outstanding electrical and thermal conductivity, along with interesting optical properties.

Graphene synthesis is a demanding process, especially when a large area is desirable, and involves either bottom-up (from atoms to nano) or top-down (from bulk to nano) methodologies. The bottom-up methodologies include growth on SiC and on metals by precipitation, molecular beam epitaxy and chemical vapor deposition. The top-down methodologies include dry and/or liquid-phase exfoliation, unzipping of nanotubes and chemical exfoliation.

Chemical vapor deposition (CVD) may be a more practical synthetic method for graphene, as reported by recent studies. The first synthesis of graphene using CVD was reported by Somani in 2006, who used camphor and nickel substrate [86]. Since then, numerous technical advancements have been made with current research focusing on the reproducible production of n-layered graphene (n = integer) without impurities and defects. Generally, the synthesis of graphene by CVD involves five broad steps: (a) pre-heating of a substrate and precursors, (b) annealing of the substrate without sublimation, (c) insertion of gases/precursors and formation of graphene layer(s), (d) gradual cooling and (e) insert gases to remove by-products [87].

In 1958, Hummer and coworkers demonstrated the use of an oxidizing reaction mixture including $KMnO_4$, $NaNO_3$ in H_2SO_4 with the aim of producing a graphene derivates from the oxidation of graphite, and since then, this reaction has been called the modified Hummer's method. The product achieved from this reaction was called graphene oxide (GO), and it is based on domains of sp^2 carbon atoms arranged in a honeycomb structure, as well as domains with structural defects bearing oxygen based functional groups (Figure 1.4A), which make it dispersible in hydrophilic solvents, and easy to be functionalized by chemical approaches for its use in various applications. GO exhibits high thermal conductivity, flexibility, chemical stability, adjustable electrical conductivity, high surface area, excellent biocompatibility [88] and moderate mechanical strength [89, 90]. While its conductivity and thermal properties are lower than pristine graphene, GO's dispersibility, tunable optical properties, and ability to be chemically modified make it suitable for various applications, from energy storage to water purification and biomedicine.

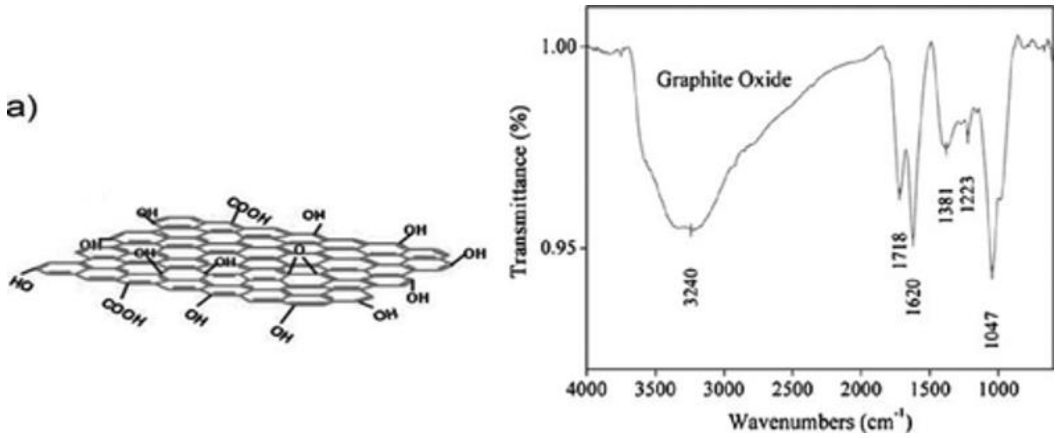

Figure 1.4 (a) Structure of GO and (b) its FTIR spectrum [91].

GO can be reduced to graphene-like sheets by removing the oxygen-containing groups with the recovery of a conjugated structure, achieving another graphene derivative called Reduced Graphene oxide (RGO). The latter is a versatile and scalable material possessing the structural properties, electrical, thermic and mechanical closest to those of pristine graphene. It has found widespread use in various applications due to the low cost of its production and high reactivity of its basal plane.

RGO can be synthesized from GO by chemical, thermal and electrochemical reduction. Chemical reduction involves the use of reducing agents such as hydrazine, sodium borohydride, or ascorbic acid [92]. RGO retains a large surface area and high conductivity, making it suitable for applications such as catalysis, sensors, energy storage, electrochemical devices [93], water purification and flexible electronics [94]. Its mechanical properties can be significantly improved when incorporated into composites [89].

Characterization of graphene is a crucial aspect in graphene research and involves the use of spectroscopic and microscopic techniques to assess its properties. Characterization focuses on determining the size of the sheets, number of graphene layers and quality of the sample, particularly in terms of presence or absence of structural defects.

Optical contrast analysis of graphene layers on different substrates is the most simple and effective technique for identifying the number of layers. This technique is based on the contrast generated by the interference of the reflected light beams at the air-to-graphene, graphene-to-dielectric, and (in the case of thin dielectric films) dielectric-to-substrate interfaces [95]. AFM, Raman and XRS are other valuable tools for graphene characterization. AFM directly measures surface height to determine the number of layers. Raman Spectroscopy investigates structural quality of graphene and allows them to differentiate between single-layer, bilayer, and multilayer graphene. X-ray Reflectivity uses interference patterns from reflected X-rays to assess the number of layers.

1.5 Surface functionalization approaches of graphene

Surface functionalization of pristine graphene sheets with chemical groups or molecules has been extensively developed for a variety of applications. A primary objective of this functionalization is to improve graphene's dispersibility in common organic solvents for its processing from dispersions. The functionalization with organic functional molecules, such as chromophores, can impart new properties to graphene, which can complement its inherent characteristics, such as absorption in visible spectral range. Another significant outcome of its functionalization is the possibility to modify its electronic level structure by developing a band gap by chemical doping. This method is particularly valuable for enabling the use of graphene in nanoelectronics devices [96].

The functionalization strategies are generally categorized into covalent and noncovalent methods, depending on the nature of the bonding involved.

The organic covalent functionalization of graphene typically follows two primary pathways: (a) formation of covalent bonds between free radicals or dienophiles and the C=C bonds in pristine graphene, and (b) formation of covalent bonds between organic functional groups and the pristine oxygen-containing groups in GO.

One prominent example involves the addition of free radicals to the sp^2 carbon atoms of graphene. When diazonium salts are heated, highly reactive free radicals are generated, which can attack the sp^2 carbon atoms, resulting in the formation of covalent bonds. This approach was employed by Tour and colleagues to functionalize graphene with nitrophenyls [97, 98]. Graphene sheets in this work were obtained by chemically unzipping carbon nanotubes. During the functionalization process, measurements of the graphene sheet's conductivity, using a simple device (Figure 1.5), revealed a significant decrease in conductivity. This reduction is attributed to the disruption of the graphene's aromatic system, as the sp^2 carbon atoms are transformed to sp^3 hybridization due to covalent bonding with the free radicals.

The addition of dienophiles to carbon–carbon bonds is another key route for the functionalization of graphene, apart from free radicals. Dienophiles, such as azomethine ylide, which undergoes 1,3-dipolar cycloaddition, are commonly employed in the functionalization of various carbon nanostructures, including fullerenes, nanotubes and nanohorns. This type of reaction affords a variety of organic derivatives, which hold potential for applications in areas such as polymer composites, biotechnology, nanoelectronics, drug delivery, and solar cells [99, 100]. In a notable example, Georgakilas et al. [101] demonstrated that graphene sheets, produced directly from graphite dispersed in organic solvents [102], could be functionalized with pyrrolidine rings through the 1,3-dipolar cycloaddition of azomethine ylide.

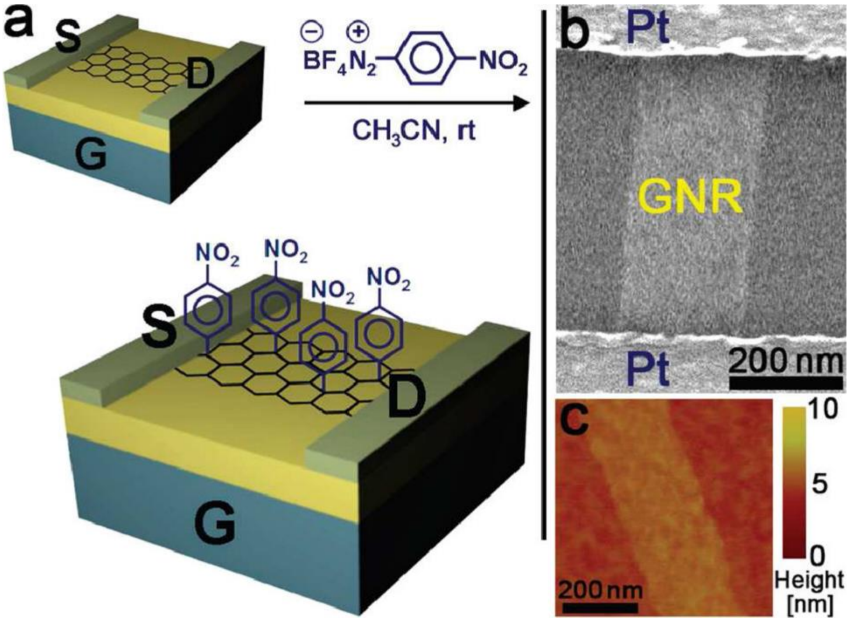

Figure 1.5 Chemical doping of graphene with 4-nitrophenyl groups: (a) schematic representation; (b) SEM image of a graphene nanoplatelet between Pt electrodes; (c) AFM image of a fragment of a monolayer graphene [97].

Polymers are among the compounds most frequently used for the covalent functionalization of graphene, due to their structural properties (mechanical, rheological, electrical conductivity, biocompatibility etc.), low cost, sustainability and easy processability from solutions. Polymethylmethacrylate (PMMA) [103], polythiophene [104], polyethylene glycol (PEG) [105], chitosan [106] have been covalently grafted onto SLG, GO and RGO for various purposes. Salavagione et al. [107] reviewed polymer-based covalent modifications of graphene derivatives into two main methods: chemical conjugation of pre-formed polymers to the graphene surface and polymer growth initiated directly from graphene.

The abundant hydroxyl, carboxyl, and epoxy groups in GO make it an optimal platform for the preparation of new materials by covalent functionalization approaches. Raman spectra of functionalized GO typically show no significant deviations from those of the unmodified GO, indicating minimal addition of further structural defects.

Non-covalent functionalization of graphene, GO and RGO have also been widely explored in many studies. Non-covalent intermolecular interactions involving π-systems play a crucial role in the stabilization of various biological and chemical systems, including proteins, enzyme–drug complexes, DNA–protein complexes, organic supramolecules, and functional nanomaterials [63, 108, 109]. These interactions are particularly significant in the design and fabrication of nanomaterials and nanodevices, where even small changes in the electronic properties of π-systems can result in substantial effects on the structure and behavior of nanosystems [63, 108].

Over the past two decades, extensive studies have been conducted to understand the nature of π-complexes that graphene can form with its aromatic basal plane for applications in devices and sensors [110]. These include various types of π-interactions such as nonpolar gas–π, H–π, π–π, cation–π, and anion–π interactions [111, 112]. Extensive investigation has focused on the energetic and geometric aspects of π-interactions, with theoretical insights primarily derived from high-level ab initio calculations. These studies have been instrumental in elucidating the nature of π-interactions; tthe strength of these interactions arises from a balance between attractive forces (such as electrostatic, dispersive, and inductive interactions) and repulsive forces (exchange repulsion). Each of these forces differs in its physical origin, magnitude, and directionality, contributing to the overall complexity and importance of the π-interactions in nanomaterial applications.

The first stable graphene dispersion using a noncovalent functionalization route was achieved by reducing an aqueous GO dispersion with hydrazine in presence of poly (sodium 4-styrenesulfonate) (PSS) [113]. In this process, the achieved rGO sheets were stabilized through aromatic $\pi - \pi$ interactions with the hydrophobic backbone of PSS, while the hydrophilic sulfonate side groups helped to maintain the dispersion of the graphene–PSS complex in water.

Noncovalent functionalization of graphene sheets through aromatic $\pi - \pi$ stacking interaction with the water-soluble 1-pyrenebyturate (PB), was explored to achieve large-area flexible PB coated graphene films by vacuum filtration [114]. Such noncovalent functionalization has shown significant enhancement in solubility and conductivity of the graphene sheets and offers a versatile strategy for modifying graphene while preserving its outstanding structural properties [115-118].

Also, biomolecules such as single-strand DNA (ssDNA) have been involved in the functionalization of graphene by van der Waals force, demonstrating their ability to stabilize aqueous suspensions of graphene sheets [119].

1.6 Hybrid nanocomposites comprising graphene and colloidal nanoparticles: Synthesis methods and applications

Hybrid nanocomposites that integrate graphene with colloidal NPs have garnered significant attention due to their enhanced properties and diverse applications. These materials leverage the unique characteristics of graphene alongside the functionalities of various NPs, leading to innovative solutions across multiple fields. The approaches for preparing these nanocomposites can generally be categorized into two main types, *ex situ* and *in situ* (Figure 1.6).

In the *ex-situ* approach, NPs are pre-synthesized and then immobilized onto the aromatic surface of graphene. This process typically involves a bifunctional linker that binds the graphene basal plane by π-π stacking, hydrophobic interactions, or electrostatic forces, and that anchors, by coordination or covalent, or electrostatic interactions, the NPs by its end chemical group [120] (Figure 1.6).

The *in situ* approach involves synthesizing nanocomposites or NPs directly onto graphene. This method utilizes the intrinsic residual oxygenated functional groups on GO or the additional functional groups grafted onto the GO and rGO basal plane as coordinating sites at which the NPs nucleate and grow by chemical reduction, in presence of suitable coordination agents, starting from specific precursors [121].

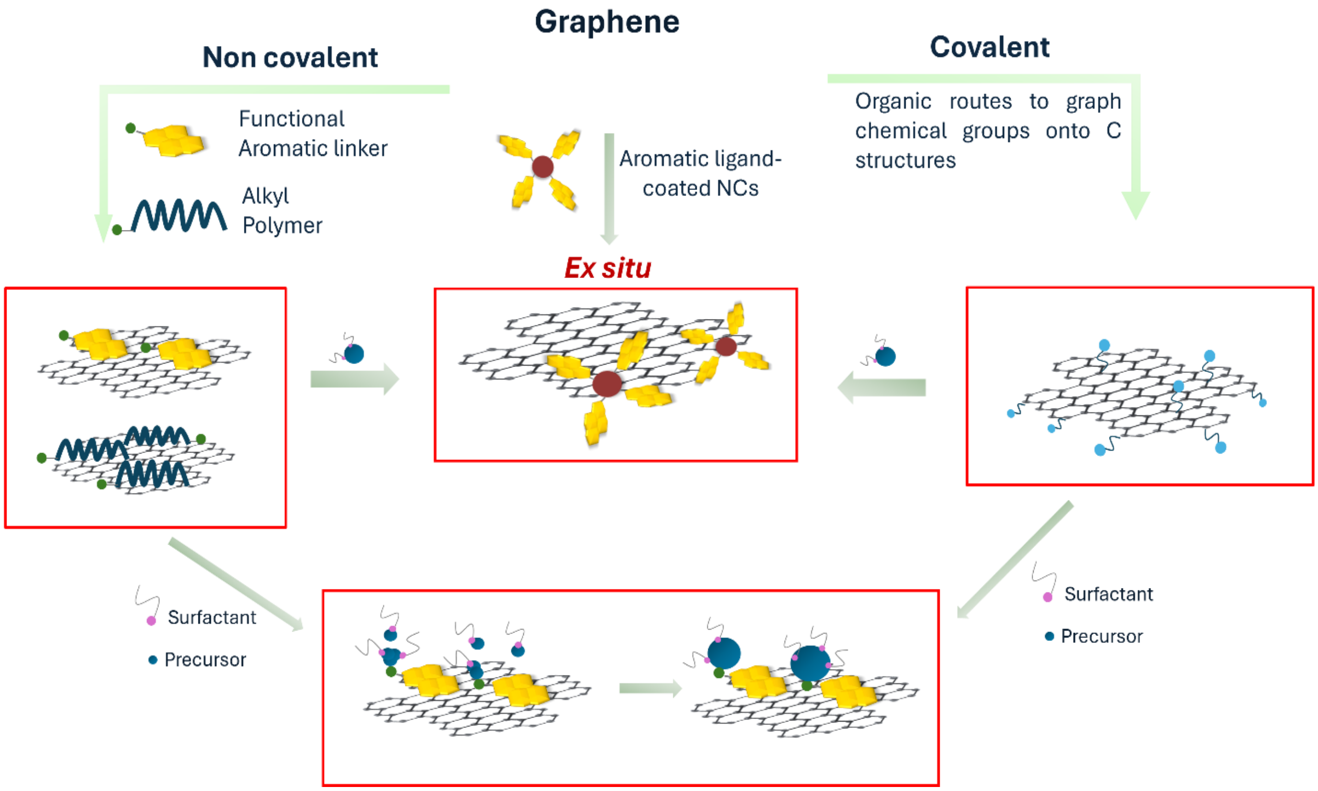

Figure 1.6 Scheme of preparation of hybrids based on graphene derivatives and colloidal NPs with covalent and non-covalent functionalization approaches, *in situ* and *ex situ*.

Following *in situ* synthesis routes, graphene derivatives have been decorated with colloidal nanoparticles (NPs) such as silver (Ag) [122, 123], gold (Au) [124-126], copper (Cu) [127], Palladium (Pd) [128], platinum (Pt) [129], and nickel (Ni) [130], by chemical [123], microwave assisted [127] and photochemical reduction [126]. Depending on the type of the anchored NPs, the graphene–metal NP hybrid nanocomposites have been applied in a wide range of applications, such as surface-enhanced Raman scattering (SERS) [124], catalysis [131] and electrochemical sensing [132].

Pd NPs supported on GO were prepared by bubbling hydrogen through a suspension of a Pd2+ precursor and GO in ethanol, and the synthesized composites were used as catalysts in the Suzuki–Miyaura coupling reaction [131]. The Pd/GO and Pd/rGO composites exhibited higher catalytic activities compared to conventional Pd/carbon catalysts, with turnover frequencies surpassing 39,000 h^{-1} indicate high efficiency in catalyzing reactions, while the very low palladium leaching (< 1 ppm) ensures minimal contamination and prolonged catalyst stability. This makes graphene-based materials a promising alternative to conventional support for palladium catalysts, enhancing both the efficiency and sustainability of chemical reactions.

A notable example of a hybrid nanocomposite, which holds both fundamental and practical interest, involves the combination of GO/rGO and colloidal Au NPs, that are synthesized onto the GO basal plane through an *in situ* colloidal approach. This approach allows for the controlled synthesis of Au NPs with varying sizes, depending on the strength of the reducing agent used [133].

The first graphene–Au NP composite was synthesized by the reduction of the $HAuCl_4$ precursor with $NaBH_4$ in a dispersion of rGO coated by octadecylamine (ODA). The functionalization of rGO with ODA increases the dispersibility of the composites in low-polar solvents like tetrahydrofuran (THF) and ODA reduces the Au precursor.

Another example consists of the synthesis of small Au NPs (2–3 nm in size) directly on the surface of GO sheets in an aqueous solution, starting from $HAuCl_4$, which is reduced to elemental gold (Au^0) by the strong reducing agent sodium borohydride ($NaBH_4$) [121]. Larger Au NPs, ranging from 10 to 20 nm, can be achieved onto GO using the same $HAuCl_4$ precursor, reduced by milder reducing agents as citrate or ascorbic acid. Using an *in situ* approach, F. Vischio et al. [134]successfully synthesized a hybrid nanocomposite consisting of carboxylated nano graphene oxide (c-NGO) densely decorated with monodisperse, citrate-coated Au NPs (c-NGO/Au NPs), with an excellent control over morphology. The nanocomposite demonstrated interesting photothermal properties resulting a in promising nanoplatform for photothermal ablation of cancer cells (Figure 1.7).

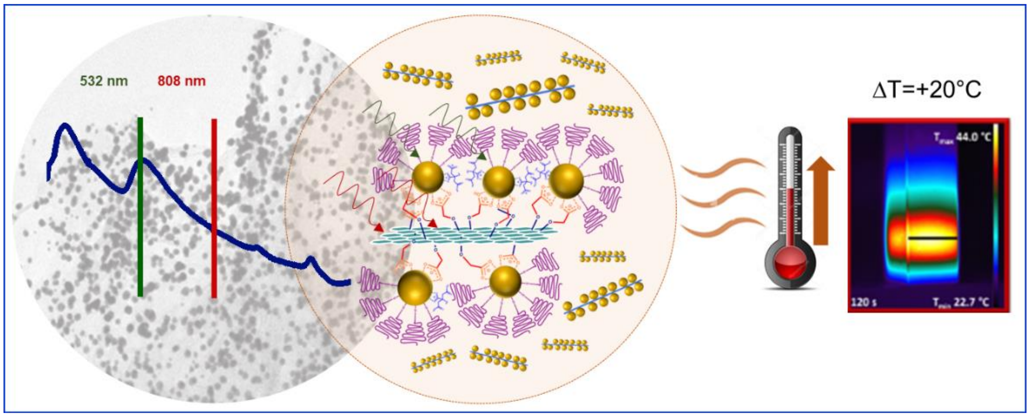

Figure 1.7 Hybrid nanocomposite based on NGO and Au NPs for photothermal applications [134].

Another hybrid nanocomposite was synthesized by an *in situ* approach by C. Ingrosso et al. [121] by a modified Brust's method [133]. In this process, the $HAuCl_4$ precursor was first reduced from Au^{3+} to Au^{+} in the presence of the PCA-RGO complex, using the aromatic thiol 3,4-dimethylbenzenethiol (DMBT), and then the reduction from Au^{+} to Au^{0} is completed with $NaBH_4$. In this process, the carboxyl groups of PCA act as heteronucleation centers for the growth of the Au NPs [135]. The use of the aromatic DMBT allows to slow down and control the reduction process, while also facilitating the binding of the Au NPs onto the RGO basal plane through π-π interactions. This binding ensures electronic coupling between RGO and the Au NPs. Besides, the

DMBT capping ligand facilitates electronic coupling through π-π interactions between the NPs and RGO, as well as between the Au NPs themselves.

Due to the strong coordinating ability of the thiol and the reducing power of $NaBH_4$, the resulting Au NPs are small, around 2–3 nm, and exhibit a significant plasmon absorption peak at 564 nm.

The resulting hybrid nanocomposite was utilized to modify screen-printed carbon electrodes (SPCEs). These hybrid-modified SPCEs were further functionalized with a thiolated DNA capture probe and tested in a streptavidin-alkaline phosphatase catalyzed assay for detecting miRNA-221 (Figure 1.8) in spiked human blood serum samples. The proposed genosensor exhibited high sensitivity, with a limit of detection (LOD) of 0.7 pM.

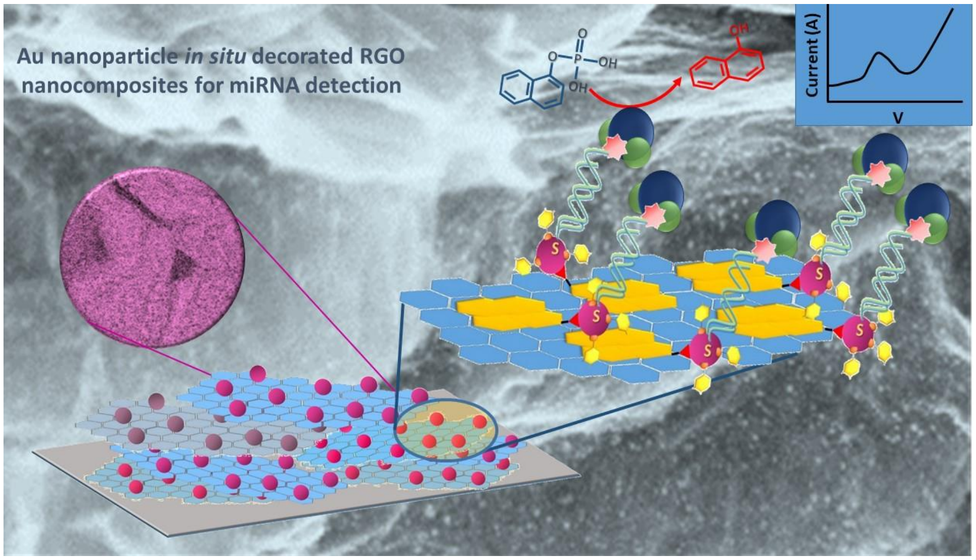

Figure 1.8 PCA-RGO/Au NPs hybrid nanocomposite for miRNA-221 detection [135].

Another nanocomposite was synthesized functionalizing GO with 3,4,9,10-perylene tetracarboxylic acid (PTCA), which was subsequently reduced to rGO with hydrazine, and Au NPs were synthesized onto rGO via reduction of $HAuCl_4$ with amino-terminated ionic liquid (IL-NH 2). The formed composite was water-soluble and showed a high surface coverage of uniformly distributed Au NPs, thanks to the presence of the carboxylic acid groups of PTCA that act as a coordinating site for the formed Au NPs.

A similar approach was used to prepare a nanocomposite based on RGO flakes functionalized with 1-aminopyrene (PA) and subsequently decorated with Au NPs [136]. In this material, the Au NPs nucleate and grow onto the amino groups of the PA-functionalized RGO through π-π interactions. The $HAuCl_4$ precursor is reduced to Au^0 by oleylamine (OLEAM), a long-chain alkyl amine that acts as both the solvent and coordinating agent, thereby stabilizing the hybrid nanocomposite in organic solvents. This hybrid material was deposited by casting onto screen-printed carbon electrodes (SPCEs) (Figure 1.9), that were treated with a mixture of methanol and acetic acid (CH_3OH/AcOH) to remove the oleylamine dielectric layer, making the surface of the nanocomposite modified SPCEs more electrochemically active. These modified SPCEs were employed for the label-free detection of dopamine (DA) (Figure 1.9), a neurotransmitter, whose abnormal concentrations are indicative of neurodegenerative disorders such as Parkinson's disease and Huntington's disease [137].

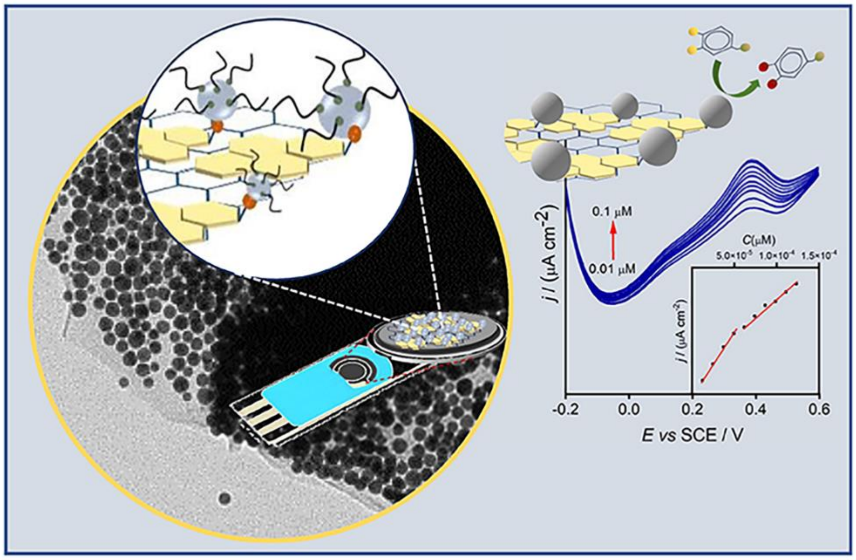

Figure 1.9 AP-RGO/Au NPs for the detection of dopamine [136].

There is also significant interest in the synthesis of graphene-semiconductor nanomaterial composites due to their potential in electronics, optics, and energy-based applications such as solar cells, supercapacitor and Li-ion batteries. The synthetic methods for these types of composites include *in situ* synthesis [138], solution mixing [139], vapor deposition [140], electrochemical deposition [141] and microwave-assisted growth [142]. Graphene–CdS composites were synthesized by mixing GO and $Cd(CH_3COO)_2$ in dimethyl sulfoxide (DMSO), followed by heating in an autoclave at 180° C for 12 h [143]. During this hydrothermal process, CdS NPs were formed simultaneously with the reduction of GO to rGO in DMSO, which serves both as a solvent and sulfur source. Time-resolved fluorescence spectroscopy data showed a picosecond ultrafast electron transfer process from CdS NPs to the graphene sheet, highlighting the potential optoelectronic application of this graphene–CdS hybrid material.

References

1. Allred, D.B., et al., *Electrochemical nanofabrication using crystalline protein masks.* Nano letters, **2005**. 5(4): p. 609-613.
2. Agarwal, N., et al., *Derivatization and interlaminar debonding of graphite–iron nanoparticle hybrid interfaces using Fenton chemistry.* Physical Chemistry Chemical Physics, **2017**. 19(25): p. 16329-16336.
3. Ariga, K., Y. Yamauchi, and M. Aono, *Commentary: nanoarchitectonics—think about NANO again.* APL Materials, **2015**. 3(6).
4. Dai, H., et al., *An electrochemical sensor based on phytic acid functionalized polypyrrole/graphene oxide nanocomposites for simultaneous determination of Cd (II) and Pb (II).* Chemical Engineering Journal, **2016**. 299: p. 150-155.
5. Chan, W.C. and S. Nie, *Quantum dot bioconjugates for ultrasensitive nonisotopic detection.* Science, **1998**. 281(5385): p. 2016-2018.
6. Arivalagan, K., et al., *Nanomaterials and its potential applications.* **2011**.
7. Altmann, J., *Military uses of nanotechnology: perspectives and concerns.* Security Dialogue, **2004**. 35(1): p. 61-79.
8. Feynman, R., *There's plenty of room at the bottom*, in *Feynman and computation*. **2018**, CRC Press. p. 63-76.
9. Chakraverty, S., *Nano Scaled Structural Problems.*
10. Shahid, I. and M. Alam, *A critical review on types and applications of Nano structured materials.*
11. Jeevanandam, J., et al., *Review on nanoparticles and nanostructured materials: history, sources, toxicity and regulations.* Beilstein journal of nanotechnology, **2018**. 9(1): p. 1050-1074.
12. Adul-Rasool, A.A., et al., *0, 1, 2, 3D nanostructures, Types of bulk nanostructured materials, and drug nanocrystals: an overview.* Cancer Treatment and Research Communications, **2024**: p. 100834.
13. Roduner, E., *Size matters: why nanomaterials are different.* Chemical society reviews, **2006**. 35(7): p. 583-592.
14. Dash, P. and P.K. Panda, *Top-Down Strategies Synthesis of 2D Nanomaterial.* 2D Nanomaterials: Synthesis, Properties and Applications, **2024**: p. 1-16.
15. Borane, N., et al., *Recent trends in the "bottom-up" and "top down" techniques in the synthesis and fabrication of myriad carbonaceous nanomaterials*, in *Carbon-Based Nanomaterials in Biosystems*. **2024**, Elsevier. p. 91-120.
16. Sekar, A., *Green synthesis of nanoparticles: A review.* GRT Journal of Education, Science and Technology, **2024**. 2(1): p. 19-30.
17. Yadav, A.K., *A Review on Synthesis Methods of Materials Science and Nanotechnology.*
18. Qin, Q., et al., *"Bottom-up" and "top-down" strategies toward strong cellulose-based materials.* Chemical Society Reviews, **2024**.
19. Khanna, P., A. Kaur, and D. Goyal, *Algae-based metallic nanoparticles: Synthesis, characterization and applications.* Journal of microbiological methods, **2019**. 163: p. 105656.
20. Farajpour, A., M.H. Ghayesh, and H. Farokhi, *A review on the mechanics of nanostructures.* International Journal of Engineering Science, **2018**. 133: p. 231-263.
21. Pradhan, K.K. and S. Chakraverty, *7 THEORETICAL CONCEPTS OF NANOSTRUCTURAL DYNAMIC PROBLEMS.* Nano Scaled Structural Problems, **2021**: p. 35.
22. Graham, T., *X. Liquid diffusion applied to analysis.* Philosophical transactions of the Royal Society of London, **1861**(151): p. 183-224.
23. Guyot, A., *Recent advances and challenges in the synthesis of polymer colloids.* Colloids and Surfaces A: Physicochemical and Engineering Aspects, **1999**. 153(1-3): p. 11-21.
24. Castelvetro, V. and C. De Vita, *Nanostructured hybrid materials from aqueous polymer dispersions.* Advances in Colloid and Interface Science, **2004**. 108: p. 167-185.

25. Ostwald, W., *Zur Systematik der Kolloide.* Zeitschrift für Chemie und Industrie der Kolloide, **1907**. 1: p. 331-341.
26. Thomas, J.M., *Colloidal metals: past, present and future.* Pure and Applied Chemistry, **1988**. 60(10): p. 1517-1528.
27. Faraday, M., *X. The Bakerian Lecture.—Experimental relations of gold (and other metals) to light.* Philosophical transactions of the Royal Society of London, **1857**(147): p. 145-181.
28. Alivisatos, A.P., *Semiconductor clusters, nanocrystals, and quantum dots.* science, **1996**. 271(5251): p. 933-937.
29. Yin, Y. and A.P. Alivisatos, *Colloidal nanocrystal synthesis and the organic–inorganic interface.* Nature, **2005**. 437(7059): p. 664-670.
30. Evans, D.F. and H. Wennerström, *The colloidal domain: where physics, chemistry, biology, and technology meet.* **1999**.
31. Sun, F., N.E. Brunk, and V. Jadhao, *Shape control of deformable charge-patterned nanoparticles.* Physical Review E, **2023**. 107(1): p. 014502.
32. Cassidy, J., et al., *Shape Control of Colloidal Semiconductor Nanocrystals through Thermodynamically Driven Aggregative Growth.* Chemistry of Materials, **2022**. 34(5): p. 2484-2494.
33. Beaton, G., et al., *Silver Nanoparticle on Alumina Films Tailored for Surface-enhanced Raman Spectroscopy and Detection of Pesticides.* ACS Applied Nano Materials, **2022**. 5(12): p. 18561-18567.
34. Varanda, L.C., et al., *Size and shape-controlled nanomaterials based on modified polyol and thermal decomposition approaches. A brief review.* Anais da Academia Brasileira de Ciências, **2019**. 91: p. e20181180.
35. Shuang, E., et al., *Shape control of carbon nanoparticles via a simple anion-directed strategy for precise endoplasmic reticulum-targeted imaging.* Angewandte Chemie, **2023**. 135(44): p. e202311008.
36. Kumar, Y., et al., *Functionalized nanoparticles: Tailoring properties through surface energetics and coordination chemistry for advanced biomedical applications.* Nanoscale, **2023**. 15(13): p. 6075-6104.
37. Martí, G., et al., *Surface-Functionalized Nanoparticles as Catalysts for Artificial Photosynthesis.* Advanced Energy Materials, **2023**. 13(21): p. 2300282.
38. Jing, X., et al., *Surface engineering of colloidal nanoparticles.* Materials Horizons, **2023**. 10(4): p. 1185-1209.
39. Korshed, P., et al., *Antibacterial mechanisms of a novel type picosecond laser-generated silver-titanium nanoparticles and their toxicity to human cells.* International Journal of Nanomedicine, **2018**: p. 89-101.
40. Phong, N.T.P., N.V.K. Thanh, and P.H. Phuong. *Fabrication of antibacterial water filter by coating silver nanoparticles on flexible polyurethane foams*. in *Journal of Physics: Conference Series*. 2009. IOP Publishing.
41. Atiyeh, B.S., et al., *Effect of silver on burn wound infection control and healing: review of the literature.* burns, **2007**. 33(2): p. 139-148.
42. Laxminarayan, R., et al., *Antibiotic resistance—the need for global solutions.* The Lancet infectious diseases, **2013**. 13(12): p. 1057-1098.
43. Singh, M., et al., *Silver nanowires as prospective carriers for drug delivery in cancer treatment: An in vitro biocompatibility study on lung adenocarcinoma cells and fibroblasts.* European Journal of Nanomedicine, **2013**. 5(4): p. 195-204.
44. Xia, Y., et al., *One-dimensional nanostructures: synthesis, characterization, and applications.* Advanced materials, **2003**. 15(5): p. 353-389.
45. Huang, Z., et al., *Controllable synthesis and biomedical applications of silver nanomaterials.* Journal of nanoscience and nanotechnology, **2011**. 11(11): p. 9395-9408.
46. Korte, K., *Rapid Synthesis of Silver Nanowires.*

47. Liang, H., et al., *Controlled synthesis of uniform silver nanospheres.* The Journal of Physical Chemistry C, **2010**. 114(16): p. 7427-7431.
48. Bachenheimer, L., et al., *Degradation mechanism of Ag nanorods for surface enhanced Raman spectroscopy.* Scientific reports, **2017**. 7(1): p. 16282.
49. Hoop, M., et al., *Magnetically driven silver-coated nanocoils for efficient bacterial contact killing.* Advanced Functional Materials, **2016**. 26(7): p. 1063-1069.
50. Dhapte, V., et al., *Probing the wound healing potential of biogenic silver nanoparticles.* Journal of wound care, **2014**. 23(9): p. 431-441.
51. Ge, L., et al., *Nanosilver particles in medical applications: synthesis, performance, and toxicity.* International journal of nanomedicine, **2014**: p. 2399-2407.
52. Jung, W.K., et al., *Antibacterial activity and mechanism of action of the silver ion in Staphylococcus aureus and Escherichia coli.* Applied and environmental microbiology, **2008**. 74(7): p. 2171-2178.
53. Kalpana, D. and Y.S. Lee, *Synthesis and characterization of bactericidal silver nanoparticles using cultural filtrate of simulated microgravity grown Klebsiella pneumoniae.* Enzyme and microbial technology, **2013**. 52(3): p. 151-156.
54. Ovington, L.G., *The truth about silver.* Ostomy/wound management, **2004**. 50(9A Suppl): p. 1S-10S.
55. Jones, M.R., et al., *Templated techniques for the synthesis and assembly of plasmonic nanostructures.* Chemical reviews, **2011**. 111(6): p. 3736-3827.
56. Vilayurganapathy, S., et al., *Silver nanorod arrays for photocathode applications.* Applied Physics Letters, **2013**. 103(16).
57. Du, Y., et al., *SERS enhancement dependence on the diameter and aspect ratio of silver-nanowire array fabricated by anodic aluminium oxide template.* Applied Surface Science, **2008**. 255(5): p. 1901-1905.
58. Li, A., et al., *Hexagonal pore arrays with a 50–420 nm interpore distance formed by self-organization in anodic alumina.* Journal of applied physics, **1998**. 84(11): p. 6023-6026.
59. Zhang, C., et al., *Single-crystalline silver nanowire arrays directly synthesized onto substrates by template-assisted chemical wetting.* Materialia, **2020**. 9: p. 100529.
60. Yang, L., et al., *Silver nanowires: from synthesis, growth mechanism, device fabrications to prospective engineered applications.* Engineered Science, **2023**. 23: p. 808.
61. Murphy, C.J. and N.R. Jana, *Controlling the aspect ratio of inorganic nanorods and nanowires.* Advanced Materials, **2002**. 14(1): p. 80-82.
62. Jana, N.R., L. Gearheart, and C.J. Murphy, *Wet chemical synthesis of silver nanorods and nanowires of controllable aspect ratioElectronic supplementary information (ESI) available: UV–VIS spectra of silver nanorods. See* *http://www. rsc. org/suppdata/cc/b1/b100521i.* Chemical Communications, **2001**(7): p. 617-618.
63. Hong, B.H., et al., *Ultrathin single-crystalline silver nanowire arrays formed in an ambient solution phase.* Science, **2001**. 294(5541): p. 348-351.
64. Sun, Y. and Y. Xia, *Large-scale synthesis of uniform silver nanowires through a soft, self-seeding, polyol process.* Advanced Materials, **2002**. 14(11): p. 833-837.
65. Sun, Y., et al., *Uniform silver nanowires synthesis by reducing AgNO3 with ethylene glycol in the presence of seeds and poly (vinyl pyrrolidone).* Chemistry of Materials, **2002**. 14(11): p. 4736-4745.
66. Jia, D., et al., *Synthesis of very thin Ag nanowires with fewer particles by suppressing secondary seeding.* CrystEngComm, **2017**. 19(1): p. 148-153.
67. Xia, Y., et al., *Shape-controlled synthesis of metal nanocrystals: simple chemistry meets complex physics?* Angewandte Chemie International Edition, **2009**. 48(1): p. 60-103.
68. Bergin, S.M., et al., *The effect of nanowire length and diameter on the properties of transparent, conducting nanowire films.* Nanoscale, **2012**. 4(6): p. 1996-2004.
69. Viau, G., F. Fiévet-Vincent, and F. Fievet, *Nucleation and growth of bimetallic CoNi and FeNi monodisperse particles prepared in polyols.* Solid State Ionics, **1996**. 84(3-4): p. 259-270.

70. Gao, Y., et al., *Growth mechanism of silver nanowires synthesized by polyvinylpyrrolidone-assisted polyol reduction.* Journal of Physics D: Applied Physics, **2005**. 38(7): p. 1061.
71. Mao, H., et al., *One-dimensional silver nanowires synthesized by self-seeding polyol process.* Journal of nanoparticle research, **2012**. 14: p. 1-15.
72. Rycenga, M., et al., *Controlling the synthesis and assembly of silver nanostructures for plasmonic applications.* Chemical reviews, **2011**. 111(6): p. 3669-3712.
73. Jones, R.S., R.R. Draheim, and M. Roldo, *Silver nanowires: Synthesis, antibacterial activity and biomedical applications.* Applied Sciences, **2018**. 8(5): p. 673.
74. Korte, K.E., S.E. Skrabalak, and Y. Xia, *Rapid synthesis of silver nanowires through a CuCl-or CuCl 2-mediated polyol process.* Journal of Materials Chemistry, **2008**. 18(4): p. 437-441.
75. Chen, D., et al., *Convenient synthesis of silver nanowires with adjustable diameters via a solvothermal method.* Journal of Colloid and Interface Science, **2010**. 344(2): p. 286-291.
76. Geim, A.K. and K.S. Novoselov, *The rise of graphene.* Nature materials, **2007**. 6(3): p. 183-191.
77. Gerstner, E., *Nobel prize 2010: Andre geim & konstantin novoselov.* Nature Physics, **2010**. 6(11): p. 836-836.
78. Randviir, E.P., D.A. Brownson, and C.E. Banks, *A decade of graphene research: production, applications and outlook.* Materials Today, **2014**. 17(9): p. 426-432.
79. Molina, J., F. Cases, and L.M. Moretto, *Graphene-based materials for the electrochemical determination of hazardous ions.* Analytica Chimica Acta, **2016**. 946: p. 9-39.
80. Hussain, A., et al., *Synthesis of graphene from solid carbon sources: A focused review.* Materials Chemistry and Physics, **2020**. 248: p. 122924.
81. Aderibigbe, B., I. Aderibigbe, and P. Popoola, *Design and biological evaluation of delivery systems containing bisphosphonates.* Pharmaceutics, **2016**. 9(1): p. 2.
82. Lee, X.J., et al., *Review on graphene and its derivatives: Synthesis methods and potential industrial implementation.* Journal of the Taiwan Institute of Chemical Engineers, **2019**. 98: p. 163-180.
83. Shen, Y., Q. Fang, and B. Chen, *Environmental applications of three-dimensional graphene-based macrostructures: adsorption, transformation, and detection.* Environmental Science & Technology, **2015**. 49(1): p. 67-84.
84. Yang, K., L. Feng, and Z. Liu, *Stimuli responsive drug delivery systems based on nano-graphene for cancer therapy.* Advanced drug delivery reviews, **2016**. 105: p. 228-241.
85. Singh, Z., *Applications and toxicity of graphene family nanomaterials and their composites.* Nanotechnology, science and applications, **2016**: p. 15-28.
86. Somani, P.R., S.P. Somani, and M. Umeno, *Planer nano-graphenes from camphor by CVD.* Chemical Physics Letters, **2006**. 430(1-3): p. 56-59.
87. Lim, J.Y., et al., *Recent trends in the synthesis of graphene and graphene oxide based nanomaterials for removal of heavy metals—A review.* Journal of Industrial and Engineering Chemistry, **2018**. 66: p. 29-44.
88. Kriti, et al., *Advances of Graphene Oxide in the Field of Microbiology*, in *Microbiology-2.0 Update for a Sustainable Future*. **2024**, Springer. p. 235-267.
89. Viprya, P., D. Kumar, and S. Kowshik, *Study of Different Properties of Graphene Oxide (GO) and Reduced Graphene Oxide (rGO).* Engineering Proceedings, **2023**. 59(1): p. 84.
90. Farooq, N., et al., *Graphene Oxide and Based Materials: Synthesis, Properties, and Applications–A Comprehensive.* **2024**.
91. Pasricha, R., S. Gupta, and A.K. Srivastava, *A facile and novel synthesis of Ag–graphene-based nanocomposites.* Small, **2009**. 5(20): p. 2253-2259.
92. Pei, S. and H.-M. Cheng, *The reduction of graphene oxide.* Carbon, **2012**. 50(9): p. 3210-3228.
93. Rowley, A., et al., *Graphene oxide membranes: Controlled laser reduction for sensing applications.* C, **2023**. 9(3): p. 74.
94. Singh, V., et al., *Graphene based materials: past, present and future.* Progress in materials science, **2011**. 56(8): p. 1178-1271.

95. Abergel, D., A. Russell, and V.I. Fal'ko, *Visibility of graphene flakes on a dielectric substrate.* Applied Physics Letters, **2007**. 91(6).
96. Niyogi, S., et al., *Spectroscopy of covalently functionalized graphene.* Nano letters, **2010**. 10(10): p. 4061-4066.
97. Sinitskii, A., et al., *Graphene nanoribbon devices produced by oxidative unzipping of carbon nanotubes.* ACS nano, **2010**. 4(9): p. 5405-5413.
98. Kosynkin, D.V., et al., *Longitudinal unzipping of carbon nanotubes to form graphene nanoribbons.* Nature, **2009**. 458(7240): p. 872-876.
99. Kostarelos, K., et al., *Cellular uptake of functionalized carbon nanotubes is independent of functional group and cell type.* Nature nanotechnology, **2007**. 2(2): p. 108-113.
100. Georgakilas, V., et al., *Multipurpose organically modified carbon nanotubes: from functionalization to nanotube composites.* Journal of the American Chemical Society, **2008**. 130(27): p. 8733-8740.
101. Georgakilas, V., et al., *Organic functionalisation of graphenes.* Chemical Communications, **2010**. 46(10): p. 1766-1768.
102. Bourlinos, A.B., et al., *Liquid-phase exfoliation of graphite towards solubilized graphenes.* small, **2009**. 5(16): p. 1841-1845.
103. Ou, B., et al., *Covalent functionalization of graphene with poly (methyl methacrylate) by atom transfer radical polymerization at room temperature.* Polymer Chemistry, **2012**. 3(10): p. 2768-2775.
104. Yao, Y., et al., *Covalent functionalization of graphene with polythiophene through a Suzuki coupling reaction.* Rsc Advances, **2015**. 5(53): p. 42754-42761.
105. Tian, B., et al., *Photothermally enhanced photodynamic therapy delivered by nano-graphene oxide.* ACS nano, **2011**. 5(9): p. 7000-7009.
106. Kang, X., et al., *Glucose oxidase–graphene–chitosan modified electrode for direct electrochemistry and glucose sensing.* Biosensors and Bioelectronics, **2009**. 25(4): p. 901-905.
107. Salavagione, H.J., G. Martínez, and G. Ellis, *Recent advances in the covalent modification of graphene with polymers.* Macromolecular rapid communications, **2011**. 32(22): p. 1771-1789.
108. Singh, N.J., et al., *Designing ionophores and molecular nanotubes based on molecular recognition.* Supramolecular Chemistry, **2007**. 19(4-5): p. 321-332.
109. Meyer, E.A., R.K. Castellano, and F. Diederich, *Interactions with aromatic rings in chemical and biological recognition.* Angewandte Chemie International Edition, **2003**. 42(11): p. 1210-1250.
110. Hong, B.H., et al., *Extracting subnanometer single shells from ultralong multiwalled carbon nanotubes.* Proceedings of the National Academy of Sciences, **2005**. 102(40): p. 14155-14158.
111. Riley, K.E., et al., *Stabilization and structure calculations for noncovalent interactions in extended molecular systems based on wave function and density functional theories.* Chemical Reviews, **2010**. 110(9): p. 5023-5063.
112. Kim, K.S., P. Tarakeshwar, and J.Y. Lee, *Molecular clusters of π-systems: theoretical studies of structures, spectra, and origin of interaction energies.* Chemical reviews, **2000**. 100(11): p. 4145-4186.
113. Stankovich, S., et al., *Stable aqueous dispersions of graphitic nanoplatelets via the reduction of exfoliated graphite oxide in the presence of poly (sodium 4-styrenesulfonate).* Journal of Materials Chemistry, **2006**. 16(2): p. 155-158.
114. Xu, Y., et al., *Flexible graphene films via the filtration of water-soluble noncovalent functionalized graphene sheets.* Journal of the American Chemical Society, **2008**. 130(18): p. 5856-5857.
115. Su, Q., et al., *Composites of graphene with large aromatic molecules.* Adv. Mater, **2009**. 21(31): p. 3191-3195.
116. Englert, J.M., et al., *Soluble Graphene: Soluble Graphene: Generation of Aqueous Graphene Solutions Aided by a Perylenebisimide-Based Bolaamphiphile (Adv. Mater. 42/2009).* Advanced Materials, **2009**. 21(42).

117. Qian, W., et al., *Solvothermal-assisted exfoliation process to produce graphene with high yield and high quality.* Nano Research, **2009**. 2: p. 706-712.
118. Ghosh, A., et al., *Noncovalent functionalization, exfoliation, and solubilization of graphene in water by employing a fluorescent coronene carboxylate.* Chemistry–A European Journal, **2010**. 9(16): p. 2700-2704.
119. Patil, A.J., et al., *Aqueous stabilization and self-assembly of graphene sheets into layered bio-nanocomposites using DNA.* Advanced materials, **2009**. 21(31): p. 3159-3164.
120. Georgakilas, V., et al., *Noncovalent functionalization of graphene and graphene oxide for energy materials, biosensing, catalytic, and biomedical applications.* Chemical reviews, **2016**. 116(9): p. 5464-5519.
121. Ingrosso, C., et al., *Solvent dispersible nanocomposite based on Reduced Graphene Oxide and in-situ decorated gold nanoparticles.* Carbon, **2019**. 152: p. 777-787.
122. Lu, G., et al., *Facile, noncovalent decoration of graphene oxide sheets with nanocrystals.* Nano Research, **2009**. 2: p. 192-200.
123. Zhou, X., et al., *In situ synthesis of metal nanoparticles on single-layer graphene oxide and reduced graphene oxide surfaces.* The Journal of Physical Chemistry C, **2009**. 113(25): p. 10842-10846.
124. Goncalves, G., et al., *Surface modification of graphene nanosheets with gold nanoparticles: the role of oxygen moieties at graphene surface on gold nucleation and growth.* Chemistry of Materials, **2009**. 21(20): p. 4796-4802.
125. Jasuja, K. and V. Berry, *Implantation and growth of dendritic gold nanostructures on graphene derivatives: electrical property tailoring and Raman enhancement.* ACS nano, **2009**. 3(8): p. 2358-2366.
126. Huang, X., et al., *Reduced graphene oxide-templated photochemical synthesis and in situ assembly of Au nanodots to orderly patterned Au nanodot chains.* small, **2010**. 6(4): p. 513-516.
127. Hassan, H.M., et al., *Microwave synthesis of graphene sheets supporting metal nanocrystals in aqueous and organic media.* Journal of Materials Chemistry, **2009**. 19(23): p. 3832-3837.
128. Johnson, J.L., et al., *Hydrogen sensing using Pd-functionalized multi-layer graphene nanoribbon networks.* Advanced materials, **2010**. 22(43): p. 4877-4880.
129. Si, Y. and E.T. Samulski, *Exfoliated graphene separated by platinum nanoparticles.* Chemistry of Materials, **2008**. 20(21): p. 6792-6797.
130. Wang, H., et al., *Nanocrystal growth on graphene with various degrees of oxidation.* Journal of the American Chemical Society, **2010**. 132(10): p. 3270-3271.
131. Scheuermann, G.M., et al., *Palladium nanoparticles on graphite oxide and its functionalized graphene derivatives as highly active catalysts for the Suzuki− Miyaura coupling reaction.* Journal of the American Chemical Society, **2009**. 131(23): p. 8262-8270.
132. Guo, S., et al., *Platinum nanoparticle ensemble-on-graphene hybrid nanosheet: one-pot, rapid synthesis, and used as new electrode material for electrochemical sensing.* ACS nano, **2010**. 4(7): p. 3959-3968.
133. Brust, M., et al., *Synthesis of thiol-derivatised gold nanoparticles in a two-phase liquid–liquid system.* Journal of the Chemical Society, Chemical Communications, **1994**(7): p. 801-802.
134. Vischio, F., et al., *Au nanoparticles decorated nanographene oxide-based platform: Synthesis, functionalization and assessment of photothermal activity.* Biomaterials Advances, **2023**. 145: p. 213272.
135. Ingrosso, C., et al., *Au nanoparticle in situ decorated RGO nanocomposites for highly sensitive electrochemical genosensors.* Journal of Materials Chemistry B, **2019**. 7(5): p. 768-777.
136. Ingrosso, C., et al., *Au nanoparticle decorated reduced graphene oxide and its electroanalytical characterization for label free dopamine detection.* Materials Advances, **2024**. 5(2): p. 549-560.
137. Chaudhury, D., et al., *Rapid regulation of depression-related behaviours by control of midbrain dopamine neurons.* Nature, **2013**. 493(7433): p. 532-536.
138. Wang, D., et al., *Self-assembled TiO2–graphene hybrid nanostructures for enhanced Li-ion insertion.* ACS nano, **2009**. 3(4): p. 907-914.

139. Liu, J., et al., *Self-assembling TiO2 nanorods on large graphene oxide sheets at a two-phase interface and their anti-recombination in photocatalytic applications.* Advanced Functional Materials, **2010**. 20(23): p. 4175-4181.
140. Son, J.Y., et al., *NiO resistive random access memory nanocapacitor array on graphene.* ACS nano, **2010**. 4(5): p. 2655-2658.
141. Wu, S., et al., *Electrochemical deposition of semiconductor oxides on reduced graphene oxide-based flexible, transparent, and conductive electrodes.* The Journal of Physical Chemistry C, **2010**. 114(27): p. 11816-11821.
142. Yan, J., et al., *Fast and reversible surface redox reaction of graphene–MnO2 composites as supercapacitor electrodes.* Carbon, **2010**. 48(13): p. 3825-3833.
143. Cao, A., et al., *A facile one-step method to produce graphene–CdS quantum dot nanocomposites as promising optoelectronic materials.* Advanced materials, **2010**. 22(1): p. 103-106.

CHAPTER 2

Innovative Green Synthesis of Ag Nanowire-Decorated Nanocomposites on Reduced Graphene Oxide

2.1 Introduction

The growing interest in hybrid nanocomposites integrating graphene with colloidal inorganic nanoparticles (NPs), stems from the synergistic combination of their distinct functionalities. This integration produces nanostructures with unique properties and enhanced performance, offering significant potential for diverse applications, including electronic circuits, (bio)sensors, electrocatalysis, photocatalysis, antimicrobial coatings, and biomedicine [1-4].

Reduced Graphene Oxide (RGO), a derivative of graphene, retains many of graphene's remarkable structural characteristics, which are largely attributed to its atomically thin structure and unique morphology. Its optical transparency in the visible spectrum, mechanical flexibility, high electrical conductivity, and excellent in-plane thermal conductivity makes it an exceptional material for various applications [5]. On the other hand, colloidal inorganic NPs exhibit intriguing chemical and physical properties dependent on morphology and crystalline phase, with tuneable surface reactivity through diverse chemical approaches [6].

The extensive surface area and high chemical reactivity of RGO make it an ideal scaffold for the fabrication of highly functional hybrid nanocomposites incorporating colloidal inorganic nanostructures. The reactive surface chemistry of RGO enables diverse chemical decoration strategies, facilitating the integration of various nanostructures [7]. Among the inorganic nanostructures of current research focus for combination with RGO, silver nanowires (Ag NWs) stand out. Renowned for their high transmittance, robust durability, antimicrobial properties, plasmonic features, and high electrical and thermal conductivity, Ag NWs find applications in diverse fields such as Surface Enhanced Raman Scattering (SERS), pressure and temperature sensors, transparent heaters, and electrodes of solar cells and touch screen panels [8-10].

When integrated with Ag NWs, RGO may serve as both a support and protective layer, preventing NWs aggregation and oxidation, leading to hybrid nanocomposites that hold significant potential for a wide range of applications, including flexible and transparent electrodes, devices for electromagnetic interference shielding, SERS sensors, thermal management systems, and materials with antimicrobial properties [11-15]. Despite the large number of functionalities achievable in these materials, the literature predominantly reports on nanocomposites prepared by mixing pre-synthesized Ag NWs with graphene derivatives. In such cases, the electron coupling between components is weaker than in nanocomposites where the NWs are directly chemically anchored to the graphene basal plane, limiting the exploitation of the full potential arising from the combination of material properties. This limitation likely stems from the complexity of the Ag NWs synthesis, influenced by various experimental conditions affecting their anisotropic growth and wire-to-particle yields.

The *in-situ* synthesis approaches of Ag NWs onto RGO remain underexplored in the existing literature. Specifically, the application of the self-seeding polyol method for synthesizing Ag NWs in the presence of graphene derivatives has not been extensively investigated, although this approach is well-regarded for its ability to precisely control NWs' morphology while achieving a high wire-to-particle yield. The synthesis of such nanocomposites, in the literature, is primarily conducted through a solvothermal approach, commencing with graphene oxide dispersed in a solution containing polyvinylpyrrolidone (PVP) as a capping and stabilizing agent, ethylene glycol (EG) as both reductant and solvent, and sodium chloride (NaCl) as the salt regulating the concentration of Ag(I) ions [11, 12]. However, these studies have reported on only limited insights into the formation mechanism of the Ag NWs on the RGO basal plane.

In our study we introduce a novel hybrid nanocomposite comprising histidine-functionalized RGO (His-RGO) sheets decorated with Ag NWs, achieved by modifying the self-seeding polyol procedure of Ag NWs. The nanocomposite is synthesized by injecting His-RGO sheets into the Ag NW synthesis solution, where Ag NWs form onto the His-RGO basal plane through the reduction of silver nitrate ($AgNO_3$) with EG, in presence of PVP and NaCl salt. His is selected as the linker between RGO and Ag NWs due to its ability to coordinate the Ag NWs surface and simultaneously intercalate and functionalize the RGO sheets through stable aromatic π-π stacking interactions. This choice avoids introducing structural defects to RGO that could detrimentally affect its electronic and interlayer thermal conductivity.

A systematic study of experimental parameters, including the injection mode of His-RGO, dissociation state of His-RGO, reaction time, stirring rate, molecular weight of PVP, PVP:$AgNO_3$ molar ratio, and His-RGO:$AgNO_3$ w/w, is conducted. Simultaneously, a comprehensive characterization of the spectroscopic and morphological properties of the achieved hybrid nanocomposites provides insights into the synthesis mechanism.

2.2 Experimental Section

2.2.1 Materials

Reduced Graphene Oxide (RGO, 1.6 nm flakes) was purchased from Graphene Supermarket, polyvinylpyrrolidone (PVP) (monomer based calculation, Mw= 55 KDa and 360 KDa), NaCl (> 99.8 %), silver nitrate ($AgNO_3$, 99.9999%), acetone (99.9%), ethanol (> 99.9 %), 1-octadecene (ODE), DL-histidine (His, > 99%) and 1,2-ethandiol (EG, > 99%, Honeywell) were purchased from Sigma Aldrich.

2.2.2 Exfoliation and functionalization of RGO with Histidine (His)

Exfoliation and functionalization of RGO with His were performed by sonication of a dispersion, 5 mg mL^{-1} in RGO and 8 mg mL^{-1} in His, in Milli-Q water at pH 11 [16, 17]. The dispersion was sonicated for 8 h to allow exfoliation and functionalization of the RGO sheets with His, and it was purified from the excess of His by three cycles of centrifugation (40000 rpm, 30 min) and re-dispersion in Milli-Q water. After the third centrifugation, the His-RGO pellet was re-dispersed in Milli-Q water, at both pH 7 and at pH 11, and was finally isolated by centrifugation (40000 rpm, 30 min) and dried at 70°C in an oven.

2.2.3 Synthesis of Ag NWs

Ag NWs were synthesized by the polyol synthesis approach reported by S. Coskun et al. [18]. In a typical experiment, a vial filled up with a solution of 250 mg of PVP (Mw= 360 KDa) and 3.5 mg of NaCl in 5 mL of EG, closed with a septum, was heated up to 170°C by immersion in an oil bath placed onto a hotplate, and stirred at 600 rpm. To this solution, ten injections of 0.25 mL of a 25 mg mL^{-1} $AgNO_3$ solution in EG, were added, every 6 min, by a syringe. At the end of the injections, the vial was allowed to stir at 600 rpm and at 170°C for 90 min, and then, was air-cooled down to room temperature, to stop the reaction. The NWs were purified from the excess of PVP and EG by three cycles of centrifugation (10000 rpm, 30 min) with acetone and re-dispersion in ethanol, and were finally dispersed in ethanol.

2.2.4 Synthesis of hybrid nanocomposites formed of His functionalized RGO decorated with Ag NWs.

The hybrid nanocomposites formed of His-RGO decorated with Ag NWs (His-RGO/Ag NWs) were synthesized modifying the polyol synthesis approach of Ag NWs [18], by injecting the His-RGO complex in the synthesis solution of the Ag NWs.

A first experiment involved introducing 2.5 mL of a 25 mg mL^{-1} $AgNO_3$ in EG through ten 0.25 mL injections, spaced 6 min apart into a mixture comprising 250 mg of PVP, 3.5 mg of NaCl, and 5 mg of His-RGO, in 5 mL of EG. The reaction setup was a vial sealed with a septum, heated up to 170°C onto a hotplate by using an oil bath, and stirred at 600 rpm. Following the completion of the ten $AgNO_3$ injections, the vial continued to be stirred at 170°C and 600 rpm for 90 min. Subsequently, the reaction was quenched by allowing the vial to air-cool down to room temperature.

In a second experiment, a dispersion containing 5 mg of His-RGO in 2 mL of EG pre-heated up to 170°C was injected into a mixture comprising 250 mg of PVP, 3.5 mg of NaCl, and 5 mg of His-RGO in 5 mL of EG, at the conclusion of the ten 2.5 mL injections of a 25 mg mL^{-1} $AgNO_3$ in EG. This composite was contained in a vial sealed with a septum, heated up to 170°C using an oil bath, and stirred at 600 rpm. Following the completion of the $AgNO_3$ injections, the vial continued to be stirred at 600 rpm and 170°C for 90 min, after which it was air-cooled to room temperature.

A third set of experiments was conducted by injecting a dispersion of His-RGO in 2 mL of pre-heated (170°C) EG into the synthesis solution containing PVP and 3.5 mg of NaCl in 5 mL of EG. This mixture was placed in a vial sealed with a septum, heated up to 170°C onto a hotplate via immersion in an oil bath, and subjected to stirring. The injection occurred between the seventh and eighth of the ten 0.25 mL injections of the 2.5 mL 25 mg mL^{-1} $AgNO_3$ solution in EG. Subsequently, the vial was air-cooled down to room temperature. In this series of experiments, variations were introduced, including 5 mg and 10 mg of His-RGO in 2 mL of EG (with His-RGO powder isolated from Milli-Q water solutions at pH 7 and pH 11 having ζ-*potential* of -20.1±1.5 mV and –24.5±1.8 mV, respectively), 250 mg and 375 mg of PVP (at molecular weights of 55 kDa and 360 kDa), reaction times of 1.5 h, 2.5 h, 6.5 h, and 7.5 h, and stirring rates of both 600 rpm and 200 rpm.

Following the syntheses, the obtained hybrid nanocomposites underwent purification from excess PVP and EG through six cycles of centrifugation with acetone (10000 rpm, 10 min) and subsequent re-dispersion in ethanol. The resulting hybrid nanocomposites were then re-dispersed in ethanol.

2.2.5 Characterization techniques

Steady state UV-Vis absorption spectroscopy investigation was performed by a Cary Varian 5000 spectrophotometer at room temperature.

Surface charge of the His-RGO complex was determined by ζ-*potential* measurements carried out by laser Doppler velocimetry method, after sample dilution in Milli-Q water. Data were reported as mean values ± standard deviation of three independent experiments.

Raman spectra were collected by using a LabRAM HR Horiba-Jobin Yvon spectrometer with a 532 nm continuous excitation laser source. Measurements were carried out under ambient conditions at a low laser power (1 mW) to avoid laser-induced damage of the sample. The Raman signal from the silicon wafer at 520 cm^{-1} was used to calibrate the spectrometer and accuracy of the spectral measurement was 1 cm^{-1}.

Mid-infrared spectra were acquired by a Varian 670-IR spectrometer equipped with a DTGS (Deuterated Tryglycine Sulfate) detector having a spectral resolution of 4 cm^{-1}. For attenuated total reflection (ATR) measurements, a one-bounce 2 mm diameter diamond microprism was used as internal reflection element (IRE). The samples were deposited by drop casting directly onto the upper face of the diamond crystal and the solvent was allowed to evaporate.

Transmission Electron Microscopy (TEM) images were collected by a JEOL JEM-1011 microscope working at an accelerating voltage of 100 kV, equipped by a high-contrast objective lens and a W filament as electron source. Under these conditions, the ultimate point resolution of the microscope was 0.34 nm. The TEM images were recorded by a Gatan SC-1000 Orius Camera, equipped with a fiber-optical coupled 11 Mp CCD. The samples were prepared by dipping a 300 mesh amorphous carbon-coated Cu grid in ethanol dispersions of neat Ag NWs and of His-RGO/Ag NWs, then letting the solvent to evaporate. Size statistical analyses of the NWs average length and diameter were performed by the freeware Image J analysis program.

2.3 Preparation and characterization of the His-functionalized RGO complex

Reduced graphene oxide (RGO) flakes, obtained commercially, were effectively exfoliated and functionalized with histidine (His) by using a process that involved repeated cycles of sonication and centrifugation, followed by steps of purification that were performed by 4 cycles of ultracentrifugation and redispersion of the pellet in Milli-Q water. The functionalization was conducted at two different pH conditions: neutral pH and pH 11, because His's carboxyl, amino, and imidazole groups undergo pH-dependent dissociation, characterized by four pKa values (1.8, 6.0, 9.1, and 14.0) as shown in the figure 2.1. Thus, different pH conditions influence the ionization state of the His's functional groups, which in turn affects its ability to bind other molecular species by supramolecular interactions [19].

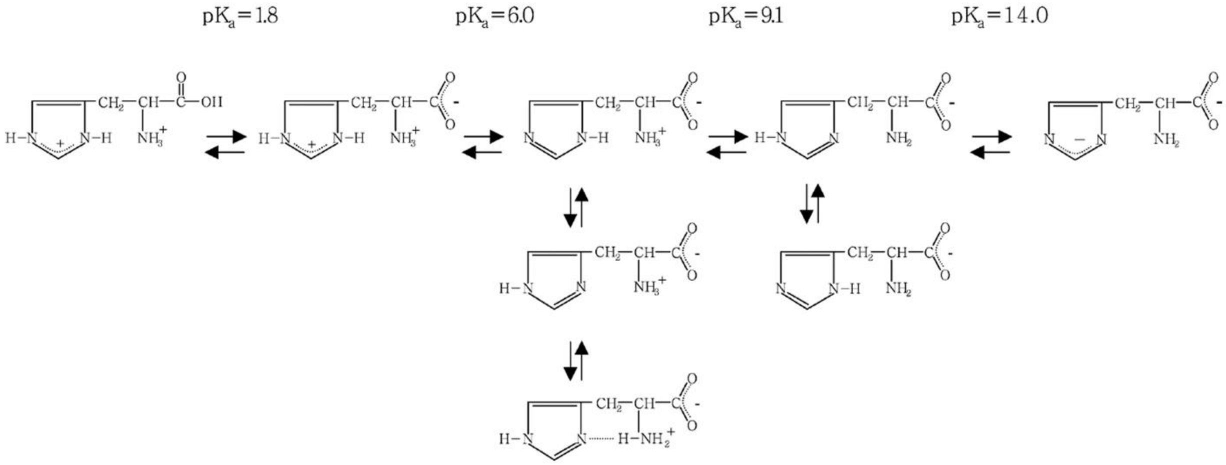

Figure 2.1 Proposed structures of the various protonation states and tautomers of L-histidine in aqueous solution, with pKa values [19].

In regards of the exfoliation and functionalization of RGO, it has been demonstrated that His acts as a molecular wedge by intercalating between RGO multilayers, binding the basal plane of RGO through aromatic π–π stacking interactions by its imidazole ring [16, 17] (Figure 2.2A). To optimize these interactions, it is crucial to sensibly select the pH conditions, as at pH lower than 7, imidazole rings would be positively charged, thus weakening the aromatic π–π stacking interactions, thereby reducing the efficiency of His as a functionalizing agent [20], and pH values greater than 11 create highly basic condition, that can induce nucleophilic reactions onto the RGO basal plane. The spectroscopic properties, chemical and morphological characteristics of the obtained complex were studied by TEM, UV-Vis-NIR and FTIR-ATR absorption spectroscopy.

TEM analysis of the RGO complex exfoliated and functionalized at pH 11 indicates that RGO sheets have dimensions of few micrometers and are almost transparent to the electron beam (Figure 2.2B). The images also show regions of high contrast on the surface of the sheets due to rolled edges, ripples and wrinkles (Figure 2.2B), which can be attributed to mechanical deformations of the basal plane, induced by structural defects, vacancies and holes that generate in the graphene lattice during the reduction of GO to RGO. Importantly, the TEM image does not show the presence of residual His on the basal plane of RGO (Figure 2.2B), demonstrating the effectiveness of the purification process.

The UV-Vis-NIR absorption spectra of the His-RGO complex aqueous dispersions, which were achieved by functionalization with His solutions at neutral pH and pH 11, respectively, show an absorption peak at 277 nm, corresponding to the characteristic π-π transition of the -C=C- bond of RGO [1, 17] (Figure 2.2C). The peak of the sample prepared at pH 11 is more intense, suggesting differences in the effectiveness of the exfoliation and functionalization processes under the investigated pH conditions. A closer comparison of the baseline trends between the two samples further highlights these differences. The high intensity of the baseline signal of the His-RGO sample achieved from solution at neutral pH assesses the occurrence of scattering phenomena induced by RGO multilayers, indicating that the exfoliation process at neutral pH was less effective. Conversely, the sample prepared at pH 11 exhibits a less intense baseline signal suggesting more efficient exfoliation (Figure 2.2C). Considering these findings, it can be concluded that the exfoliation of RGO sheets at pH 11 is more effective, probably due to the negative charge of the $-COO^-$ groups of His [17] anchored onto the basal plane of RGO (Figure 2.2A) which thus causes a greater electrostatic repulsion between the RGO flakes.

In Figure 2.2D, the Raman spectra of both the unmodified RGO and His-RGO complex are presented. The RGO spectrum shows the D and G peaks of RGO at 1344 cm^{-1} and 1590 cm^{-1}, respectively. The D peak is associated with structural defects within the RGO platform, such as those found at edge-defects, grain boundaries, edge and basal plane sites incorporating oxygen atoms or other heteroatoms like nitrogen, as well as hydrocarbon chains that may originate from the reduction of GO to RGO. The G peak is linked to the in-plane vibration modes of the sp^2 carbon atoms in the hexagonal lattice structure of RGO. These peaks are also observable in the spectrum of the His-RGO complex at 1347 cm^{-1} and 1597 cm^{-1} respectively, and the intensity ratio between the G and D peaks of RGO did not change following non-covalent functionalization with His (Figure 2.2D), indicating that the functionalization did not introduce additional structural defects into the RGO sheets.

In Figure 2.2E, the FTIR-ATR spectrum of the His-RGO complex prepared at pH 11 is compared with that of an aqueous histidine solution at the same pH. The figure shows that in the higher wavenumber region, it presents the stretching of the -NH$_2$ groups (vNH$_2$) of His at 3394 cm^{-1} and the symmetrical and asymmetrical stretching of the -CH$_2$ groups (vCH$_2$) at 2988 cm^{-1} and 2901 cm^{-1}, respectively, confirming the successful functionalization of RGO (Figure 2.2E)

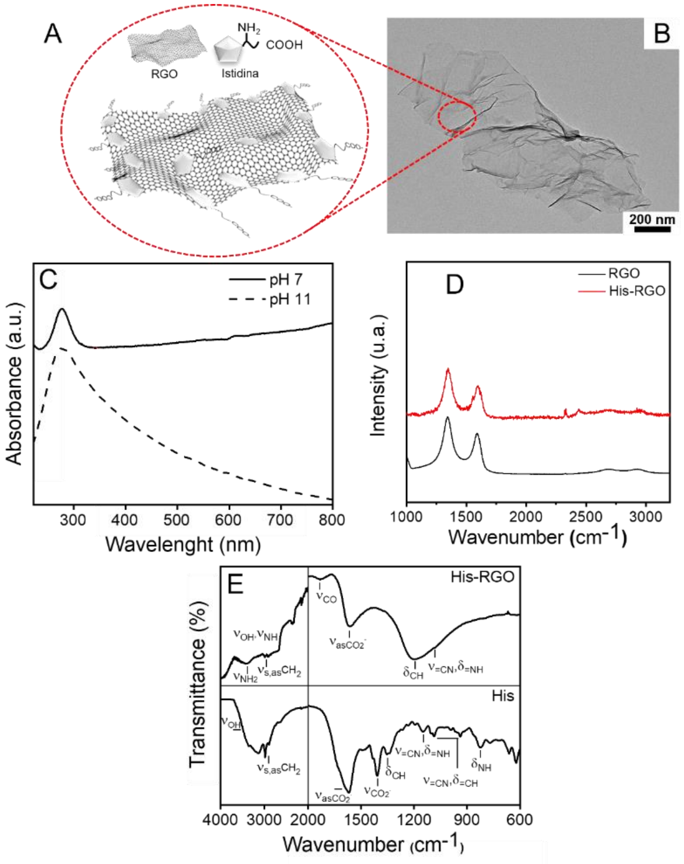

Figure 2.2 (A) Sketch of the His-RGO complex, illustrating how His interacts with the basal plane of RGO by aromatic π-π stacking interactions. **(B)** TEM micrograph of the His-RGO complex. **(C)** UV-Vis-NIR absorption spectra of His-RGO dispersion in Milli-Q water at pH 7 and 11. **(D)** Raman spectra of RGO and His-RGO. **(E)** FTIR-ATR spectrum of His-RGO at pH 11.

2.4 Self-seeding polyol synthesis of silver nanowires (Ag NWs)

The synthesis of silver nanowires (Ag NWs) was performed by using the self-seeding polyol approach of S. Coskun et al [18] . In this method, ethylene glycol (EG) was used both as a green solvent and as a reducing agent of the precursor silver nitrate ($AgNO_3$), and polyvinylpyrrolidone (PVP), which through its carbonyl group can bind the Ag surface by coordination [18], behaves as a coordinating agent sterically stabilizing the Ag cluster in growth during their nucleation and growth, preventing them from aggregating, as well as the prepared Ag NWs that are dispersible in solutions of hydrophilic solvents.

In a typical synthesis of NWs [18], a solution (A) containing 250 mg of PVP, 3.5 mg of NaCl and 5 ml of EG, was heated up to 170°C, in a septum-sealed vial, immersed in an oil bath, and was then stirred at 600 rpm. A solution (B), prepared by dissolving 50 mg of $AgNO_3$ in 2.5 ml of EG, was then added to solution (A), every 6 min, by consecutive injections of 0.25 ml each, with a 1 mL syringe. At the end of the injection of (B) into (A), the vial was left under stirring at 600 rpm, and at 170°C for 90 min, to favor the growth of the NWs, and the reaction was stopped by cooling the vial at room temperature.

During the synthesis, the color of the solution undergoes several noticeable changes. The solution changes color from milky white, immediately after the first injection of solution B (Figure 2.3A), to orange (Figure 2.3B), which becomes gradually more intense upon each subsequent injection of $AgNO_3$. The solution turns brown at the sixth injection (Figure 2.3E) and grey immediately after the seventh injection of AgNO3 (Figure 2.3F) These color changes indicate the progressive reduction of Ag+ ions and the formation of Ag nanostructures within the solution.

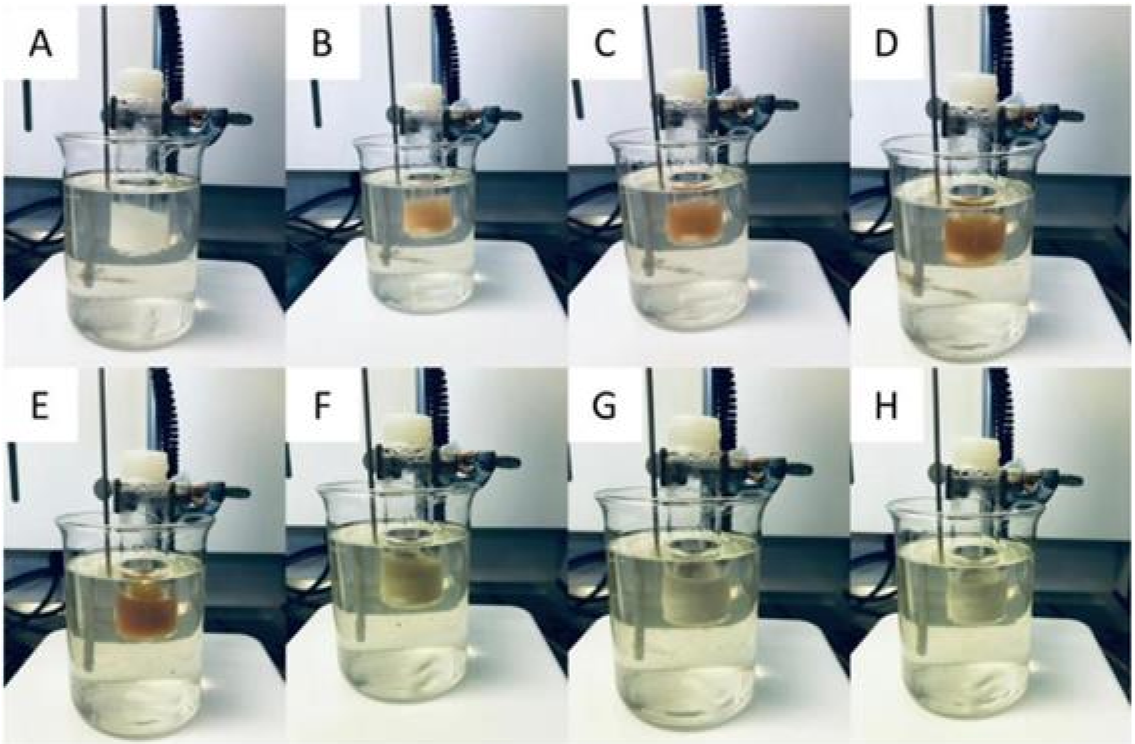

Figure 2.3 Digital photographs of the reaction solution after the first (A), second (B), third (C), fifth (D), sixth (E), seventh (F), eighth (G) and ninth (H) injection of solution B into solution A.

The absorption spectrum of the obtained Ag NWs (Figure 2.4A) shows the two characteristic plasmon peaks of the NWs observed in the TEM image of panel B of Figure 2.4, at 349 nm and 382 nm (Figure 2.4A), attributable respectively to the quadrupole resonance peak and transverse resonance peaks [21], with a weak visible shoulder around 420 nm and other weak shoulders at longer wavelengths attributable to the localized surface plasmon resonance (LSPR) of Ag nanoparticles (NPs) (Figure 2.4C) The mean length and diameter values of the Ag NWs, estimated from the statistics of the size distribution obtained from the TEM images, are 7.7 ± 2.7 μm and 0.07 ± 0.02 nm, respectively.

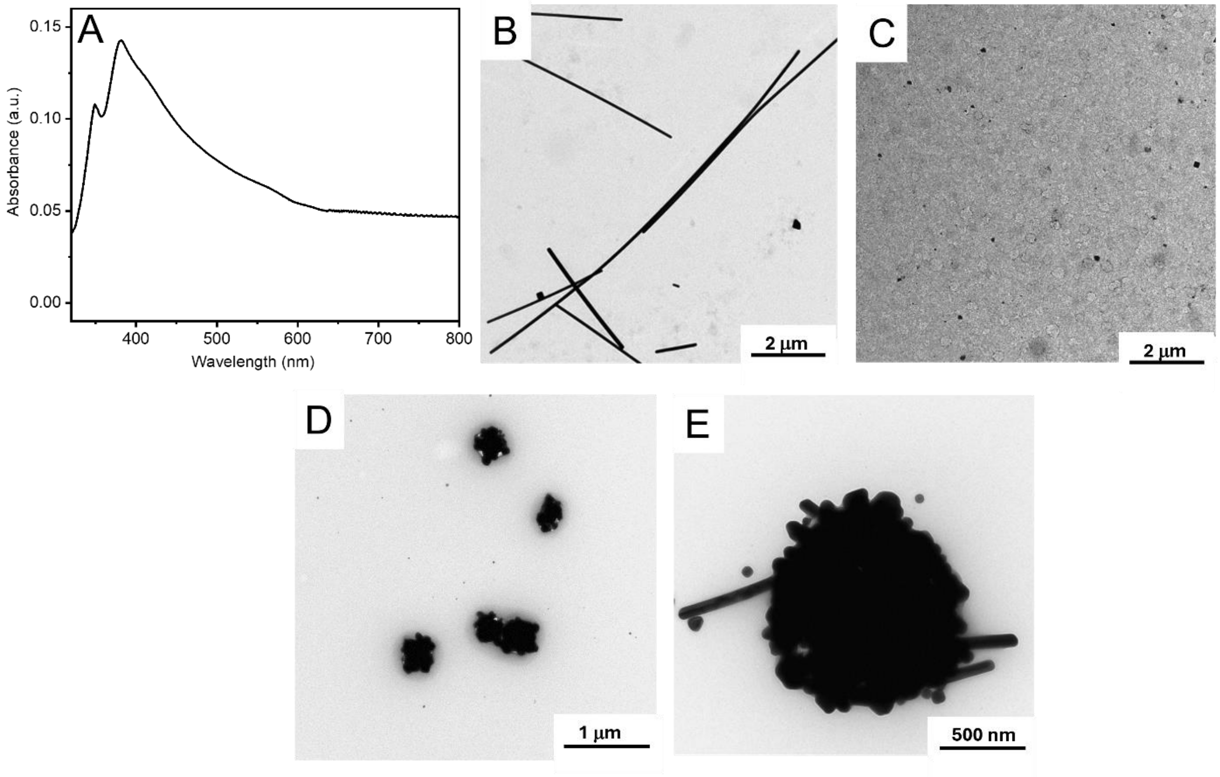

Figure 2.4 (A) UV-Vis absorption spectrum and (B-C) TEM images of the nanostructures, 0.98 mM in ethanol, synthesized at 170°C, reaction time of 2.5 h, with PVP (Mw = 360 kDa), 7.7:1 PVP:$AgNO_3$ molar ratio, stirring rate of 600 rpm and reaction time of 2.5 h. (D-E) TEM micrographs of the nanostructures observed in aliquots of the reaction solution taken after the (D) third and (E) seven injection of $AgNO_3$.

At the third injection of the precursor AgNO3, the formation of cubic nanostructures almost electron transparent, coated by high image contrast nodules was observed (Figure 2.4D). The nanocubes were attributed to silver chloride (AgCl) nanocrystallites, coated by Ag NPs [22], and stabilized by PVP through coordination [23]. The presence of the AgCl nanocubes explains the milky white color of the solution observed at the early stages of the synthesis, and the low solubility of the AgCl nanocubes promotes the gradual and slow release of Ag^+ ions, mimicking the self-seeding process introduced by Xia et al. and consisting of the controlled injection of the Ag+ precursor and PVP by a two-channel syringe pump [24]. The Ag+ ions are then reduced to Ag atom monomers by glycolaldehyde, which is formed by thermal conversion of EG [25], keeping the concentration of the Ag monomers low and allowing the synthesis to proceed under thermodynamic control conditions [23].

The formed Ag atoms gradually heteronucleate onto the surface of the AgCl nanocubes giving the nodules (Figure 2.4D), coloring the solution orange and then brown as the $AgNO_3$ precursor is added.

After the seventh injection, when the concentration of the precursor and the thermal energy are adequate, some of the heteronucleated Ag nodules turn in thermodynamically stable pentagonally twinned prisms which are the seeds initiating the anisotropic growth of the NWs, occurring with formation of filaments from the nodules (Figure 2.4E).

The beginning of the growth of NWs is noted with the color change from brown to grey. This process is driven by the Ostwald ripening phenomenon, where smaller NPs dissolve and provide Ag atoms to larger NPs. Although the pentagonally twinned prisms have the lowest energy structure, they have a face-centered cubic structure, with the {111} planes denser in atoms and in twin boundaries than the {100} facets, that have a higher surface energy [26, 27]. As PVP preferentially adheres on the {100} planes restraining their growth kinetics, it promotes uniaxial elongation of the NWs by fast addition of Ag atoms onto the {111} facets. The thermodynamic control of the synthesis of the NWs is granted by the combination of the slow release of Ag+ ions in solution from the AGCL nanocubes, which keeps low the concentration of Ag atom monomers, and the selective coordination of PVP to the {100} facets of the prisms.

The reducing power of EG increases with temperature [28], and the temperature is also crucial to supply the thermal energy necessary to thermodynamically stabilize the pentagonal-based bipyramidal prisms from which the NWs heteronucleate [29, 30]. In fact, the synthesis of the NWs is never reported in literature at temperatures below 110°C, but between 110°C and 200°C. At 110°C, NWs formation is slow, taking around 12 h, while higher temperatures accelerate the process. In this study, a synthesis temperature of 170°C was chosen, as it provides sufficient thermal energy to produce NWs with high yield [18]. However, raising the temperature above 170°C can lead to an increase in the number of bipyramidal prisms, and NWs grow with a lower aspect ratio due to the limited concentration of Ag^+ ions in the reaction solution [18].

The injection speed of the precursor is another important parameter, as it determines the concentration of Ag+ ions. High injection speeds lead to rapid supersaturation, favoring the nucleation of small Ag clusters rather than bipyramidal prisms. These clusters can dissolve and merge into larger structures through Ostwald ripening [18]. The formation of micrometric structures is observed at considerably low injection rates, as the low concentration of Ag+ ions promote the dissolution of small Ag NPs by Ostwald Ripening which feed large NPs [18].

As the planes at highest surface energy {111} of the pentagonally twinned prisms are susceptible to etching from dissolved O_2 and then dissolution, which were demonstrated to result only in isotropic nanoparticles [30], the synthesis is conducted in a vial sealed with a rubber septum and the precursor solution is injected using a syringe needle that punctures the septum.

In general, the morphology of the nanostructures formed in this process also depends on the molar ratio of PVP:AgNO3, as shown in Figure 2.5. When the ratio is low, the passivation of the faces {100} of the bipyramidal prisms is insufficient and the growth occurs on all faces [18]. In these conditions, NWs with a large diameter are obtained, together with micrometer-sized Ag particles

[31]. For intermediate PVP:$AgNO_3$ molar ratios, the length increases, and the diameter of the NWs decreases gradually (Figure 2.5), while high ratios result in shorter and thicker NWs, along with larger nanostructures due to excessive PVP coordination.

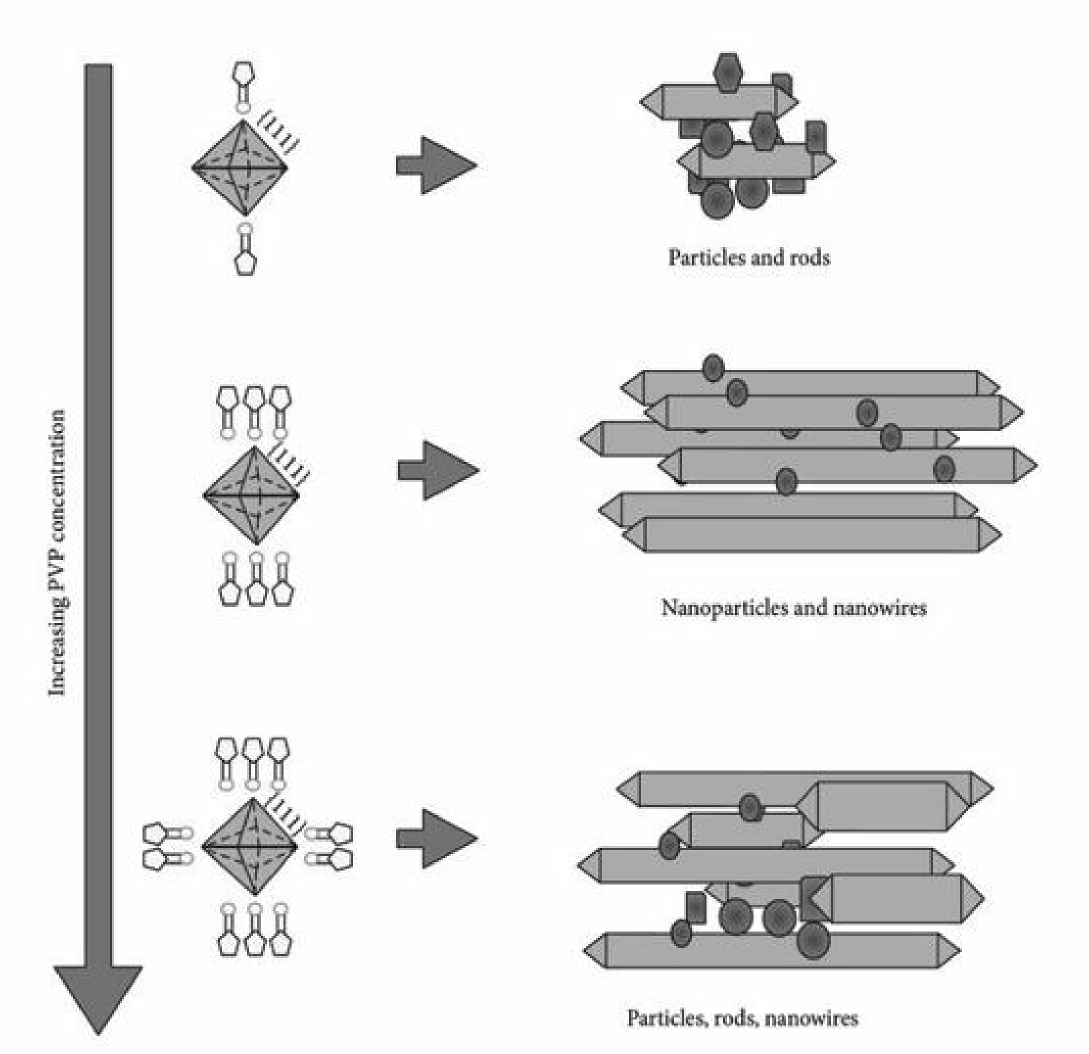

Figure 2.5 Schematic illustration of the effect of increasing PVP concentration on the growth of bipyramidal Ag prisms and on the final morphology of the obtained nanostructures [31].

Finally, also the molecular weight of PVP plays a significant role in modulating the morphology of the nanostructures. Short PVP chains do not effectively coat the growing clusters inducing a less effective steric stabilization, favoring their aggregation. In this case, Ag NPs with irregular morphology and non-uniform dimensions are obtained [32]. Conversely, if the molecular weight of PVP is too high, the adsorption of the polymer chains on the {100} faces become weaker, thus inducing almost isotropic cluster growth [32].

2.5 Synthesis of the hybrid nanocomposite based on the His-RGO complex decorated with Ag NWs (His RGO/Ag NWs)

The hybrid nanocomposite formed of His-RGO decorated with Ag NWs (His-RGO/Ag NWs) was synthesized by modifying the approach reported by S. Coskun et al. [18] with the injection of the His-RGO complex into the NW synthesis solution. To better understand the role of the species involved in the synthesis of the NWs in the presence of the His-RGO complex, some control experiments were conducted. These experiments aimed to elucidate the synthesis mechanism and optimize experimental conditions to produce NWs with relatively high aspect ratios and ensure good coverage of the basal plane of RGO with the NWs.

To study the chemical reactivity of PVP, EG and $AgNO_3$ in presence of the His-RGO scaffold, and their role in the synthesis of the hybrid nanocomposite, three control experiments were conducted. Each experiment followed the same conditions as those for synthesizing the neat Ag NWs, with the modification of the addition of His-RGO to the reaction mixture, which also contained NaCl and $AgNO_3$. In these experiments, His-RGO was used as a powder, that was isolated from a Milli-Q water solution at pH 7 and at the ʒ-*potential* of –20.1±1.5 mV. The specific experimental conditions used in each experiment are summarized in Table 2.1.

Table 2.1: Experimental conditions of the three control experiments, conducted to evaluate the chemical behavior of the single species, $AgNO_3$, PVP and EG, involved in the synthesis of NW, when His RGO is present in the reaction solution.

Control Experiments	**Conditions**
Experiment 1	No PVP, No EG (EG replaced with ODE)
Experiment 2	No PVP
Experiment 3	No EG (EG replaced with ODE)

2.5.1 Control Experiments

In the experiment n.1, a solution (A) was prepared containing 3.5 mg of NaCl and 5 mg of His-RGO in 5 ml of ODE, heated at 170°C in a vial closed with a rubber septum, immersed in an oil bath under stirring at 600 rpm, to which a solution (B) was added, that was prepared by dissolving 50 mg of $AgNO_3$ in 2.5 ml of ODE. The injection of solution (B) into (A) was performed with a 1 ml syringe, injecting 0.25 ml every 6 min. At the end of the injection, the vial was left under stirring at 170°C for 90 min.

The UV-Vis absorption spectrum of the synthesized hybrid nanostructures achieved in experiment n. 1 shows a peak at 275 nm (Figure 2.6A), which can be attributed to the π-π^* transition of the -C=C- bond of RGO. Additionally, a broad absorption band at wavelengths greater than 318 nm can be observed which is likely due to the plasmon resonance of polydisperse Ag nanostructures (Figure 2.6A). As a support of this observation, the TEM micrographs of the sample show the almost electron transparent sheet-like nanostructures of the His-RGO sheets, which are characterized by the typical wrinkles and folded edges ascribed to mechanical deformations of the RGO basal plane, coated with high-contrasts, multifaceted nanoparticles (NPs), having a size in between 100 - 300 nm (Figure 2.6B). These nanoparticles are reasonably attributed to Ag NPs that heteronucleate and grow *in situ* onto the His-RGO sheets via the galvanic reduction of the $AgNO_3$ precursor. This process occurs through electron transfer from His-RGO to Ag(I) ions, highlighting the role of His in facilitating electron transfer between RGO and Ag. This mechanism underscores the importance of His-RGO complex in the formation of the His-RGO/Ag NP hybrid nanostructures.

In the second experiment (n. 2), the chemical reactivity of EG in the presence of AgNO3, His-RGO and NaCl, without PVP, was studied. For this purpose, a solution (B), which was prepared by dissolving 50 mg of AgNO3 in 2.5 ml of EG, was added to a solution (A) containing 3.5 mg of NaCl and 5 mg of His-RGO in 5 ml of EG, which was prepared in a vial closed with a rubber septum, immersed in an oil bath heated up to 170°C, and under stirring at 600 rpm. Also, in this case solution (B) was added to (A) in 0.25 ml injections conducted every 6 min, and at the end of the injections, the vial was left to stir at the same temperature for 90 min.

The absorption spectrum of the sample achieved in experiment n. 2 shows the peak of His-RGO at 281 nm (Figure 2.6A), which is shifted approximately 6 nm towards the higher wavelengths with respect to the same peak of the sample synthesized in the first control experiment. The shift is likely due to the presence of EG, that reduces GO domains residual onto the RGO basal plane [33]. In this sample, the absorption plasmon resonance peak of Ag nanostructures is not detectable (Figure 2.6A). Instead, high-contrast, micrometer-sized structures, attributed to Ag, are predominantly observed on the His-RGO sheets. These structures likely result from a combination of the rapid reduction of $AgNO_3$ [34] by EG and by the electron transfer from His-RGO to the Ag precursor (Figure 2.6C). Further TEM analysis of the same sample reveals the presence of nearly optically transparent nanocubes (Figure 2.6D) with high-contrast, nodule-like structures heteronucleated on some of them (Figure 2.6E). Morphologically, these features are similar to the AgCl nanocubes coated with Ag nanoparticles (NPs) observed at the early stages of the seed-mediated polyol synthesis of net Ag NWs (Figure 2.4D). These nodules originate from the reduction of Ag(I) ions to Ag(0) atom monomers by glycolaldehyde, which generates dispersion through the thermal oxidation of EG [25], and diffuse, heteronucleating at the nanocubes surface (Figure 2.6E), aided by the steric stabilization of PVP and electrostatic repulsion for chemisorption of Cl^- ions. These results highlight that also in the synthesis of the hybrid nanocomposite, in the experimental conditions investigated, EG behaves as a reducing agent.

Finally, the reactivity of PVP without EG, was studied in presence of $AgNO_3$, His-RGO and NaCl, in experiment n. 3. Specifically, ten aliquots of 0.25 mL of a 20 mg mL^{-1} $AgNO_3$ solution in ethanol were injected every 6 min, in a dispersion, which was prepared by dissolving 3.5 mg of NaCl, 5 mg of His-RGO and 250 mg of PVP, in 5 ml of ODE, heated up to 170°C under stirring at 600 rpm. The sample obtained under these experimental conditions shows the absorption peak of His-RGO at 273 nm and a broadband, at wavelengths longer than 321 nm, attributable to the peak of polydisperse Ag nanostructures (Figure 2.6A), which, in the TEM images are heteronucleated, and in part also coalesced, on the His-RGO sheets, showing a multifaceted morphology, with a dimension of approx. 200 nm, smaller than that of the structures achieved by reaction of $AgNO_3$ with His-RGO (Figure 2.6B).

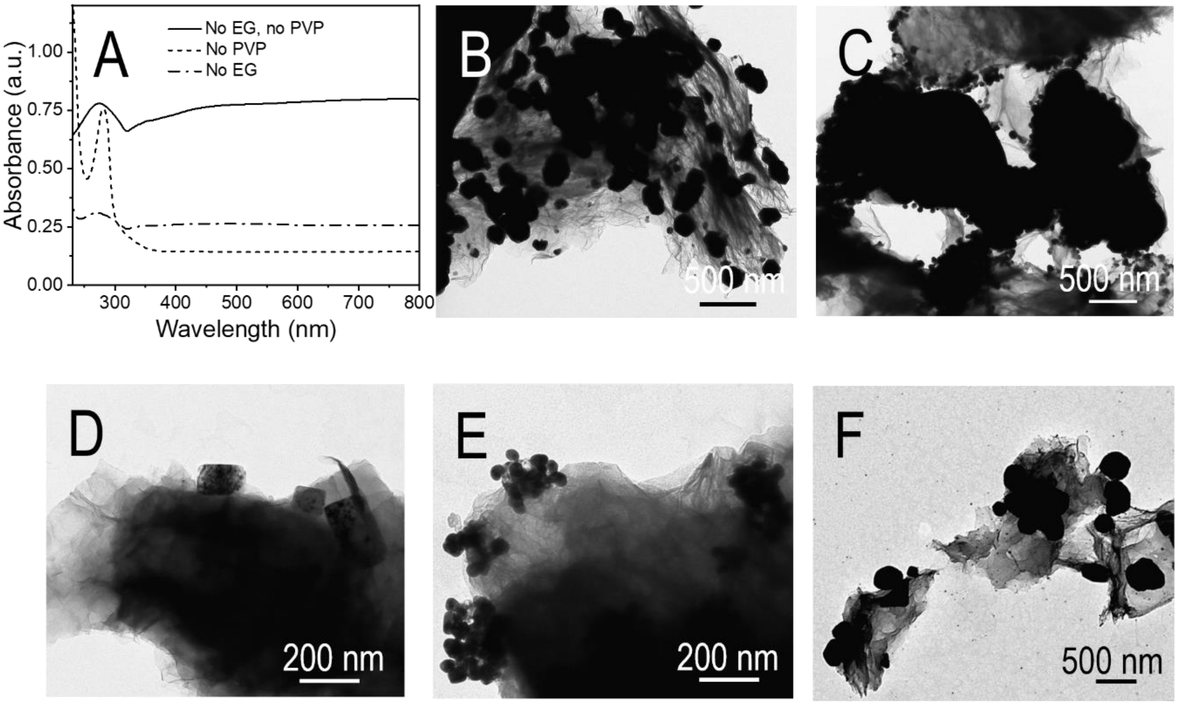

Figure 2.6 (A) UV-Vis absorption spectrum of hybrid nanostructures synthesized at 170°C, at the reaction time of 2.5 h, stirring rate of 600 rpm, with the 10:1 AgNO3:His-RGO w/w, from an ethanol dispersion 0.654 mM in AgNO3 and 1 mg mL-1 in His-RGO. (B) TEM images of the hybrid nanostructures synthesized without EG and PVP, (C-E) with EG and without PVP, and (F) with PVP (Mw=360 kDa) at the 7.7:1 PVP:AgNO3 molar ratio, without EG.

Based on these preliminary control experiments, it was observed that, when both His-RGO and NaCl are present, Ag^+ ions react with Cl^- ions to produce AgCl nanocubes. These nanocubes seem to be attached to the His-RGO basal plane, likely due to interactions with the carboxylic and amino groups on the His-RGO surface, as they were observed only onto the His-RGO sheets (Figure 2.6 D-E) and not in the supernatant of the synthesis solution, an observation that, to the best of our knowledge, has not been previously reported in literature. This is a key observation, because, during the synthesis of neat Ag NWs, the NWs' anisotropic growth initiates from these nodule-like structures when PVP [23] is present in solution and behaves as a unidirectional growth directing agent. This suggests a similar growth mechanism could occur on the His-RGO surface, potentially allowing for the synthesis of Ag NWs in a controlled manner.

To establish a reliable protocol of the synthesis of the His-RGO/Ag NWs hybrid nanocomposite formed of His-RGO sheets decorated with monodisperse Ag NWs, and processable from solution for applications, the effects of the experimental synthesis parameters expected to affect its morphology and spectroscopy properties, namely reaction time, PVP molecular weight, PVP:AgNO3 molar ratio, His-RGO complex injection mode into the synthesis solution and its dissociation state, the AgNO3:His-RGO weight ratio (w/w) and stirring rate, were systematically examined. The properties of these nanocomposites were also compared with those of the neat Ag NWs produced under the same experimental conditions (Figure 3.4B).

2.5.2 Injection mode of the His-RGO complex in the synthesis solution.

A series of experiments was conducted to determine the optimal injection mode for introducing His-RGO into the Ag NWs synthesis solution. Also in these experiments, the used His-RGO complex was isolated as a powder, by centrifugation, from a Milli-Q water solution at pH 7 and Ʒ-*potential* of –20.1±1.5 mV.

In detail, the first experiment was carried out by injecting a solution (B), which was prepared by dissolving 50 mg of $AgNO_3$ in 2.5 ml of EG, in a solution (A), containing 250 mg of PVP (Mw = 360 kDa), 3.5 mg of NaCl and 5 mg of His-RGO in 5 ml of EG, heated up to 170°C in a vial closed with a rubber septum, immersed in an oil bath, and placed under stirring at 600 rpm. Solution (B) was added to (A) by injections of 0.25 ml, carried out every 6 min, with a 1 mL syringe. At the end of the injections, the vial was left under stirring at 600 rpm, 170°C, for 90 min.

During the injections of $AgNO_3$, the dispersion undergoes a series of distinct color changes. Initially, at the first injection, the dispersion transitioned from black to light grey, indicative of the formation of AgCl, which is a milky white color. Between the second and sixth injections, the dispersion developed an orange color that gradually becomes darker, likely due to the formation of Ag nanostructures. After the seventh injection, the dispersion becomes dark silver, as expected for the formation of the Ag NWs in presence of His-RGO.

The UV-Vis absorption spectrum of the synthesized hybrid nanostructures shows a notable absorption peak at 275 nm corresponding to RGO, as well as a large surface plasmon resonance absorption band for wavelengths extending beyond 315 nm, with superimposed peaks at 340 and 410 nm (Figure 2.7A). These spectral features are indicative of the successful formation of hybrid His-RGO/Ag NW nanostructures, with the observed peaks suggesting the presence of both RGO and elongated and spherical Ag nanostructures.

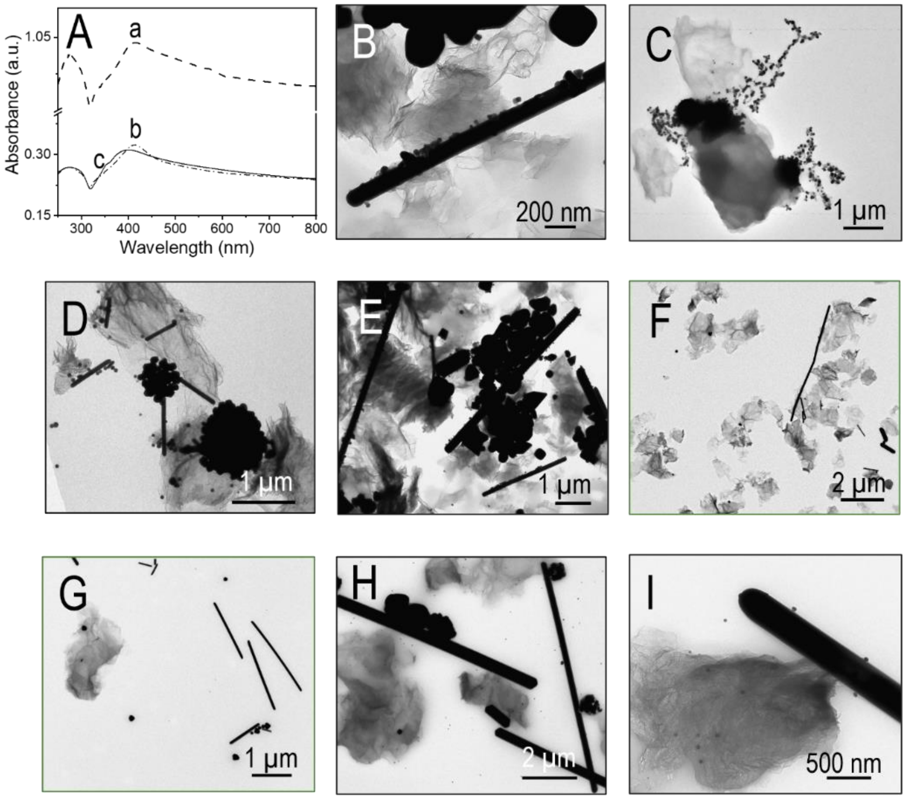

Figure 2.7 (A) UV-Vis absorption spectra and (B-I) TEM images of hybrid nanostructures synthesized with the 10:1 $AgNO_3$:His-RGO w/w, 7.7:1 PVP:$AgNO_3$ molar ratio, at 170°C, reaction time of 2.5 h, PVP at Mw of 360 kDa, stirring rate of 600 rpm, by injecting His-RGO (a, B-E) in the synthesis solution containing PVP and NaCl, then slowly added by $AgNO_3$, (b, F-G) after complete injection of $AgNO_3$, and (c, H-I) between the seventh and eight injection of $AgNO_3$. In (A) AgNO3 and His-RGO were 0.654 mM and 1 mg mL^{-1} in ethanol, respectively.

The TEM images of the synthesized sample, in fact, exhibit elongated nano-objects that are surrounded by His-RGO sheets and display an image contrast like that of neat Ag NWs, suggesting that they are likely Ag NWs wrapped by His-RGO sheets (Figure 2.7B). The TEM micrographs also show Ag clusters stabilized by PVP, around nodules that are anchored on the His-RGO sheets (Figure 2.7C). Moreover, the images reveal the presence of filaments extending from some nodules anchored onto the His-RGO sheets (Figure 2.7D). This observation is particularly noteworthy because, to the best of our knowledge, such protruding filaments have not been reported in literature before, assessing initiation of the NWs growth form the AgCl nanocubes anchored onto the sheets. Interestingly, unlike the typical synthesis of pure Ag NWs reported in literature, more than one filament was observed emanating from individual nodules on the His-RGO sheets. The mean values of length and diameter of the Ag NWs in the nanocomposite are 4 ± 2 μm and 0.17 ± 0.07 μm, respectively, against 7.7 ± 2.7 μm and 0.07 ± 0.02 μm, the mean values of length and diameter estimated for the sample of neat NWs.

The TEM images of Figure 2.7 D-E indicate the formation of other structures in the nanocomposite, including spherical NPs, nanosized cubic byproducts, and irregularly shaped particles at the micrometer scale. These various morphologies contribute to the overall complexity of the composite material. The TEM micrographs of Figure 2.7 panels B-E allow to assign the surface plasmon resonance absorption peak of the sample, at 340 nm (Figure 2.7A), to the quadrupole resonance of the Ag NWs in the nanocomposite, which is at 349 nm in the spectrum of the neat Ag NWs (Figure 2.4A), and the peak at 410 nm, is attributed to the transverse plasmon resonance. This peak is shifted to longer wavelengths compared to that of the pure Ag NWs, which appears at 381 nm. This shift is likely caused by the increased diameter of the NWs, from 0.07 ± 0.02 μm in the pure Ag NWs to 0.17 ± 0.07 μm in the nanocomposite, consistent with the known relationship between the wavelength of the transverse plasmon absorption peak and the NW diameter (D), described by the equation $\lambda = 361.3 + 0.410\ D_{NW}$ [35]

The broadening of the localized surface plasmon resonance band in the absorption spectrum of the His-RGO/Ag NWs (Figure 2.7A), extending from the visible to the near infrared wavelengths, is due to the absorption of spherical NPs and to light trapping effects. These last effects are induced by hotspots that form at the junctions where the Ag NWs overlap [36]. Finally, the increase in the baseline signal of the absorption spectrum may be due to scattering phenomena originating from the micrometer-sized particles and the presence of His-RGO multilayers.

To avoid the formation of nanosized cubic byproducts and micrometer-sized particles, the His-RGO complex was strategically added to the synthesis solution after the completion of tenth injections of $AgNO_3$. The aim was to allow the nucleation of Ag NWs first, and then the intercalation of the His-RGO sheets between the PVP chains coordinated at the NWs surfaces. By doing so, His-RGO was expected to anchor to the NW surfaces during the dynamic adsorption and desorption of PVP on the growing NWs. For this experiment, His-RGO was isolated as a powder by centrifugation from a Milli-Q water solution at pH 7 and Ʒ-*potential* of –20.1±1.5 mV, dispersed in EG, and was heated up to 170°C before being injected into the synthesis solution, to ensure that the temperature remained constant.

The absorption spectrum of the hybrid nanostructures achieved in these experimental conditions showed a distinct absorption peak of RGO at 275 nm, a shoulder at 355 nm, corresponding to the quadrupole resonance of the Ag NWs, and the transverse plasmon resonance of the NWs at 400 nm (Figure 2.7A). The TEM images of the achieved sample show NWs with an average length of approximately 5 ± 3 µm and a diameter of 0.11 ± 0.06 µm, accompanied by spherical Ag NPs (Figure 2.7 F-G). However, the TEM images predominantly displayed bare His-RGO sheets and homonucleated Ag NWs (Figure 2.7 F-G). This finding indicates that His-RGO did not effectively coordinate to the NW surfaces, likely due to the steric hindrance caused by the His-RGO flakes, which prevented adequate surface coverage and interaction with the NWs surface.

In view of the unsatisfactory results of these two preliminary experiments, another approach was adopted. His-RGO was added to the synthesis solution immediately after the nucleation of Ag NWs, which was indicated by a color change from dark orange to light grey, occurring after the seven injections of $AgNO_3$ to the reaction solution. Prior to the addition of His-RGO, its dispersion in EG was preheated up to 170°C to maintain the reaction temperature constant.

The TEM analysis of the hybrid nanostructures synthesized under these modified conditions showed NWs with an average length and diameter of 6 ± 5 µm and 0.27 ± 0.10 µm, respectively, which were anchored by His-RGO sheets (Figure 2.7H). Additionally, spherical NPs with an average size of around 39 ± 12 nm were observed adsorbed on the surfaces of the Ag NWs (Figure 2.7I). Nodule-like nanostructures were also present (Figure 2.7H), along with homonucleated Ag NWs (data not shown). The absorption spectrum of the sample shows the absorption peak of His-RGO a 275 nm, the shoulder of the quadrupolar resonance of the NWs at 330 nm and the peak at 413 nm, due to the transverse plasmon peak of the NWs (Figure 2.7A).

The lack of nanosized Ag cubes and micrometer-sized byproducts, coupled with the predominance of NWs wrapped by His-RGO in the nanocomposite (Figure 2.7 H-I), indicated that this revised injection method was effective. This approach was subsequently adopted for further studies involving the change of other experimental parameters to optimize the synthesis of the His-RGO/Ag NW nanocomposites. Moreover, the presence of nodule-like structures and small Ag NPs in the nanocomposite (Figure 2.7 H-I) lead us to infer that prolonging the synthesis reaction time could potentially initiate and complete the conversion of these nodules into fully developed NWs. This extension of the reaction time aims to enhance the growth and uniformity of the Ag NWs while minimizing the formation of undesirable byproducts.

2.5.3 Effect of reaction time, dissociation state of His-RGO, PVP molecular weight and PVP:$AgNO_3$ molar ratio

In the next set of experiments, the reaction time was extended to 5 h and then to 6.5 h, while other synthesis parameters were kept constant. Namely, the reaction temperature, the stirring rate, the PVP Mw, the PVP:$AgNO_3$ molar ratio and the $AgNO_3$:His-RGO w/w were fixed at 170°C, 600 rpm, 360 kDa, 7.7:1 and the 10:1, respectively. His-RGO was injected between the seventh and the eight injection of $AgNO_3$, from a dispersion in EG preheated up to 170°C.

The UV-Vis absorption spectrum of the hybrid nanocomposite synthesized at the reaction time of 5 h shows the peak of RGO at 275 nm. Also, a broad surface plasmon resonance band was observed for wavelengths greater than 319 nm, which was more intense than that seen in the sample synthesized after 2.5 h. Two shoulders at 354 nm and 392 nm, that are respectively ascribed to the quadrupole and the transverse plasmon resonances of the NWs (Figure 2.8A) were notices. The rise in the baseline signal intensity also suggested a higher concentration of nanostructures.

Further examination revealed that the transverse plasmon resonance peak of the sample achieved after 5 h is shifted towards the higher energy side of the spectrum with respect to the peak observed after 2.5 h of synthesis (Figure 2.8A), namely it passes from 413 nm to 392 nm, indicating a decrease in the NWs diameter. TEM images confirmed this observation, showing shorter NWs with a mean length of 5 ± 3 µm and a reduced diameter of 0.10 ± 0.03 µm, which were anchored onto and wrapped by His-RGO sheets, as well as spherical Ag NPs of mean size of 143 ± 72 nm (Figure 2.8 C-D) larger than the Ag NPs in the nanocomposite grown for 2.5 h (Figure 2.8B).

Given that the absorbance intensity of the two plasmon bands of the NWs is independent of their morphology and considering that the size of the spherical NPs increased from 39±12 nm after 2.5 h, to 143 ± 72 nm after 5 h, the increase of the absorption intensity of the sample grown for 5 h lead us to infer an increase of the NWs concentration. This increase is likely due to the reaction of unreacted $AgNO_3$ precursor left after 2.5 h and the dissolution of smaller spherical NPs via Ostwald ripening, which supplies Ag atoms to the nodules, promoting further NWs growth [25] and enlarging the existing larger Ag NPs.

Despite the prolonged reaction time of 5 h, however, TEM images still showed nodule-like structures with protruding filaments on the His-RGO platform (Figure 2.8D). This observation led us to increase further the time of the reaction up to 6.5 h, aiming to complete the conversion of these nodules into filaments, thereby potentially increasing the NWs concentration.

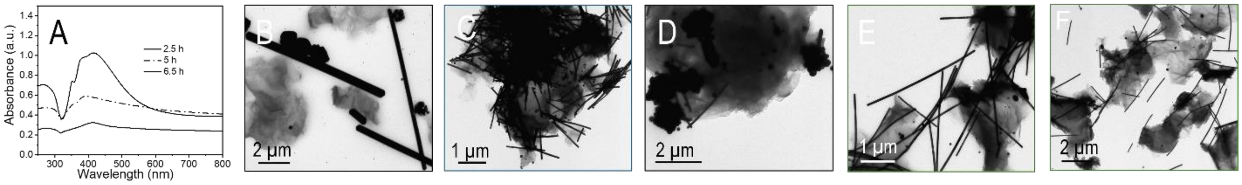

Figure 2.8 (A) UV-Vis absorption spectra and (B-F) TEM images of the hybrid nanocomposites synthesized with the 10:1 $AgNO_3$:His-RGO w/w, 7.7:1 PVP:$AgNO_3$ molar ratio, at 170°C, PVP at Mw of 360 kDa, stirring rate of 600 rpm, and reaction time of (B) 2.5 h, (C-D) 5 h and (E-F) 6.5 h, achieved injecting His-RGO between the seventh and the eight injection of $AgNO_3$. In (A) $AgNO_3$ and His-RGO were 0.654 mM and 1 mg mL^{-1} in ethanol.

After 6.5 h of reaction, the absorption spectrum of the His-RGO/Ag NWs nanocomposite exhibited an enhanced broad surface plasmon resonance band for wavelengths above 319 nm, with superimposed both the quadrupole and the transverse resonance plasmon peak appearing at 352 nm and 378 nm, respectively, indicating a further increase in NW concentration. The LSPR peak of spherical Ag NPs showed at 415 nm.

The TEM analysis of this sample shows spherical NPs, 76 ± 44 nm in mean size and the lack of nodules (Figure 2.8 E-F), demonstrating their complete evolution in NWs. In addition, the morphology investigation shows NWs with higher monodispersion, and with mean length and diameter decreased down to 2.5 ± 1.0 µm and 0.05 ± 0.01 µm, respectively.

It is important to note that the observed reduction in NW length and diameter is not due to etching caused by the production of nitric acid (HNO_3) during the reduction of Ag+ ions to Ag atoms by glutaraldehyde [37]. This is because Cl^- ions , which absorb on the {100} facets of the growing NWs, offer protection. Moreover, the pH of the solution only slightly decreases, passing from 5.5, the pH of the injected His-RGO dispersion in EG, to 4.9 after 5 h of reaction, and to 4.7 after 6.5 h.

In all the previous experiments, the His-RGO dispersion in EG was prepared by isolating His-RGO from a Milli-Q water solution at pH 7. This condition was selected, because His-RGO isolated from a water solution at pH 11, with a ʒ - *potential* of –24.5 ± 1.8 mV, resulted in a higher dissociation state, and in a more competition of its carboxylate and amino functionalities with PVP in coordinating and stabilizing the surface of the growing clusters, preventing their anisotropic growth into NWs. Indeed, TEM images of the hybrid nanostructures achieved under these conditions showed short, elongated nanostructures, 0.6±0.4 µm in mean length and 0.1±0.1 µm in mean diameter, along with spherical and micrometer sized particles.

Besides, the chosen Mw of PVP of 360 kDa, and the PVP:$AgNO_3$ molar ratio of 7.7:1, were proven to be the most appropriate to control the anisotropic growth of the Ag NWs in the His-RGO/Ag NWs nanocomposite. When the synthesis of the hybrid nanocomposite was conducted with the PVP at the lower M_w of 55 kDa, which has been reported in literature suited to synthesize monodisperse neat Ag NWs, the achieved hybrid nanostructures showed mainly the formation of spherical Ag NPs up to hundreds nm of size, with NWs of mean length of 2.6±0.6 µm and diameter of 0.09±0.04 µm, along with aggregated micrometer sized Ag structures (Figure 2.9B). Additionally, aggregated micrometer-sized Ag structures were observed (Figure 3.9C). Moreover, when using PVP with a Mw of 360 kDa and increasing the PVP:AgNO3 molar ratio up to 11.5:1, the hybrid nanostructures primarily consisted of spherical Ag NPs with a few NWs of 0.9 ± 0.6 µm in length and 0.05 ± 0.01 µm in diameter.

These findings demonstrate that the steric hindrance posed by the His-RGO complex renders lower molecular weight PVP ineffective in promoting and controlling NW growth. While, when using

PVP with Mw of 360 kDa, the increase of the PVP:AgNO3 molar ratio tends to produce shorter NWs with a high concentration of spherical Ag NPs (Figure 2.9D), likely because of the tendency of PVP to coordinate all facets of the seeds in growth [32].

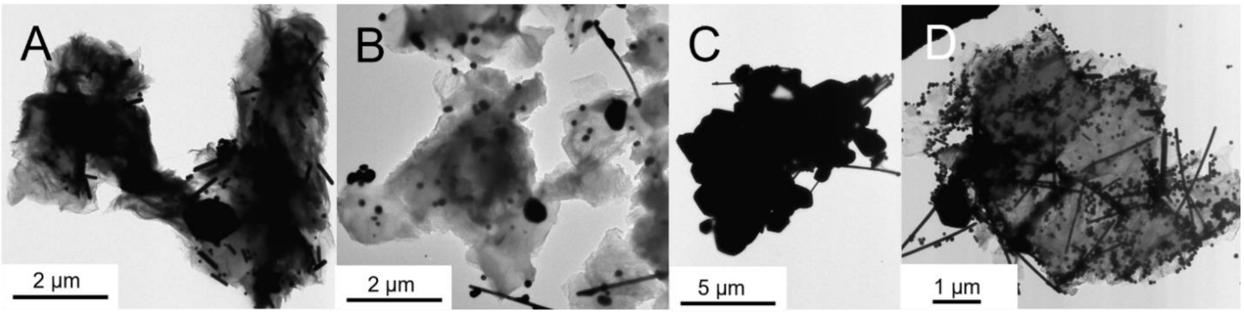

Figure 2.9 TEM images of His-RGO/Ag NWs synthesized with the 10:1 $AgNO_3$:His-RGO w/w, at 170°C, stirring rate of 600 rpm, time of reaction 6.5 h, injecting His-RGO between the seventh and the eight injection of $AgNO_3$, by using (A) His-RGO isolated from a Milli-Q water solution at pH 11 and ʒ-*potential* of –24.5±1.8 mV, with 7.7:1 PVP:$AgNO_3$ molar ratio and PVP 360 kDa, and (B-D) His-RGO isolated from a Milli-Q water solution at pH 7 and ʒ-*potential* of -20.1±1.5 mV, with (B-C) 7.7:1 PVP:$AgNO_3$ molar ratio and PVP 55 kDa, and (D) 11.5:1 PVP:$AgNO_3$ molar ratio with PVP 360 kDa.

Increasing the $AgNO_3$:His-RGO w/w up to 5:1, the hybrid nanostructures show a LSPR band lower in intensity than that of the 10:1 w/w counterpart (Figure 2.8A), an increase of the baseline of the LSPR band of the Ag NWs originated from scattering phenomena from multilayers of His-RGO, with the transversal plasmon peak not clearly detectable, because likely superimposed by the LSPR of spherical Ag NPs (Figure 2.9A). The nanocomposite show Ag NWs with mean length and diameter comparable with those of the 10:1 w/w nanocomposite (Figure 2.8 E-F), but a higher concentration of spherical Ag NPs and of Ag nodules were observed (Figure 2.9B), assessing the slowing-down of the NWs' growth due to the increase of the His-RGO sheets concentration, and hence, the need for increasing the reaction time up to 7.5 h to complete the conversion of the nodules in NWs, resulting in a mean length and diameter of 1.74 ± 0.89 µm and 0.06 ± 0.01 µm, respectively (Figure 2.9C).

Finally, decreasing the stirring rate from 600 rpm down to 200 rpm, a hybrid nanocomposite with a LSPR band lower in intensity (Figure 2.8A), a shift of the quadrupolar plasmon resonance and transversal plasmon peaks towards the lower energy side (Figure 2.8A) were observed (Figure 2.9 D-F). NWs having higher mean length and diameter, as well as spherical Ag NPs and nodules, formed (Figure 2.9E), indicating, the latter, the uncomplete growth of the NWs due to the lower diffusion rate and, accordingly an inhomogeneous concentration of Ag+ ions in the reaction solution, locally favouring the reaction of Ag atoms with the Ag multitwin seeds and growing NWs clusters, thus leading to longer and larger NWs, that, however, leaves unreacted nodules in the reaction mixture (Figure 2.9F). Prolonging the reaction time up to 7.5 h when the lower stirring rate, the complete evolution of the nodules into NWs was observed, leading to Ag NWs of mean length and diameter of 2.11 ± 0.52 µm and 0.04 ± 0.006 µm (Figure 2.9F).

2.6 Raman and ATR-FTIR spectroscopy investigation of the His-RGO/Ag NWs nanocomposite

The structural and surface chemistry properties of the His-RGO/Ag NWs nanocomposite were thoroughly investigated by Raman and attenuated total reflectance Fourier-transform infrared ATR-FTIR spectroscopy.

The Raman spectrum of RGO is characterized by two prominent peaks, the D and G peaks at ca. 1349 cm^{-1} and 1582 cm^{-1}, respectively, that are the typical modes of graphitic materials. The former peak derives from a second order Raman process involving the inelastic and elastic scattering of an electron with a phonon and a defect respectively. This peak is the indication of defects in the carbon lattice of RGO, that is also indicated by the very low intensity of the 2D peak at ca. 2700 cm^{-1}, and the presence of the D+D' peak below 3000 cm^{-1}. The G peak, on the other hand, is associated with the stretching of sp^2 carbon-carbon bonds and the breathing modes of sp^2 carbon atoms within hexagonal rings, which is typical of graphitic materials.

Raman spectra show that after decoration of His-RGO with the Ag NWs, the position of the D and G peaks of His-RGO does not change, but the intensity of the D peak decreases with respect to the intensity of the G peak (Figure 2.10A), attesting occurrence of graphitization of the residual GO domains in the RGO basal plane, that is induced by reduction with EG at the reaction temperature investigated in the synthesis [33].

The ATR-FTIR spectrum of the His-RGO/Ag NWs nanocomposite shows the stretching vibration of -OH ($\upsilon_{\text{-OH}}$) moieties at 3322 cm^{-1}, which is also detectable in the spectrum of PVP at 3400 cm^{-1}, and that is ascribed to the cheto-enol equilibrium of C=O group in the pyrrolidine ring (Figure 2.10B) [32]. In the spectrum of the hybrid nanocomposite are also detectable the symmetric and asymmetric stretching modes of -CH$_2$ ($\upsilon_{\text{s,asCH2}}$) at 2861 cm^{-1} and 2945 cm^{-1}, respectively that in the spectrum of PVP are located at 2882 cm^{-1} and 2969 cm^{-1}, and, in the spectrum of His-RGO, are instead at 2889 cm^{-1} and 2981 cm^{-1} (Figure 2.10B). These results confirm the presence of PVP in the hybrid nanocomposite sample.

Going more into detail, the infrared spectrum of the nanocomposite shows a peak at ca. 1643 cm^{-1} accountable to the stretching of the C=O group ($\upsilon_{\text{C=O}}$) of PVP, the bending of CH groups (δ_{CH}) at 1367 cm^{-1} and the wagging C-N ($\upsilon_{\text{C-N}}$) at 1280 cm^{-1}, that, in the spectrum of neat PVP, are at 1652 cm^{-1}, 1373 cm^{-1} and 1289 cm^{-1}, respectively (Figure 2.10B). In particular, the shift of the C=O group towards the lower wavenumbers provides evidence of the coordination of PVP at the (100) facets of the Ag NWs, while those of the stretching modes of -CH$_2$ ($\upsilon_{\text{s,asCH2}}$), bending of CH ($\delta_{\text{CH}}$)

and wagging of C-N ($\upsilon_{C\text{-}N}$) towards lower wavenumbers (Figure 2.10B) demonstrate that these groups are closer to the Ag NWs surface [32].

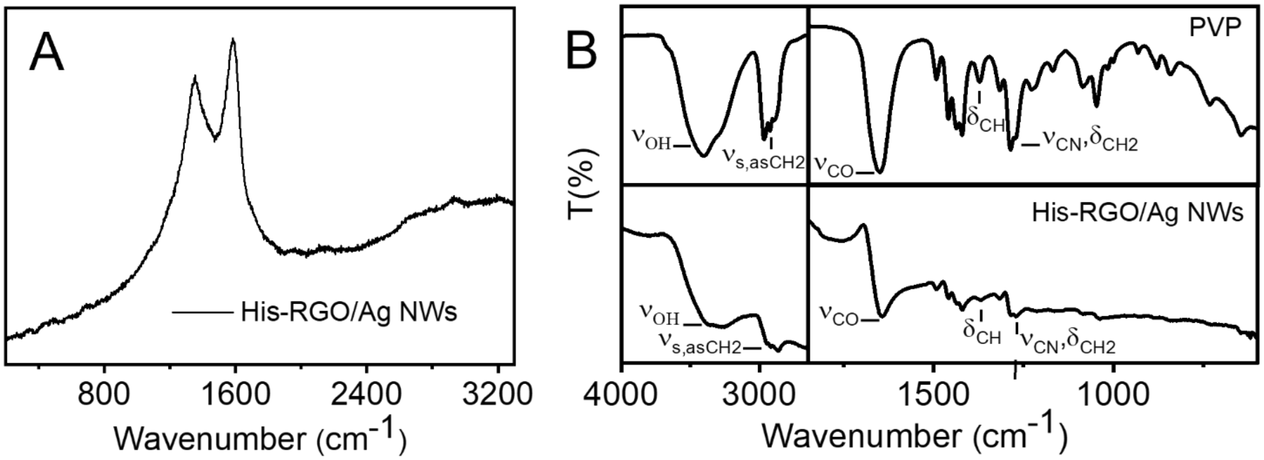

Figure 2.10 (A) Raman spectra of His-RGO/Ag NWs. (B) ATR-FTIR spectra of PVP (Mw= 360 KDa) and of His-RGO/Ag NWs.

2.7 Reaction mechanism of His-RGO/Ag NWs

The formation mechanism of His-RGO/Ag NWs was examined by monitoring synthesis progress through the withdrawal of aliquots of the synthesis solution after each $AgNO_3$ precursor injection, both before and after the addition of His-RGO. The spectroscopy and morphological properties of the resulting nanostructures in each aliquot were assessed after purification and isolation via centrifugation in acetone and subsequent re-dispersion in ethanol.

After the first injection of $AgNO_3$ into the solution of PVP and NaCl in EG, the reaction mixture turns milky white, indicating the formation of AgCl nanocubes [18] (Figure 2.3A), and after the second injection, it transitions to a light orange color (Figure 2.3B), progressively darkening with subsequent injections up to the sixth (Figure 2.3 B-E). UV-Vis absorption spectra of the second and fourth aliquots show a broad plasmon peak spanning the visible spectral range (Figure 2.11A traces b-c), indicating the presence of polydisperse Ag nanostructures. TEM images of these aliquots reveal nodules consisting mostly of nanocubes coated with Ag NPs, along with a few spherical Ag NPs (~19 nm). The following aliquots continue to show nodules and spherical Ag NPs, with their concentration increasing through the fifth injection.

The UV-Vis absorption spectra of the second and fourth aliquots exhibit a prominent plasmon peak spanning the entire visible spectrum, as depicted in traces b-c of Figure 2.11A. This phenomenon persists even after the fifth injection and is likely attributable to the plasmon absorption of polydisperse Ag nanostructures. TEM images reveal that the nanostructures in the second, fourth, and sixth aliquots primarily comprise nodules composed of bright nanocubes coated with Ag NPs exhibiting high image contrast, heteronucleated at their surface (trace b of Figure 2.11B), alongside few spherical Ag NPs of approximately 19 nm (data not shown). Subsequent aliquots (trace c of Figure 2.11B for the fourth, and data not shown for the fifth) also feature nodules, along with Ag NPs still around 19 nm in size, whose concentration appears to increase from the second to the fifth addition of the $AgNO_3$ precursor (data not shown).

Following the sixth injection of $AgNO_3$, the solution turns dark orange (Figure 2.3E), and the originally broad plasmon absorption band get narrower and shift towards higher energy, centering around 400 nm (trace d, Figure 2.11A), indicating primarily the formation of spherical Ag NPs (trace d, Figure 2.11B), as confirmed by the TEM image that shows Ag NPs approximately 7 nm in size, along with nodules (trace d, Figure 2.11B). The absorption peak observed in the spectra of the second, fourth, and sixth aliquots at 270 nm is attributed to the absorption of the PVP:Ag+ complex (Figure 2.11A).

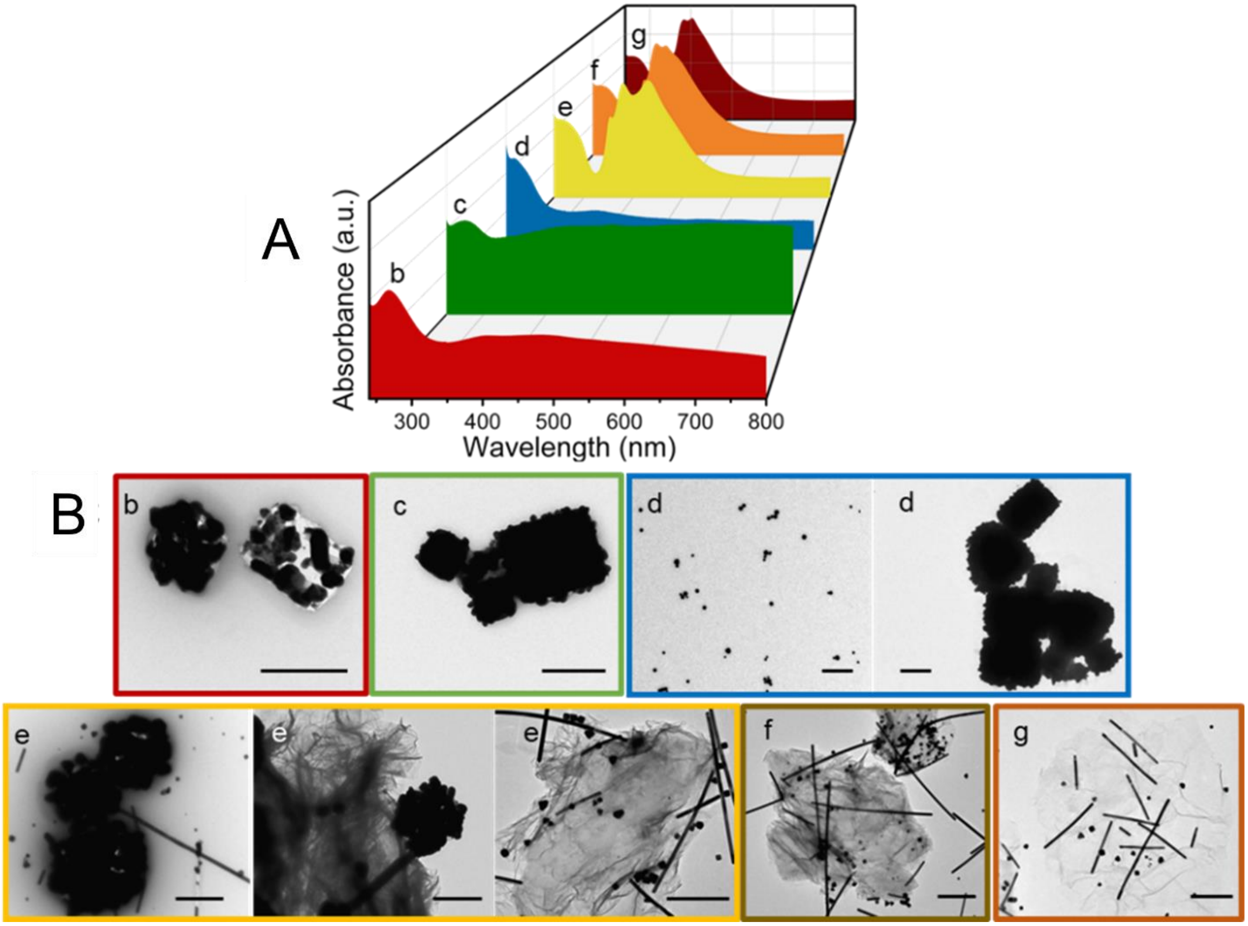

Figure 2.11 (A) UV-Vis absorption spectra of the synthesis mixture after the second (b), fourth (c), sixth (d), seventh (e), ninth (f) and tenth (g) $AgNO_3$ solution injection and (B) TEM micrographs of the aliquots withdrawn from the synthesis mixtures in (b), (c), (d), (e), (f) and (g) panel A. The synthesis was performed with the 10:1 $AgNO_3$:His-RGO w/w, 7.7:1 PVP:$AgNO_3$ molar ratio, at 170°C, PVP 360 kDa, stirring rate of 600 rpm, reaction time of 6.5 h, and His-RGO was added between the seventh and the eight injections of $AgNO_3$. Absorption spectra have been registered in ethanol and normalized at the characteristic absorption peak of the PVP:Ag(I) complex at 270 nm [38].

After the seventh $AgNO_3$ injection and subsequent addition of His-RGO, the solution turns dark grey (Figure 2.3F), accompanied by significant changes in its absorption spectrum. A large plasmon absorption band emerges, with superimposed quadrupole resonance and transversal plasmon peaks of NWs at 350 nm and 380 nm, respectively, along with a LSPR peak of spherical Ag NPs at 430 nm (trace e, Figure 2.11A). These peaks persist in the subsequent additions of AgNO3 up to the tenth injection (traces f-g, Figure 2.11A).

The TEM micrographs of the nanostructures isolated after the seventh injection show filaments protruding from the nodules homonucleated in the synthesis solution and from nodules anchored or wrapped by the His-RGO sheets, Ag NWs already anchored or wrapped onto the sheets, as well as homonucleated Ag NWs and Ag NPs of ca. 36 nm (trace e of Figure 2.11B). These micrographs confirm that the addition of His-RGO after the seventh injection of $AgNO_3$, which is known as the primarily responsible for the NWs growth in the synthesis of neat Ag NWs, does not affect filaments initiation in solution, that starts also from the nodules anchored onto the His-RGO basal plane, as also observed in Figure 2.8D.

The TEM images of the ninth and tenth aliquots show that after the subsequent additions of $AgNO_3$, the NWs grow anchored onto the sheets and in the supernatant reaction solution, as well as the spherical Ag NPs that reach a final size of ca. 50 nm (traces f-g of Figure 2.11B).

In view of these results, as for the synthesis of neat Ag NWs, it can be inferred that after the first injection of $AgNO_3$, AgCl nanocubes form (step I, Figure 2.12), and, having the latter a solubility constant lower than that of $AgNO_3$ [34], they slowly release Ag+ ions buffering their concentration in the reaction solution [23] and limiting Ag atoms nucleation events, which occur by means of reduction with glycolaldehyde [23].

High concentration of Ag(I) ions, in fact, has been demonstrated to favor heteronucleation of small Ag clusters, that can then dissolve and contribute to the formation of micrometer sized structures by Ostwald ripening [18], instead of the more thermodynamically stable pentagonally twinned prisms, which are the seeds promoting the uniaxial growth of the NWs. Micrometer sized structures have been observed in literature at relatively low injection rates, since low concentrations of Ag(I) ions lead to dissolution of small Ag NPs by Ostwald ripening, that feeds Ag(I) ions larger Ag NPs [18].

At the second injection of $AgNO_3$, the Ag atoms concentration overcomes supersaturation [39] reaching minimum nucleation concentration, and thus turns into the homonucleation of few Ag NPs. Under these conditions, the heteronucleation of Ag clusters concomitantly takes place at the surface of the AgCl nanocubes, thus generating the nodules, which are stabilized both electrostatically, by the electrostatic repulsions among the Cl^- ions chemisorbed at their surface [28], and sterically, by PVP (step II, Figure 2.12). Such processes occur until the fifth injection, as the further added Ag precursor on one side increases the concentration of the Ag NPs, that keep their size constant over the additions, and, on the other hand contributes to the growth of the Ag nodules by deposition of metal monomers at their surface.

It has been inferred that the low concentration of Ag monomers in solution promotes, onto the nodules surface, the heteronucleation of pentagonally twinned prisms (step III, Figure 2.12) which are the seeds initiating the anisotropic growth of the NWs, with formation of the filaments from the nodules (step IV, Figure 2.12), in thermodynamic control conditions [23].

In this process, the temperature of the reaction has been demonstrated crucial to induce both the relatively fast thermal conversion of EG to glycolaldehyde [25] and to provide the thermal energy required for the conversion of some of the Ag nodules in the pentagonally twinned prisms, which are more thermodynamically stable [18]. The synthesis of the Ag NWs has been reported in literature for temperatures between 110°C and 200°C. At 110°C, the NWs form with long reaction times (12 h) [40], while for higher temperatures their formation is faster and occurs in few hours [28]. In this work, the temperature of 170°C has been selected, as it has been demonstrated to lead to Ag NWs in high yield [18], because, keeping fixed the AgNO3 precursor concentration, a further increase of temperature would bring to a higher concentration of pentagonally twinned seeds, and therefore, to Ag NWs with a lower aspect ratio [18].

These seeds have a face-centered cubic structure, with the {111} planes denser in atoms and in twin boundaries than the {100} facets, and hence, have higher surface energy [26, 27]. As PVP preferentially adheres on the {100} planes restraining their growth kinetics, it promotes uniaxial elongation of the NWs by fast addition of Ag atoms onto the {111} facets. The thermodynamic control of the synthesis process of the NWs is granted by the combination of the slow release of Ag+ ions in solution, which keeps low the concentration of Ag atom monomers, and the selective coordination of PVP to the {100} facets of the prisms.

In the nanocomposite, the anisotropic growth of the Ag NWs was found dependent on the molecular weight of PVP, on the $AgNO_3$:PVP molar ratio, injection mode of the His-RGO complex and on its dissociation state. Neat Ag NWs have been effectively synthesized by using PVP at the Mw of 55 kDa [18], but in presence of His-RGO, such a low Mw was found ineffective in assisting and promoting the anisotropic growth of the NWs (Figure 2.9 B and C), likely due to: i. competition of the functionalities of His grafted on the sheets in coordinating the Ag NWs surface in growth, and ii. steric hindrance of His-RGO, that limits Ag atoms monomers diffusion in solution, resulting mostly in spherical and micrometer sized Ag nanostructures.

The results of Figure 2.11 showed that, until the sixth injection of $AgNO_3$, the Ag atom monomer concentration favours the homonucleation of spherical Ag NPs, as well as of nodules (Steps II-III, Figure 2.12), and at the sixth injection, the concentration of the Ag NPs increases, while their size significantly decreases. At the seventh injection, it is likely that initiation of Ag filaments from the pentagonally twinned seeds occurs (Steps IV of Figure 2.12), thanks to the dissolution, by Oswald ripening [25], of the small Ag NPs (Steps V of Figure 2.12), which have a high surface energy due to their high surface to volume ratio, and hence, feed of Ag atoms the {111} facets of the pentagonally twinned filaments [25].

After the injection of the His-RGO complex, both the filaments in growth anchor the His-RGO basal plane by coordination to its carboxylic groups, as well as the Ag nodules initiators of the filament growth (Step VI of Figure 2.12). In the following additions, the size of the Ag NPs increases due to Oswald ripening phenomena, as well as that of the NWs (Step VII of Figure 2.12). It is worth noticing that for times of reaction between 5 h and 6.5 h, the monodispersion of the Ag NWs in the nanocomposite increases without resorting to any size separation, any change of the temperature of reaction, any step of separation by precipitation, redispersion in solvent, reflux, and any addition of PVP [39]. This evidence, that, to the best of our knowledge, has never been discussed in literature for the synthesis of nanocomposites formed of graphene and Ag NWs, is reasonable due to the size focusing phenomenon (Step VII of Figure 2.12) [41]. This result allows to infer that, at the investigated temperature, the PVP ligand molecules coordinated at the NWs defect sites, which have higher chemical reactivity due to twinning boundaries and possessing strong microstress with lower lattice stabilization energy, promote an extensive transportation/exchange of ligated clusters/atoms from longer and larger NWs, that dissolve in the solvent and deposit on the shorter and thinner NWs, ultimately reaching an equilibrium between etching and redeposition processes, allowing the system to move toward the focusing conditions with the formation of monodisperse NWs (Step VII of Figure 2.12).

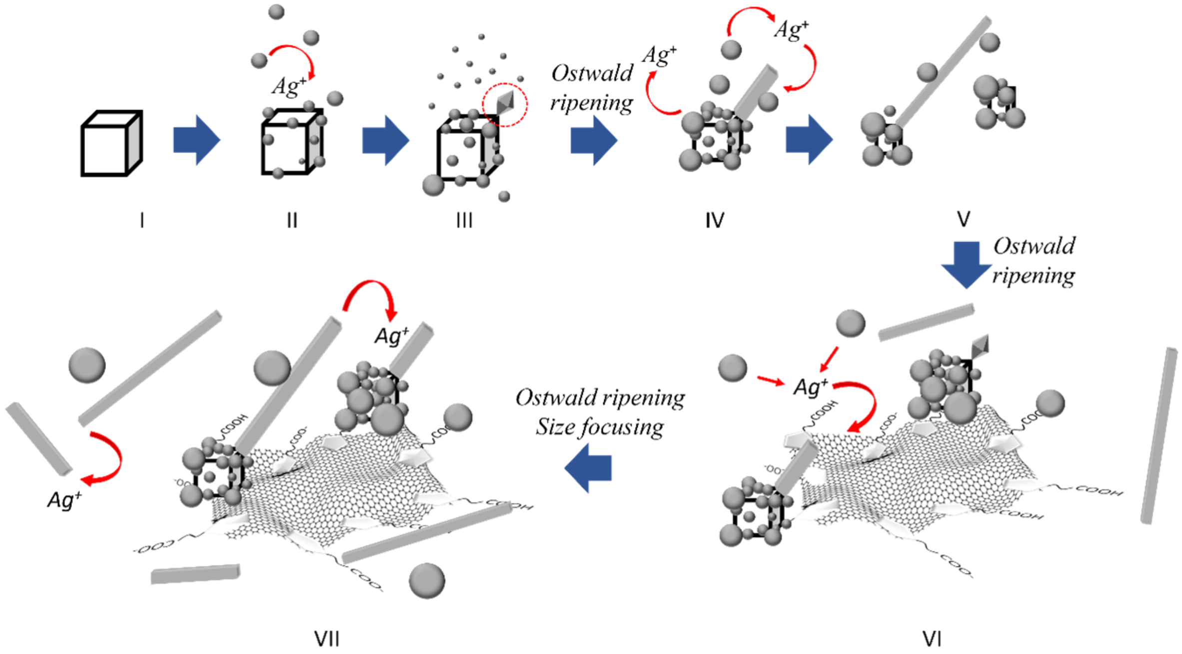

Figure 2.12 Sketch of the synthesis reaction mechanism of His-RGO/Ag NWs.

The synthesis mechanism can be thought to involve AgCl nanocube formation, followed by Ag NP nucleation and growth, heteronucleation at cube surfaces, and subsequent growth into nodules. Later injections lead to the formation of pentagonally twinned prisms, initiating NW growth. The addition of His-RGO complex facilitates filament initiation and growth. Oswald ripening processes occur, promoting Ag NP dissolution and NW growth. The PVP ligand aids in size focusing of NWs through ligand exchange processes, leading to monodisperse NWs without further manipulation.

2.8 Conclusions

A novel colloidal hybrid nanocomposite based on histidine (His) functionalized RGO flakes (His-RGO), decorated with polyvinylpyrrolidone (PVP)-capped Ag NWs, has been prepared by a new modified self-seeding polyol approach, relying on a merged *ex situ* and *in situ* synthesis procedure. The functionalization of RGO with His allows its phase exfoliation in water, avoiding the use of organic hazardous solvents and providing its dispersion in the green solvent ethylene glycol (EG). The slow injection of the $AgNO_3$ precursor in a solution of PVP and NaCl in EG yields to nucleation of AgCl nanocubes, that, releasing slowly Ag(I) ions, which are reduced by EG onto their surface in Ag nanostructures, form nodule-like structures, as well as Ag NPs. Among the nanostructures heteronucleated at the nodules surface, pentagonally twinned prisms form, from which filaments, that are feed by the Ag atoms produced in Oswald Ripening processes involving the spherical NPs, grow, anchored, or wrapped, by coordination, to the carboxyl functionalities of the His-RGO complex, that is added to the synthesis solution after anchoring of the AgCl nanocubes onto the His-RGO basal plane and after heteronucleation of the pentagonally twinned prisms.

The slow release of Ag(I) ions, combined with the selective coordination of PVP at the {100} planes of the pentagonally twinned seeds and filaments, allow the synthesis to proceed in thermodynamic control conditions. Size focusing phenomena, promoting an extensive transportation/exchange of ligated clusters/atoms from longer and larger NWs to shorter and thinner NWs, allow the system to move toward focusing conditions granting NWs monodispersion. A suitable tuning of the His-RGO dissociation state, $AgNO_3$:His-RGO w/w, molecular weight of PVP, PVP:$AgNO_3$ molar ratio, stirring rate and reaction time, allows the preparation of the hybrid nanocomposite made of His-RGO sheets decorated by monodisperse Ag NWs, 2.5 ± 0.9 μm long and 0.05 ± 0.01 μm thick, in a high wire-to-particle concentration.

The developed synthesis approach can be optimized for the manufacture of His-RGO/Ag NWs hybrid nanocomposites based on longer NWs by using PVP at higher molecular weights or other nanocomposites based on inorganic nanostructures having different composition and hence diverse chemical physical properties. The synthesized nanocomposite can be applied in electrochemical and SERS (bio)sensors, pressure and temperature sensors, flexible heaters, in multifunctional coatings showing antimicrobial properties combined with electrical conductivity and UV-light protection capability, in thermal management, in flexible transparent electrodes to integrate in optoelectronic systems, and in electromagnetic interference (EMI) devices.

References

1. Vischio, F., et al., *Au nanoparticles decorated nanographene oxide-based platform: Synthesis, functionalization and assessment of photothermal activity.* Biomaterials Advances, **2023**. 145: p. 213272.
2. Ingrosso, C., et al., *Au nanoparticle in situ decorated RGO nanocomposites for highly sensitive electrochemical genosensors.* Journal of Materials Chemistry B, **2019**. 7(5): p. 768-777.
3. Li, G., et al., *Lamellar α-Zirconium phosphate nanoparticles supported on N-doped graphene nanosheets as electrocatalysts for the detection of levofloxacin.* ACS Applied Nano Materials, **2023**. 6(18): p. 17040-17052.
4. He, Y., et al., *Construction of graphene oxide-coated zinc tetraphenyporphyrin nanostructures for photocatalytic CO2 reduction to highly selective CH4 product.* Journal of Colloid and Interface Science, **2023**. 638: p. 123-134.
5. Song, H., et al., *Two-dimensional materials for thermal management applications.* Joule, **2018**. 2(3): p. 442-463.
6. Ingrosso, C., et al., *Photoelectrochemical properties of Zn (II) phthalocyanine/ZnO nanocrystals heterojunctions: nanocrystal surface chemistry effect.* Applied surface science, **2005**. 246(4): p. 367-371.
7. Georgakilas, V., et al., *Noncovalent functionalization of graphene and graphene oxide for energy materials, biosensing, catalytic, and biomedical applications.* Chemical reviews, **2016**. 116(9): p. 5464-5519.
8. Jin, Y., et al., *Long-term stable silver nanowire transparent composite as bottom electrode for perovskite solar cells.* Nano Research, **2018**. 11: p. 1998-2011.
9. Cao, M., et al., *Wearable rGO-Ag NW@ cotton fiber piezoresistive sensor based on the fast charge transport channel provided by Ag nanowire.* Nano Energy, **2018**. 50: p. 528-535.
10. Goh, M.S., et al., *A chemical route to increase hot spots on silver nanowires for surface-enhanced Raman spectroscopy application.* Langmuir, **2012**. 28(40): p. 14441-14449.
11. Li, Y., et al., *Incorporating Ag nanowires into graphene nanosheets for enhanced thermal conductivity: implications for thermal management.* ACS Applied Nano Materials, **2020**. 3(6): p. 6061-6070.
12. Jia, H., et al., *A one-step graphene induction strategy enables in-situ controllable growth of silver nanowires for electromagnetic interference shielding.* Carbon, **2021**. 183: p. 809-819.
13. Chen, S., et al., *Preparation of graphene films bridged with Ag nanowires and its application in heterojunction solar cells.* Solar Energy, **2020**. 198: p. 167-174.
14. Manikandan, A., et al., *Graphene-coated copper nanowire networks as a highly stable transparent electrode in harsh environments toward efficient electrocatalytic hydrogen evolution reactions.* Journal of Materials Chemistry A, **2017**. 5(26): p. 13320-13328.
15. Kim, Y.-K., S.W. Han, and D.-H. Min, *Graphene oxide sheath on Ag nanoparticle/graphene hybrid films as an antioxidative coating and enhancer of surface-enhanced Raman scattering.* ACS applied materials & interfaces, **2012**. 4(12): p. 6545-6551.
16. Zhang, L., et al., *Surface-assisted assembly of a histidine-rich lipidated peptide for simultaneous exfoliation of graphite and functionalization of graphene nanosheets.* Nanoscale, **2019**. 11(6): p. 2999-3012.
17. Elumalai, S., et al., *An experimental and steered molecular dynamics simulation approach to histidine assisted liquid-phase exfoliation of graphite into few-layer graphene.* Physical Chemistry Chemical Physics, **2020**. 22(18): p. 9910-9914.
18. Coskun, S., B. Aksoy, and H.E. Unalan, *Polyol synthesis of silver nanowires: an extensive parametric study.* Crystal Growth & Design, **2011**. 11(11): p. 4963-4969.
19. Mesu, J.G., et al., *Infrared and Raman spectroscopic study of pH-induced structural changes of L-histidine in aqueous environment.* Vibrational spectroscopy, **2005**. 39(1): p. 114-125.

20. Verma, C. and E.E. Ebenso, *Ionic liquid-mediated functionalization of graphene-based materials for versatile applications: a review.* Graphene Technology, **2019**. 4: p. 1-15.
21. Azani, M.R. and A. Hassanpour, *Synthesis of silver nanowires with controllable diameter and simple tool to evaluate their diameter, concentration and yield.* ChemistrySelect, **2019**. 4(9): p. 2716-2720.
22. Dong, Y.-Y., et al., *Synthesis and characterization of Ag@ AgCl-reinforced cellulose composites with enhanced antibacterial and photocatalytic degradation properties.* Scientific Reports, **2021**. 11(1): p. 3366.
23. Schuette, W.M. and W.E. Buhro, *Silver chloride as a heterogeneous nucleant for the growth of silver nanowires.* Acs Nano, **2013**. 7(5): p. 3844-3853.
24. Sun, Y. and Y. Xia, *Shape-controlled synthesis of gold and silver nanoparticles.* science, **2002**. 298(5601): p. 2176-2179.
25. Skrabalak, S.E., et al., *On the polyol synthesis of silver nanostructures: glycolaldehyde as a reducing agent.* Nano letters, **2008**. 8(7): p. 2077-2081.
26. Sun, Y. and Y. Xia, *Large-scale synthesis of uniform silver nanowires through a soft, self-seeding, polyol process.* Advanced Materials, **2002**. 14(11): p. 833-837.
27. Wiley, B., Y. Sun, and Y. Xia, *Synthesis of silver nanostructures with controlled shapes and properties.* Accounts of chemical research, **2007**. 40(10): p. 1067-1076.
28. Bergin, S.M., et al., *The effect of nanowire length and diameter on the properties of transparent, conducting nanowire films.* Nanoscale, **2012**. 4(6): p. 1996-2004.
29. Sun, Y., et al., *Uniform silver nanowires synthesis by reducing AgNO3 with ethylene glycol in the presence of seeds and poly (vinyl pyrrolidone).* Chemistry of Materials, **2002**. 14(11): p. 4736-4745.
30. Wiley, B., et al., *Polyol synthesis of silver nanoparticles: use of chloride and oxygen to promote the formation of single-crystal, truncated cubes and tetrahedrons.* Nano Letters, **2004**. 4(9): p. 1733-1739.
31. De Guzman, N. and M.D.L. Balela, *Growth of ultralong Ag nanowires by electroless deposition in hot ethylene glycol for flexible transparent conducting electrodes.* Journal of Nanomaterials, **2017**. 2017(1): p. 7896094.
32. Song, Y.-J., et al., *Investigation on the role of the molecular weight of polyvinyl pyrrolidone in the shape control of high-yield silver nanospheres and nanowires.* Nanoscale research letters, **2014**. 9: p. 1-8.
33. Xu, C., R.-s. Yuan, and X. Wang, *Selective reduction of graphene oxide.* New Carbon Materials, **2014**. 29(1): p. 61-66.
34. Korte, K.E., S.E. Skrabalak, and Y. Xia, *Rapid synthesis of silver nanowires through a CuCl-or CuCl 2-mediated polyol process.* Journal of Materials Chemistry, **2008**. 18(4): p. 437-441.
35. Chen, C., et al., *Study on the synthesis of silver nanowires with adjustable diameters through the polyol process.* Nanotechnology, **2006**. 17(15): p. 3933.
36. Chen, M., et al., *Layer-by-layer assembly of Ag nanowires into 3D woodpile-like structures to achieve high density "hot spots" for surface-enhanced Raman scattering.* Langmuir, **2013**. 29(23): p. 7061-7069.
37. Im, S.H., et al., *Large-scale synthesis of silver nanocubes: the role of hcl in promoting cube perfection and monodispersity.* Angewandte Chemie International Edition, **2005**. 44(14): p. 2154-2157.
38. Tang, J., et al., *Chemical-etched silver nanowires with tunable rough shape for surface enhanced Raman scattering.* Colloids and Surfaces A: Physicochemical and Engineering Aspects, **2021**. 630: p. 127521.
39. Shimpi, J.R., D.S. Sidhaye, and B.L. Prasad, *Digestive ripening: a fine chemical machining process on the nanoscale.* Langmuir, **2017**. 33(38): p. 9491-9507.
40. Jiu, J., et al., *Facile synthesis of very-long silver nanowires for transparent electrodes.* Journal of Materials Chemistry A, **2014**. 2(18): p. 6326-6330.

41. Mozaffari, S., et al., *The role of nanoparticle size and ligand coverage in size focusing of colloidal metal nanoparticles.* Nanoscale Advances, **2019**. 1(10): p. 4052-4066.

CHAPTER 3

Electrochemical sensors based on Ag nanowires decorated histidine-reduced graphene oxide for carbofuran detection in real water samples

3.1 Introduction

The issue of environmental pollution is becoming increasingly severe, despite advancements in science and technology. A major contributor to this problem is the accumulation of pesticide residues in rivers, sea and soil due to the excessive use of organophosphate (OP) and carbamate (CB) pesticides in the agriculture sector. This situation poses significant threats to both human health and non-target organisms, also compromising environmental sustainability [1]. Therefore, there is a growing emphasis in modern research on developing rapid and accurate methods to detect pesticide residues in soil, food, and natural water resources.

Carbofuran (CF, 2,3-dihydro-2,2-dimethylbenzofuran-7-ol methyl carbamate), also known by its trade names Furadan or Curaterr, is a carbamate ester belonging to the 1-benzofuran family. CF is an odorless, white, crystalline solid with a melting point ranging between 150-154 ºC. CF is slightly soluble in water, as well as in organic solvents as N-methyl-2-pyrrolidone, dimethylformamide, dimethyl sulfoxide, acetone, acetonitrile, methylene chloride, cyclohexanone, benzene, and xylene. CF is quite stable under neutral and acidic conditions and decomposes only under alkaline conditions [2]. The U.S Environmental Protection Agency (U.S EPA) has set the maximum allowed contaminant level (MCL) of CF in drinking water at

1.8 x 10^{-7} M and higher levels are considered dangerous for human health. CF is widely used in agriculture and forestry as a broad-spectrum systemic insecticide, primarily for controlling insects and worms [3-5]. Due to its relatively low environmental persistence and broad biological efficacy, CF has become a preferred alternative to organochlorine insecticides, which tend to persist in the environment for longer times [6, 7]. The insecticidal action of CF is primarily mediated through N-methyl carbamate, which is derived from carbamic acid and inhibits acetylcholinesterase activity at neural synapses and neuromuscular junctions, resulting in the disruption of normal nerve function [8]. The acute toxicity of CF varies among organisms. In mammals, CF is more toxic when ingested or inhaled compared to dermal exposure. Exposure to CF through oral ingestion or inhalation can affect the nervous system, reproductive disorders, endocrine disruption and in severe cases, even fatality [9, 10]. Symptoms in humans include weakness, respiratory difficulties, excessive sweating, headaches, nausea, vomiting, abdominal pain, dizziness, and blurred vision [11, 12]. Higher levels can cause hypothermia, body tremors, muscular twitching, fasciculations, loss of coordination, convulsions, and halted breathing, which can lead to death from respiratory failure [13, 14]. Given the risks associated with CF contamination in agricultural products and wastewater, effective methods for detecting and mitigating CF contamination are essential [15, 16].

Many studies have been conducted to determine the CF level in fruits, vegetables, and wastewater. These include enzyme-linked immunosorbent assay (ELISA) [17], high-performance liquid chromatography (HPLC) [18], fluorimetry [19], gas chromatography [20], mass spectrometry [21], spectrophotometry [22], and electrochemical methods [23-27]. These techniques, however, require expensive and complex instruments and technologies, specialized operators, are time-consuming and are not suitable for *in-field* use, because they are cumbersome. As an alternative to these approaches, electrochemical methods have been developed for the detection of pesticides in the environment and agricultural products [28-31], because they are rapid, less expensive, lightweight, portable and suitable for miniaturization and *on-site* use. Moreover, in electrochemical sensors the modification of the electrode surface can enhance sensitivity and selectivity in the analysis.

The electrochemical methods which have been used for the detection of CF, commonly focus on targeting the nervous system enzyme acetylcholinesterase (AChE), which is inhibited by the action of OP and CB pesticides [32-35]. Enzyme-based electrochemical biosensors show, in fact, potential for real-time pesticide monitoring, particularly when miniaturized into portable devices. However, the use of enzymes is critical, because of their low stability, storage constraints, and optimum conditions such as pH, temperature, and so forth. The requirements of a controlled environment for enzyme and the low reproducibility, in turn, reduce the life span of these biosensors, limiting their practical applications [32, 36].

To overcome these challenges, the nonenzymatic electrochemical techniques have gained significant attention in recent years, as they offer a more rapid, cost-effective, and sensitive approach for detecting both organic and inorganic substances [37-40]. A key strategy in developing effective nonenzymatic sensors involves modifying the transducer surface with suitable nanomaterials of diverse morphologies (nanoparticles, nanotubes, 2D nanostructures, nanowires) and chemical composition (metal oxides, metals, sulfides, and nanostructured carbon-based compounds), possessing superior electrochemical reactivity and electrocatalytic properties, facilitating oxidation of pesticides at the electrode surface, and offering a large surface area for an high loading capacity and an increased number of active sites, which significantly amplify signals in the electrochemical quantification [41]. Notably, the combination of these materials often results in synergistic effects, enhancing stability, selectivity, and reproducibility of the fabricated electrodes. The sensitivity of such sensors has been further improved by implementing highly specific electrochemical (bio) sensing approaches, such as immune sensing, enzymatic sensing, molecularly imprinted polymers (MIP), or ion-imprinted polymers (IIP). As an example, Yaqub et.al [42] fabricated a novel nonenzymatic electrochemical sensor by using a nanohybrid assembly, based on cobalt-substituted Dawson-type polyoxometalate (Co-POM) and polyethyleneimine (PEI)-capped Ag nanoparticles (NPs), that was integrated onto GCEs by layer-by-layer self-assembly. Ag NPs have been largely studied for their potential as effective electrocatalysts for the oxidation and detection of pesticides. The device has reached a LOD of 0.1mM, with a sensitivity of 13.11 μAmM^{-1}, was achieved for CF.

Graphene derivatives have been widely employed in electrochemical sensors due to their high conductivity, high electrocatalytic activity, and extremely fast heterogeneous electron transfer kinetics [43]. These properties, along with their high chemical reactivity, have paved the way for the development of various functional nanocomposite materials formed of graphene derivatives functionalized by NPs and biomolecules, making them ideal for sensing applications [44]. The enhanced electrochemical activity of graphene can be attributed to two main factors: (1) its large surface area, provided by the 2D structure of graphene sheets, which offers a high number of electroactive sites, thereby increasing the sensitivity to target molecules [45], and (2) its stability over a vast range of temperature and voltages, making it a highly reliable conductive material for electrochemical sensor development. In addition, the sp^2-hybridized orbital system in graphene facilitates faster electron transfer kinetics, resulting in lower response times and lower LODs. For instance, Vinitha et al. [26] developed a (Gd_2S_3/rGO)-modified glassy carbon electrode (GCE) sensor for CF detection, achieving a low limit of detection (LOD) of 0.128 μM. Similarly, Balamurugan et al. demonstrated an electrochemical detection approach using $Dy_2Sn_2O_7$/GO composites, with an impressive LOD of 14.8 nM for CF [46]. The results depicted that the fabricated nonenzymatic hybrid film showed excellent electrocatalytic efficiency for CF oxidation.

Additionally, metal oxide-GO and metal NPs-GO composites have shown promise for electrochemical quantification of CF. GO nanocomposite decorated with Ag NPs (Ag@GO) was used to modify a GCE for detecting CF in vegetable samples [47]. The modified electrode can detect CF in a wide detection range of 1 to 1000 μM, with a low LOD of 10 nM.

Two-dimensional (2D) transition metal dichalcogenide nanomaterials, such as molybdenum disulfide (MoS_2), have garnered significant attention due to their unique, tunable electrical properties, which depend on factors like crystal structure, nanosheet size, and surface defects [48]. The preparation of hybrid nanocomposites based on graphene derivatives decorated with nanostructured MoS_2 results in materials showing enhanced stability, electron conductivity, heterogeneous electron transfer kinetics, and electrocatalytic activity [49]. Alagarsamy et al. [50] designed an electrochemical sensor based on cerium molybdenum oxide (CMO) nanoparticles that were decorated on the face of boron doped reduced graphene oxide nanocomposite synthesized through the co-precipitation process and modified on the surface of glassy carbon electrode (GCE) for the determination of CF. The CMO/B-rGO/GCE electrochemical sensor exhibits higher selectivity and sensitivity of 4.06 $\mu A \mu M^{-1} cm^{-2}$, a low LOD of 0.002 μM with the linear ranges 0.01–365 μM. The prepared sensor was tested in the real food samples towards the determination of CF. Haritha et al. [51] fabricated a voltametric sensor for the accurate detection of CF residues utilizing the cyclic voltammetry technique. The constructed sensor has displayed a linear range of carbofuran detection from 10-90 μM, with a LOD of 0.38 μM and sensitivity of 0.303 $\mu A\ \mu M^{-1}\ cm^{-2}$. The developed sensor has been employed to monitor CF residues in real soil and water samples and it shows a recovery greater than 95 %, enables the cost-effective monitoring of carbofuran in real samples.

In 2011, Liu et al. developed an advanced electrochemical sensor by modifying an RGO-Au nanocomposite electrode with carboxy phenylboronic acid and immobilized acetylcholinesterase (AChE). The sensor demonstrated the capability to detect multiple pesticides, including chlorpyrifos, malathion, carbofuran, and isoprocarb, at LODs of 0.1, 0.5, 0.05, and 0.5 μg/L, respectively [52]. Similarly, Tan et al. developed an electrochemical sensor based on a RGO-Au nanocomposite for the detection of CF using differential pulse voltammetry, in a solution containing 5.0×10^{-3} mol/L $K_3[Fe(CN)_6]$ and 0.1 mol/L KCl (pH 7.0), and showing a LOD as low as 20 nM, that was achieved thanks to the fast binding kinetics of CF. Hashemi et al. developed a RGO–Cu/CuO–Ag nanocomposite for detection of carbaryl and fenamiphos pesticides with LODs of 0.005 and 0.003 μM, respectively [53].

To the best of our knowledge, while extensive research has been conducted on the use of nanocomposites based on graphene and spherical metal NPs or metal oxides in the electrochemical detection of CF, there is a notable gap in studies exploring the fabrication of CF sensors using nanocomposites based on graphene derivatives decorated with Ag NWs. This gap is most likely due to the complexity of their synthesis, whose effectiveness depends by various experimental conditions affecting anisotropic growth and wire-to-particle yields, because the Ag NWs have been proven to show a high electrocatalytic activity [54], and thanks to their elongated morphology, can fill the gaps among graphene sheets favoring charge transfers, and increasing electrical conductivity of the electrode.

In this work, we have combined the promising chemical physical properties of RGO, functionalized with histidine (His), with those of the Ag NWs decorating its basal plane, for the electroactive detection of CF in aqueous solutions. For this purpose, screen-printed carbon electrodes (SPCEs) were modified with the His-RGO/Ag NWs hybrid nanocomposite to fabricate functional SPCE/His-RGO/Ag NW electrodes. To further enhance their sensitivity and selectivity, a layer of poly(3,4-ethylenedioxythiophene) polystyrene sulfonate (PEDOT:PSS) was applied through electrochemical polymerization, producing SPCE/His-RGO/Ag NW/PEDOT:PSS electrodes. The manufactured SPCEs/His-RGO/Ag NW/PEDOT:PSS have shown LOD 17.3 nM for carbofuran lower than the U.S. EPA recommended concentration in drinking water and comparable with the lowest ones reported in the literature (Table 3.3). Repeatability, reproducibility, storage stability, and selectivity of the electrodes, manufactured for the detection of the carbofuran in real samples of the complex aqueous matrix from tap and river water, have been assessed, supporting their technological potential for monitoring environmental threats.

3.2 Materials and methods

3.2.1 Preparation of the His-RGO/Ag NWs modified Screen Printed Electrodes (SPCEs/His-RGO/Ag NWs)

Screen-printed carbon electrodes (SPCEs) were modified by drop casting 5 µl the His-RGO/Ag NWs hybrid nanocomposite dispersions and are here indicated as SPCEs/His-RGO/Ag NWs. Then, they were further modified with poly(3,4-ethylenedioxythiophene)polystyrene sulfonate (PEDT:PSS) films achieved by electrochemical polymerization of 10 mM PEDOT:PSS monomers, by applying a voltage of 0.5 V for 300 s, resulting in the electrodes here called SPCEs/His-RGO/Ag NWs/PEDOT:PSS (Figure 3.1)

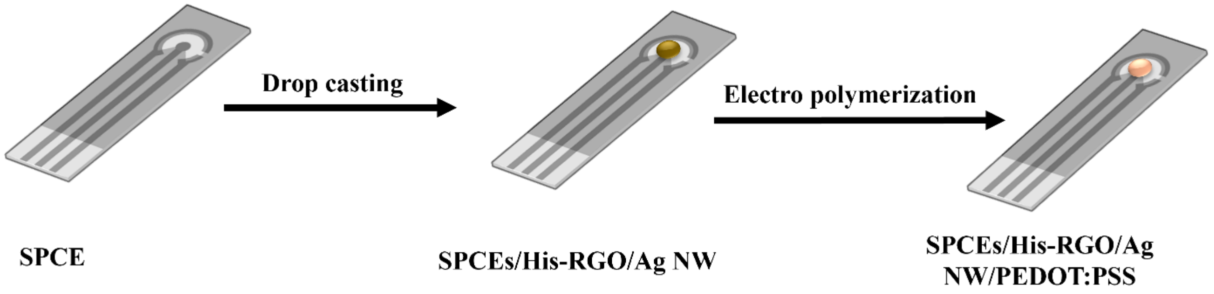

Figure 3.1. Sketch of the preparation of the SPCEs/His-RGO/Ag NWs and SPCE/His-RGO/Ag NW/PEDOT:PSS for the electroactive detection of carbofuran.

3.2.2 Electrochemical characterization of the SPCEs/His-RGO/Ag NWs

Cyclic voltammetry (CV) measurements of the bare SPCEs, SPCEs/His-RGO/Ag NWs and SPCEs/His-RGO/Ag NWs/PEDOT:PSS, were performed in a 0.01 M PBS buffer solution (pH 7.4) containing 0.1 M KCl and 5 mM $Fe[(CN)_6]^{3-/4-}$, at the scan rate of 10 mV s^{-1}.

Electrochemical impedance spectroscopy (EIS) measurements of the bare SPCEs, SPCEs/His-RGO/Ag NWs and SPCEs/His-RGO/Ag NWs/PEDOT:PSS were presented as Nyquist plots (complex plane diagrams), that were fitted by the Randles equivalent circuit and treated by the Nova® v1.11 software to quantitatively analyze the data. This circuit model allows to determine various electrochemical parameters, including solution *resistance*, charge transfer *resistance* (R_{et}), and double-layer capacitance. Charge transfer *resistance* (R_{et}) is particularly important, as it served as an analytical signal to assess the electron transfer properties at electrode-electrolyte interphase. The electroactive surface area (A_{ele}) of the prepared electrodes was estimated by using the Randles–Sevcik equation for a quasi-reversible system, as:

$$I_{ap} = (2.69 \times 10^5)\, A_{ele} \times C \times D^{1/2} \times n^{3/2} \times v^{1/2} \tag{1}$$

This calculation enabled the determination of the effective surface area participating in the electrochemical reactions.

The heterogeneous electron transfer rate constant (k_0) was estimated by using the following:

$$K_0 = R / (n^2 \times F^2 \times A_{ele} \times C \times R_{et}) \tag{2}$$

In Equations (1) and (2), I_{ap} is the anodic peak *current*, D is the diffusion coefficient of $Fe[(CN)_6]^{4-}$ in solution (6.5×10^{-6} cm^2 s^{-1}), R is the universal gas constant, F is the Faraday's constant, n is the number of electrons transferred in the redox reaction, v is the *potential* scan rate (Vs^{-1}) and C is the $[Fe(CN)_6]^{4-}$ concentration in the bulk solution (mol cm^{-3}).

3.2.3 Electroanalytical application of the sensing platforms

Chronoamperometry was used to detect carbofuran at the SPCEs/His-RGO/Ag NWs/PEDOT:PSS in 0.1M PBS buffer solution at pH 7.4, in the concentration range of 0.1 – 80 µM, at 0.26 V (vs. pseudo-Ag/AgCl).

Calibration plots were fitted to a linear model function (y = ax +b) by the weighted linear least squares method using Origin Pro 2018 (Origin Lab Corporation, USA) and w = 1/σi 2 as weight. The Limit of detection (LOD) was determined as:

$$LOD = 3.3 (sy/x/S) \tag{3}$$

where sy/x is the residual standard deviation and S is the slope of the calibration plot (calibration sensitivity) [55].

The limit of quantification (LOQ) was estimated as:

$$LOQ = 10 (sy/x/S) \tag{4}$$

All electrochemical measurements were performed six times to determine the relative standard deviation of the current values in calibration plots.

3.3 Results and discussions

3.3.1 Electrochemical characterization of the His-RGO/Ag NW modified SPCEs

SPCEs were modified with the His-RGO/Ag NW hybrid nanocomposite, showing, in the TEM micrographs, the sheet-like microstructures of the His-RGO complex coated by 4 ± 2 µm long and 0.17 ± 0.07 µm width Ag NWs (Figure 3.2A), as reported in the Materials and Methods section. The surface morphology of the SPCEs/His-RGO/Ag NWs were characterized by scanning electron microscopy (SEM). The SEM images of the neat SPCEs show a porous surface (Figure 3.2B) which significantly changes after deposition of the nanocomposite, showing the distinct wrinkled, sheet-like structures of the His-RGO, coated by the Ag NWs, as well as by nanometer-sized spherical Ag NPs (Figure 3.2C).

The modification of the SPCEs/His-RGO/Ag NWs by the *in situ* electrochemical polymerization of the PEDOT:PSS film, was assessed by cyclic voltammetry (CV) and electrochemical impedance spectroscopy (EIS) (Figure 3.2 D,E), that were performed in presence of the inner-sphere probe ($K_4[Fe(CN)_6]$). Such a molecule is characterized by electrochemical behavior that is more sensitive to chemistry (oxygen containing functionalities, impurities, and adsorption sites) and structure of the electrode material surface, rather than its electronic density of states (DOS), and hence ideal for assessing modifications of its surface.

The CV scans collected at the SPCEs/His-RGO/Ag NWs show a decrease of the anodic and cathodic peak *potential* difference (ΔEp) with respect to the bare SPCEs, which feature, instead, the couple of quasi reversible redox peaks typical of $Fe[(CN)_6]^{3-/4-}$ (Figure 3.2D). This reduction in ΔEp indicates a higher degree of reversibility of the redox reactions at the modified electrode surface, that is ascribed to a higher conductivity and higher electron transfer capability at the interface with the electrolyte, as assessed by the increase of the apparent heterogenous electron transfer kinetic constant (K_0) of such electrodes, estimated by using Equation (2) for a quasi-reversible system, with respect to the neat SPCEs (Table 3.1).

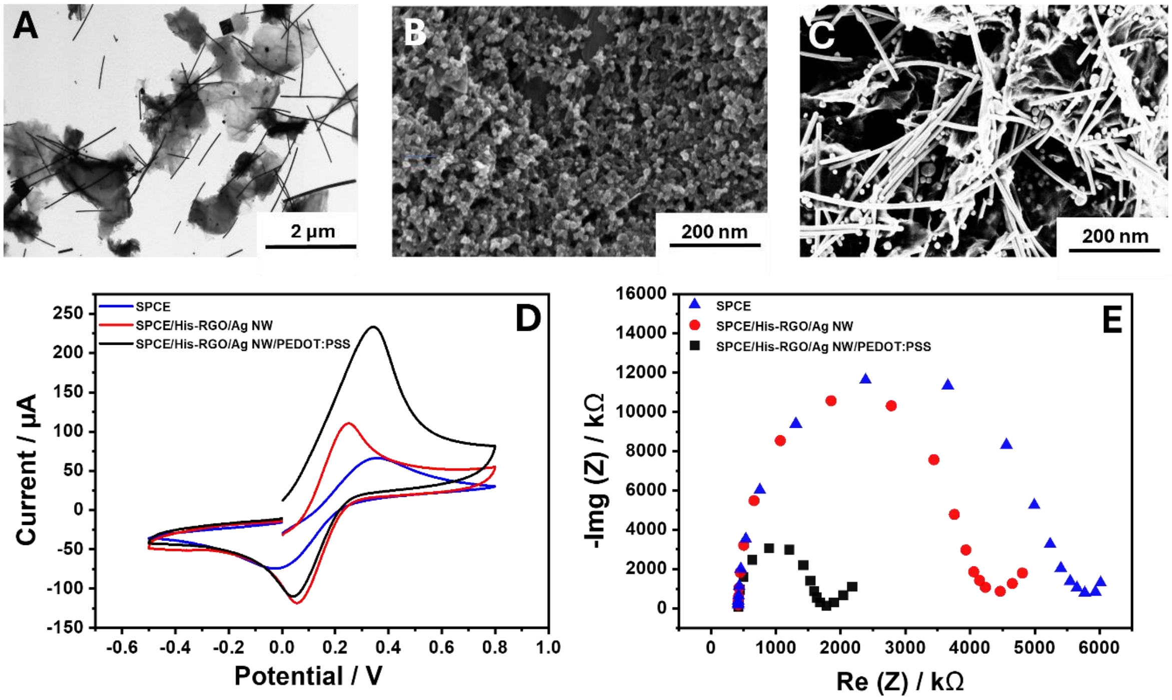

Figure 3.2 (**A**) TEM micrograph of the His-RGO/Ag NW, (**B**) SEM image of neat SPCEs and (**C**) SPCEs/His-RGO/Ag NW (127.92 KX). (**D**) CV scans and (**E**) EIS spectra collected at the SPCEs/His-RGO/Ag NW and SPCEs/His-RGO/Ag NW/PEDOT:PSS at 10 mV s^{-1}, in 0.01 M PBS buffer (pH 7.4) added by 5mM $Fe[(CN)_6]^{3-/4-}$ and 0.1 M KCL.

The increase of K0 in SPCEs/His-RGO/Ag NW is believed to result from the merging of the electrical conductivity of the Ag NWs and of the His-RGO sheets, which are linked by histidine, the coupling agent mediating the Ag NWs-RGO charge transfers [56].

Table 3.1. Peak-to-peak separation *potential* (ΔEp), electroactive surface area (A_{ele}), electron transfer *resistance* (Ret) and apparent heterogeneous electron transfer constant (K_0) of SPCEs, SPCEs/His-RGO/Ag NW and SPCEs/His-RGO/Ag NW/PEDOT:PSS.

Electrode	ΔEp	K_0/cm s^{-1}	A_0/A cm^{-2}	R_{et}/kOhm
Bare SPCE	383.06	1.26	0.083	5243.78
SPCEs/His-RGO/Ag NW	194.73	2.16	0.137	3935.32
SPCEs/His-RGO/AgNWs/PEDOT:PSS	302.7	1.94	0.176	1597.01

Also, the presence of long Ag NWs which fill the gaps between adjacent His-RGO sheets across the film deposited onto the SPCEs ensures effective electrical contact and enhances the overall conductivity of the electrode. Finally, the increase of K_0 is also accounted for by the presence of the Ag NWs catalyzing the $[Fe(CN)_6]^{3-/4-}$ red/ox processes at the electrode surface [56].

Upon electro polymerization of PEDOT:PSS, also the SPCEs/His-RGO/AgNWs/PEDOT:PSS electrodes showed a peak *potential* difference (ΔEp) and a K_0 value respectively lower and higher with respect to those of the bare SPCEs, likely due to the high electrical conductivity of the polymer.

Finally, both SPCEs/His-RGO/Ag NWs and SPCEs/His-RGO/Ag NWs/PEDOT:PSS showed an increase of the *current* intensity with respect to the bare SPCEs (Table 3.1), reasonably due to the 1.65- and 2-folds increase of the electroactive surface area (A_{ele}) of the modified electrodes (Table

3.1), estimated by the Randles–Sevcik equation (Eq. (1)), and attesting their higher electrochemical reactivity.

The evidence found in the CV scans are confirmed by the Faradaic impedance spectra (Figure 3.2E), that showed a reduction of the semicircle diameter of the EIS spectra of the SPCEs/His-RGO/Ag NWs with respect to the bare SPCEs (Figure 3.2E). This decrease is more evident for the SPCEs/His-RGO/Ag NWs/PEDOT:PSS and confirms the higher reversibility of the redox Fe$[(CN)_6]^{3-/4-}$ probe at such electrodes, as also assessed by the decrease of the electron transfer *resistance* (R_{et}) (Table 3.1) at the electrode-electrolyte interphase.

It is worth noticing that the behavior of the SPCEs/His-RGO/Ag NWs/PEDOT:PSS differs from that of the SPCEs/His-RGO/Ag NW, specifically in the ΔEp value, peak *current* intensity and R_{et}. The ΔEp in the SPCEs/His-RGO/Ag NW/PEDOT:PSS is slightly higher in comparison to the SPCEs/His-RGO/Ag NWs (Table 3.1), the peak *current* intensity shows a notable increase (Table 3.1), and R_{et} is lower (Table 3.1), indicating a higher electron transfer *resistance* at the electrode surface.

3.3.2 Electrochemical detection of carbofuran

The electrochemical performance of the bare SPCEs, SPCEs/His-RGO/Ag NWs and SPCEs/His-RGO/Ag NW/PEDOT:PSS was tested for the detection of carbofuran.

For this purpose, the optimization of the detection conditions, pH and electrolyte, was performed by collecting CV scans at different pH in the range of 2-12, and in presence of different electrolytes (NH_4Cl, $LiClO_4$, K_2SO_4, PBS, $NaNO_3$, KCl) (Figure 3.3). The CV scans show the highest oxidation peak *current* intensity at the pH of 7.4 (Figure 3.3A) and in presence of the PBS buffer (Figure 3.3B). Therefore, these conditions were used to compare the performance of the bare

SPCEs, SPCEs/His-RGO/Ag NWs and SPCEs/His-RGO/Ag NW/PEDOT:PSS in the detection of carbofuran, which was added to the PBS buffer solution at the 10 µM concentration, keeping constant the geometrical area of the electrode (4 mm diameter, 12.6 mm^2).

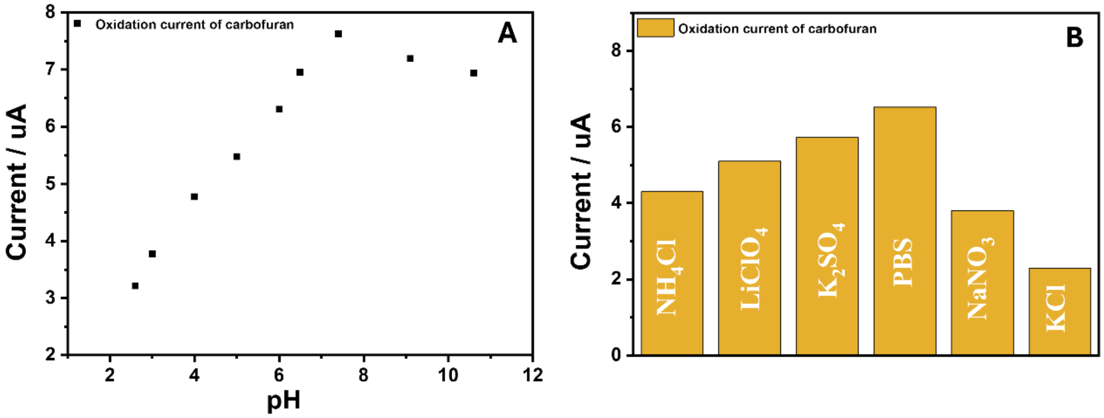

Figure 3.3 Optimization of the experimental parameters for the SPCEs/His-RGO/Ag NW/PEDOT:PSS: (A) study of pH with (B) different electrolytes.

The CV scans recorded at the bare SPCEs in presence of the pesticide show a weak and large oxidation shoulder at ca. 0.4 V, indicating a poor electrochemical response. In contrast, the SPCEs/His-RGO/Ag NWs and SPCEs/His-RGO/Ag NW/PEDOT:PSS present an intense signal at ca. 0.30 V (vs. pseudo-Ag/AgCl) (Figure 3.4).

The appearance of this peak at both the modified electrodes suggests the occurrence of oxidation of carbofuran, which evolves by hydrolysis to carbofuran phenol, that is an electroactive compound. The electrochemical oxidation of carbofuran to a phenolic derivative is well-documented and aligns with previous studies on similar organophosphate compounds [57-59].

The results of Figure 3.4 highlight the crucial role of the electrode surface modification in facilitating the electrochemical detection of carbofuran, which is otherwise not observable at the bare SPCEs. Both the SPCEs/His-RGO/Ag NWs and SPCEs/His-RGO/Ag NW/PEDOT:PSS demonstrated substantially higher sensitivity to carbofuran oxidation when compared to the bare SPCEs, while decreasing carbofuran oxidation *potential*.

Besides, a comparison of the oxidation peak *current*s between the modified electrodes shows that SPCEs/His-RGO/Ag NW/PEDOT:PSS exhibit higher sensitivity toward carbofuran oxidation than SPCEs/His-RGO/Ag NWs. This enhanced sensitivity can be attributed to the electrocatalytic properties of the Ag NWs [54], and to the electropolymerization of the conductive polymer PEDOT:PSS which enhances the electrochemical reactivity of the electrode, further amplifying its response, making the SPCEs/His-RGO/Ag NW/PEDOT:PSS highly suitable for carbofuran detection.

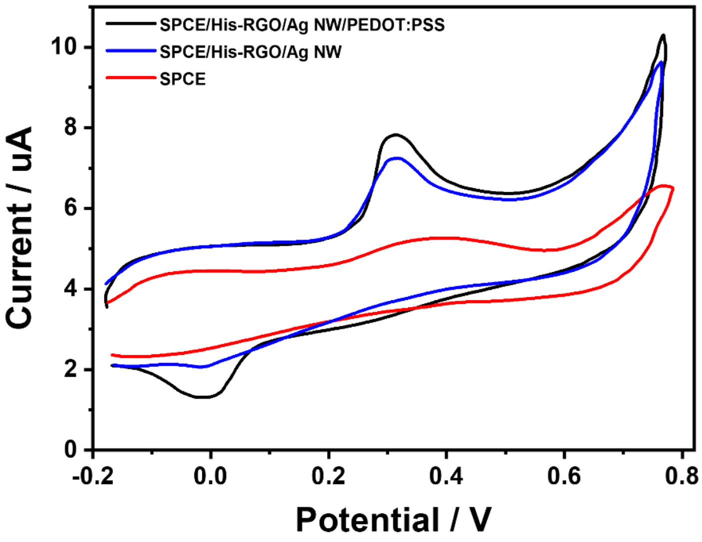

Figure 3.4 CV scan recorded at the SPCEs, SPCEs/His-RGO/Ag NW and SPCEs/His-RGO/Ag NW/PEDOT:PSS, at 10 mV s^{-1}, in 0.1 mM PBS (pH 7.4) added by 10 μM carbofuran.

Chronoamperometry measurements were performed in the 0.1-80 μM concentration range of carbofuran (Figure 3.5A) to construct calibration curves for its detection (Figure 3.5B) at the investigated SPCEs/His-RGO/Ag NWs/PEDOT:PSS, and to estimate sensitivity (S), limit of detection (LOD), and limit of quantification (LOQ), key analytical parameters to quantitatively evaluate the efficiency and reliability of the electrode in carbofuran detection for practical applications. Indeed, sensitivity reflects the electrode's ability to detect changes in analyte concentration, while the LOD and LOQ define the minimum concentration levels at which the analyte can be reliably detected and quantified, respectively.

The *current* response of the SPCEs/His-RGO/Ag NWs/PEDOT:PSS in the standard solutions of carbofuran shows a linear relationship (y = (a*b) x) over the investigated concentration range, with a correlation coefficient of r^2 = x (Figure 3.5B). This result allows us to infer the occurrence of two different electroactive kinetic processes caused by a change in the electrode surface chemistry occurring during the red/ox processes. At low concentrations, the electroactive process is controlled by the adsorption of the analyte on the electrode active sites and the sensitivity is high. On the contrary, at high concentrations, a partial saturation of the electrode active sites is expected to slow down the activation of the analyte molecules to the red/ox process, becoming the rate-determining step that induces a decrease in sensitivity [60].

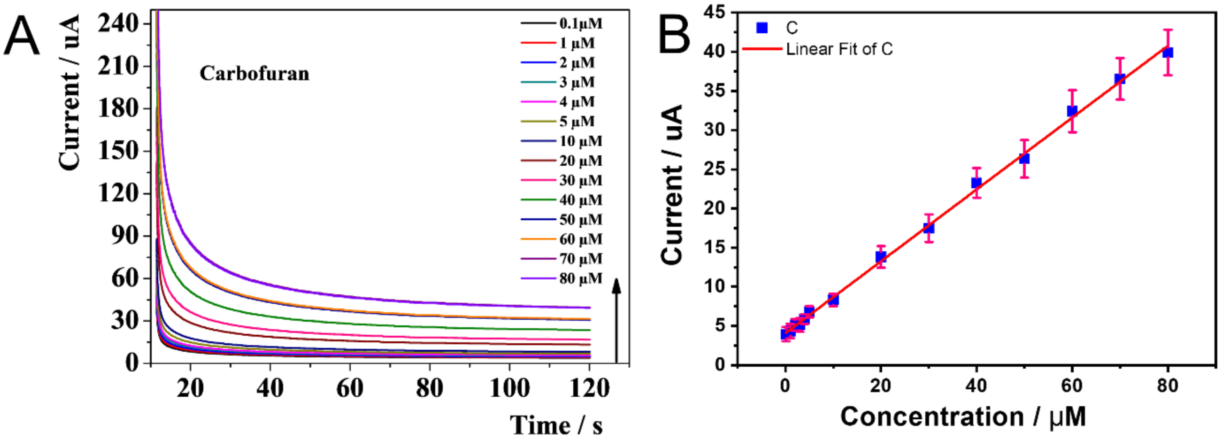

Figure 3.5 Chronoamperograms (**A**) and corresponding calibration plots (**B**) of carbofuran between 0.1–80 μM, in 0.1 mM PBS buffer (pH 7.4) at the SPCEs/His-RGO/AgNWs/PEDOT:PSS

Sensitivity (S), the limit of detection (LOD), the limit of quantification (LOQ) (Table 3.2), %RSD of repeatability, %RSD of reproducibility, and storage stability were determined to evaluate the performance of the SPCEs/His-RGO/Ag NWs/PEDOT:PSS in the detection of CF (Figure 3.6)

The results, summarized in Table 3.2, demonstrate that the SPCEs/His-RGO/Ag NW/PEDOT:PSS possess high sensitivity and a low LOD, making them highly suitable for the trace detection of carbofuran in aqueous samples. This evidence can be explained by the intrinsic porous structure of the conductive polymer PEDOT:PSS, that provides a large specific surface area offering abundant active sites for analyte molecules interaction and accumulation, thereby enhancing the sensitivity of the electrochemical sensor [61]. For instance, polyaniline has been effectively employed in electrochemical sensing applications, leveraging its porous nature to detect various analytes [62]. Similarly, polypyrrole's porous structure has been utilized to enhance sensitivity in gas sensing applications. The porous nature of PPy allows for rapid gas diffusion and interaction with the polymer matrix, leading to measurable changes in electrical conductivity upon gas adsorption [63]. Jiang et al. [64] synthesized three-dimensional porous conductive polymer hydrogels for *in situ* sensitive electrochemiluminescence (ECL) detection of hydrogen peroxide (H_2O_2) released from live cells, demonstrating the versatility of porous conductive polymers in electrochemical sensing. Comparing with the lowest values recently reported for similar state-of-the-art Ag/Au NPs based graphene nanocomposites synthesized by different approaches and deposited onto different electrodes (Table 3.3), our approach takes advantage of the high sensitivity and low LODs typical of the SPCEs, from their suitability for on-site use, where portable and disposable electrodes are highly demanding, and from their low cost, being low volumes of samples necessary for the analysis. These findings further underscore the utility of the His-

RGO/Ag NW nanocomposite as an effective material for enhancing the electrochemical performance of SPCEs in environmental and agricultural monitoring.

Table 3.2 Sensitivity (S), limit of detection (LOD), limit of quantification (LOQ) of the SPCEs/His-RGO/Ag NW/PEDOT:PSS towards 10 µM of carbofuran.

	Carbofuran
Sensitivity / µA μM^{-1}	0.458
LOD / nM	17.3
LOQ / nM	58.1

Table 3.3 Comparative table of the LODs of carbofuran sensors reported in literature

Electrode material	**Analyte**	**LOD (nM)**	**Reference**
AgNPs/GO/GCE	Carbofuran	10	[47]
CoPOM/PEI-AgNP/GCE		100000	[42]
AuNPs/GO-SPCE		220	[65]
MIP/rGO@AuNPs/GCE		20	[27]
AChE/CPBA/RGO-AuNPs/GCE		226.07	[52]
AChE/ConA/PDA-RGO-AuNP/GCE		54256.27	[66]
rGO/AuNP/NA/SPCE		200	[67]

Repeatability was assessed by measuring the electroactive *current* of CF by chronoamperometry, six times in one day (Figure 3.6A), and a satisfactory %RSD of 3.7 was determined. Reproducibility in the detection of CF was investigated with six different hybrid platforms (Figure 3.6B) ,and a low %RSD of 4.1 was determined. Finally, to investigate the storage stability, six SPCEs/His-RGO/Ag NW/PEDOT:PSS were stored at 4°C for one month, and during this time, the *current*s of oxidation of CF (Figure 3.6C) were measured every week, showing almost stable *current* values (Figure 3.6D).

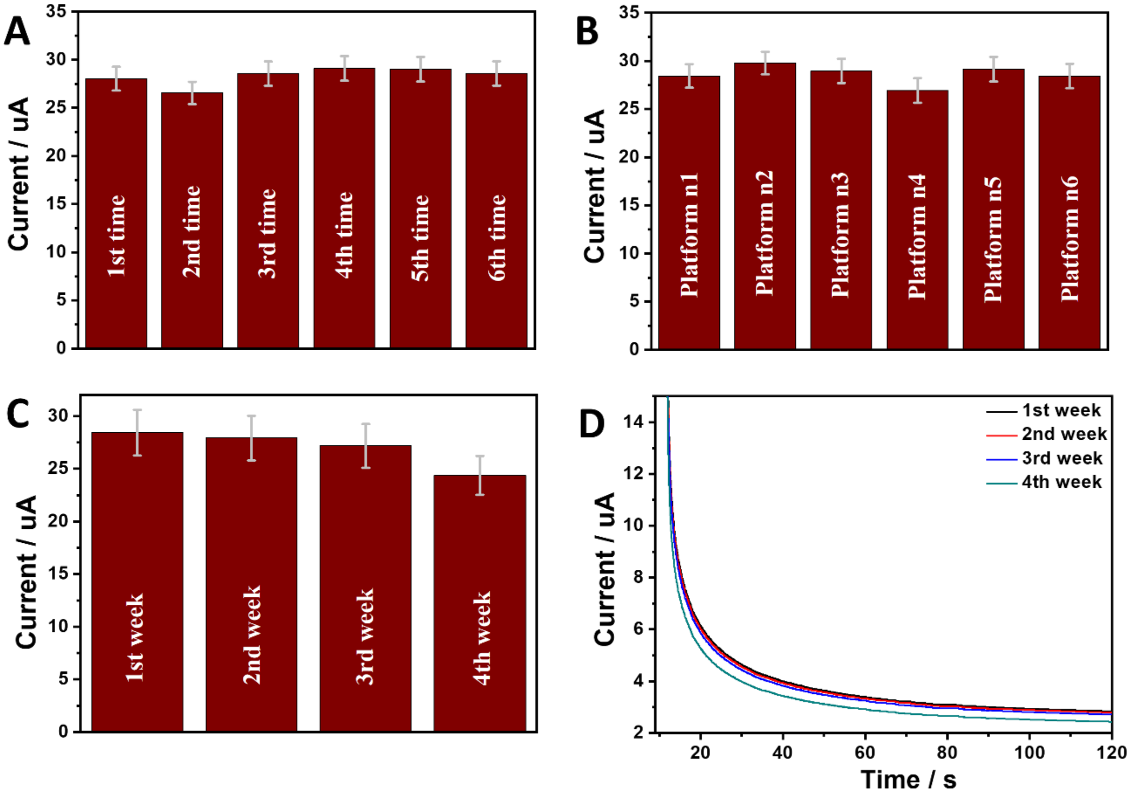

Figure 3.6 Histograms of repeatability (A), reproducibility (B) and storage stability (C) and chronoamperograms (D) recorded at the SPCEs/His-RGO/Ag NW/PEDOT:PSS in 0.1 M PBS buffer (pH 7.4) added by 50 µM of carbofuran

Interference measurements: Possible components of the matrix may affect the analysis of real samples, and the analytical parameters of the method, including LOD, LOQ, repeatability, and reproducibility, thus causing inaccuracy in the measure. Therefore, to investigate the role of interferent species in the detection of CF, DPV analysis was performed by spiking 0.1M PBS solutions at pH 7.4, 50 µM of CF with 5 mM interfering species. Sodium, potassium, magnesium, glucose, ascorbic acid, and uric acid was added as interferents for the CF detection. The results show that the interferent species added in a 100-fold higher concentration do not significantly affect the *current* intensity (Figure 3.7A), thus confirming the high selectivity of the modified electrodes to CF analytes.

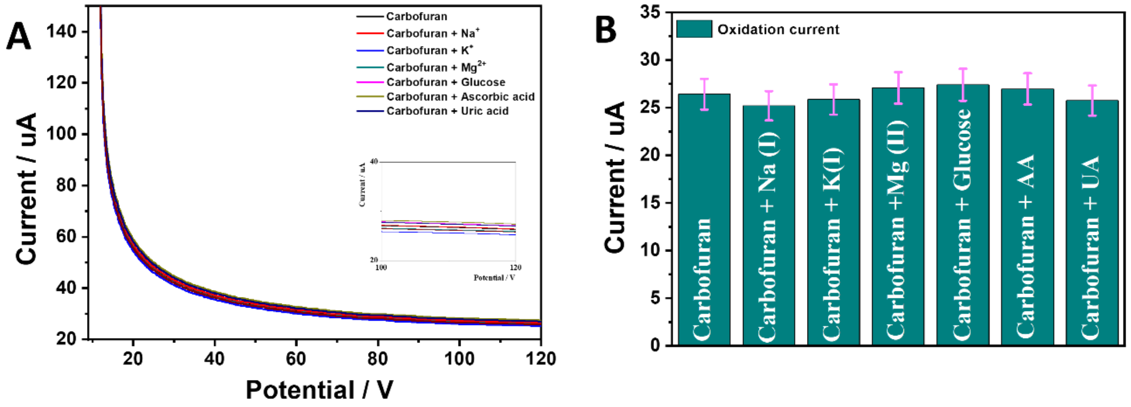

Figure 3.7 DPVs at the SPCEs/His-RGO/Ag NW/PEDOT:PSS in 0.1 M PBS buffer (pH 7.4) added by 50 µM of carbofuran in presence of 5 mM interfering species with 0.05 s modulation time, 0.2 s interval time, 60 mV modulation amplitude, 0.26 V step *potential* and 50 mV s^{-1} scan rate.

Analysis of carbofuran in real water samples: To assess the performance and validate the proposed nanostructured platforms in the analysis of complex real samples, river and tap water samples were analyzed by chronoamperometry (Table 3.4). These experiments were performed by the standard addition method, by analyzing three samples added by three known concentrations of the target analytes, between 20–60 µM range, and the results were reported as mean values obtained by analyzing three aliquots of the same sample (Table 3.4). The recovery rates reported in Table 3.4 point out the reliability of the modified electrodes for the detection of CF in the real water samples.

Table 3.4 Quantification of CF in river and tap water samples.

Samples	**Standard Concentration (µM)**	**Concentration Determined by Chronoamperometry (µM)**	**RSD (%)**	**Apparent Recovery (%)**
Tap water	20	21.7	3.6	108.5
	40	38.3	4.2	95.75
	60	62.9	3.9	104.83
River water	20	19.1	3.7	95.5
	40	42.7	3.9	106.75
	60	59.4	4.2	99.0

3.4 Conclusion

Nanostructured platform formed by disposable screen-printed carbon electrodes (SPCEs), modified by a hybrid nanocomposite based on histidine functionalized RGO sheets, the surface decorated with colloidal Ag NWs (SPCEs/His-RGO/Ag NWs), were tested for the detection of carbofuran. To improve the sensitivity and selectivity of the electrodes, a layer of PEDOT:PSS was deposited (SPCE/His-RGO/Ag NW/PEDOT:PSS) through electrochemical polymerization.

The modified SPCEs demonstrated a limit of detection (LOD) of 17.3 nM for carbofuran, which is below the concentration recommended by the U.S. EPA for drinking water. The SPCE/His-RGO/Ag NW/PEDOT:PSS showed an electroactive activity higher than that of the SPCE/His-RGO/Ag NW, which can be explained by the higher electroactive surface area and higher reversibility in the red/ox processes due to the His, which act as electrical contact, soldering adjacent RGO sheets and as an electron coupling agent in mediating Ag NWs-RGO charge transfers, electroactive properties of the Ag NWs and due to the high electrical conductivity of the polymer. The SPCE/His-RGO/Ag NW/PEDOT:PSS showed a high sensitivity for carbofuran with lowest LODs of 17.3 nM, compared to the literature reported, with relatively good %RSD of repeatability and of reproducibility and good storage stability. The modified electrodes show high selectivity with a %RSD of 3.6% for carbofuran after the addition of interferent species in a concentration 100-fold higher than that of the analyte. Recovery rates between 95.75–108.5% for the detection of carbofuran in real water samples, assessed feasibility of the fabricated platforms for the successful detection of such threats in real samples opening the venue to their use for the determination of other hazardous species.

References

1. Graham, K.Z., *Federal regulation of pesticide residues: a brief history and analysis.* J. Food L. & Pol'y, **2019**. 15: p. 98.
2. Inhalation, D. and A. MOE, *Department of Pesticide Regulation.* **2012**.
3. Wu, X., et al., *Circulating purification of cutting fluid: an overview.* The International Journal of Advanced Manufacturing Technology, **2021**. 117(9): p. 2565-2600.
4. Liu, W., et al., *Ultrasensitive exhaled breath sensors based on anti-resonant hollow core fiber with in situ grown ZnO-Bi2O3 nanosheets.* Advanced Materials Interfaces, **2021**. 8(6): p. 2001978.
5. Tang, X., et al., *Competitive-type pressure-dependent immunosensor for highly sensitive detection of diacetoxyscirpenol in wheat via monoclonal antibody.* Analytical chemistry, **2020**. 92(5): p. 3563-3571.
6. Zhu, H., et al., *Crossover from linear chains to a honeycomb network for the nucleation of hexagonal boron nitride grown on the Ni (111) surface.* The Journal of Physical Chemistry C, **2021**. 125(48): p. 26542-26551.
7. Dobšíková, R., *Acute toxicity of carbofuran to selected species of aquatic and terrestrial organisms.* Plant Protection Science, **2003**. 39(3): p. 103.
8. Gupta, R.C., *Carbofuran toxicity.* Journal of Toxicology and Environmental Health, Part A Current Issues, **1994**. 43(4): p. 383-418.
9. Maheshwaran, S., et al., *Metal oxide-based electrochemical sensors for pesticide detection in water and food samples: a review.* Environmental Science: Advances, **2024**.
10. Bortoli, S. and X. Coumoul, *Impact of Pesticides on Human Health.* Prat. en Nutr, **2018**. 14: p. 18-24.
11. Ruzaidy, N.I.M. and A. Amid, *Heavy metal contamination in vegetables and its detection: A review.* Science Heritage Journal (GWS), **2020**. 4(1): p. 1-5.
12. Zhang, Z., et al., *Metal–organic frameworks (MOFs) based chemosensors/biosensors for analysis of food contaminants.* Trends in Food Science & Technology, **2021**. 118: p. 569-588.
13. Li, H., et al., *Extreme pressure and antiwear additives for lubricant: academic insights and perspectives.* The International Journal of Advanced Manufacturing Technology, **2022**. 120(1): p. 1-27.
14. Gupta, J.K. and S. Gupta, *A comparative study of crowd counting and profiling through visual and non-visual sensors.* Acta Informatica Malaysia, **2019**. 3(1): p. 4-6.
15. Karimi-Maleh, H., et al., *Nanochemistry approach for the fabrication of Fe and N co-decorated biomass-derived activated carbon frameworks: a promising oxygen reduction reaction electrocatalyst in neutral media.* Journal of Nanostructure in Chemistry, **2022**. 12(3): p. 429-439.
16. Nazeer, M., et al., RETRACTED: Theoretical study of MHD electro-osmotically flow of third-grade fluid in micro channel. **2022**, Elsevier.
17. Yang, J., et al., *Development of an enzyme-linked immuno-sorbent assay (ELISA) method for carbofuran residues.* Molecules, **2008**. 13(4): p. 871-881.
18. Abad, A., et al., *Determination of carbaryl, carbofuran and methiocarb in cucumbers and strawberries by monoclonal enzyme immunoassays and high-performance liquid chromatography with fluorescence detection: An analytical comparison.* Journal of Chromatography A, **1999**. 833(1): p. 3-12.
19. Pacioni, N.L. and A.V. Veglia, *Determination of carbaryl and carbofuran in fruits and tap water by β-cyclodextrin enhanced fluorimetric method.* Analytica Chimica Acta, **2003**. 488(2): p. 193-202.
20. Leppert, B.C., et al., *Determination of carbosulfan and carbofuran residues in plants, soil, and water by gas chromatography.* Journal of agricultural and food chemistry, **1983**. 31(2): p. 220-223.
21. Detomaso, A., G. Mascolo, and A. Lopez, *Characterization of carbofuran photodegradation by-products by liquid chromatography/hybrid quadrupole time-of-flight mass spectrometry.* Rapid

Communications in Mass Spectrometry: An International Journal Devoted to the Rapid Dissemination of Up-to-the-Minute Research in Mass Spectrometry, **2005**. 19(15): p. 2193-2202.

22. Rangaswamy, J.R., Y.N. VijayaShankar, and S.R. Prakash, *A simple spectrophotometric method for the determination of carbofuran residues.* Journal of the Association of Official Analytical Chemists, **1976**. 59(6): p. 1276-1278.
23. Pohanka, M., et al., *Carbofuran assay using gelatin based biosensor with acetylcholinesterase as a recognition element.* International Journal of Electrochemical Science, **2013**. 8(1): p. 71-79.
24. Wang, M., et al., *Electrochemical nonenzymatic sensor based on CoO decorated reduced graphene oxide for the simultaneous determination of carbofuran and carbaryl in fruits and vegetables.* Food chemistry, **2014**. 151: p. 191-197.
25. Sun, X., et al., *A label-free electrochemical immunosensor for carbofuran detection based on a sol-gel entrapped antibody.* Sensors, **2011**. 11(10): p. 9520-9531.
26. Mariyappan, V., M. Keerthi, and S.-M. Chen, *Highly selective electrochemical sensor based on gadolinium sulfide rod-embedded RGO for the sensing of carbofuran.* Journal of Agricultural and Food Chemistry, **2021**. 69(9): p. 2679-2688.
27. Tan, X., et al., *Electrochemical sensor based on molecularly imprinted polymer reduced graphene oxide and gold nanoparticles modified electrode for detection of carbofuran.* Sensors and Actuators B: Chemical, **2015**. 220: p. 216-221.
28. Kanoun, O., et al., *A review of nanocomposite-modified electrochemical sensors for water quality monitoring.* Sensors, **2021**. 21(12): p. 4131.
29. Tanwar, S. and D. Mathur, *Graphene-based nanocomposites as sensing elements for the electrochemical detection of pesticides: a review.* Journal of Solid State Electrochemistry, **2021**. 25(8): p. 2145-2159.
30. Ramachandran, R., et al., *A review of the advanced developments of electrochemical sensors for the detection of toxic and bioactive molecules.* Inorganic Chemistry Frontiers, **2019**. 6(12): p. 3418-3439.
31. Hanrahan, G., D.G. Patil, and J. Wang, *Electrochemical sensors for environmental monitoring: design, development and applications.* Journal of environmental monitoring, **2004**. 6(8): p. 657-664.
32. Ivanov, A., et al., *Acetylcholinesterase biosensor based on single-walled carbon nanotubes—Co phtalocyanine for organophosphorus pesticides detection.* Talanta, **2011**. 85(1): p. 216-221.
33. Du, D., et al., *Comparison of pesticide sensitivity by electrochemical test based on acetylcholinesterase biosensor.* Biosensors and Bioelectronics, **2007**. 23(2): p. 285-289.
34. Bilal, S., et al., *An insect acetylcholinesterase biosensor utilizing WO3/g-C3N4 nanocomposite modified pencil graphite electrode for phosmet detection in stored grains.* Food chemistry, **2021**. 346: p. 128894.
35. Qi, J.-f., et al., *A novel acetylcholinesterase biosensor with dual-recognized strategy based on molecularly imprinted polymer.* Sensors and Actuators B: Chemical, **2021**. 337: p. 129760.
36. Bowman, C.A., *Novel Sensing Concept for Organophosphate Monitoring*. **2021**: State University of New York at Albany.
37. Raymundo-Pereira, P.A., et al., *Selective and sensitive multiplexed detection of pesticides in food samples using wearable, flexible glove-embedded non-enzymatic sensors.* Chemical Engineering Journal, **2021**. 408: p. 127279.
38. Gu, C., et al., *Ultrasensitive non-enzymatic pesticide electrochemical sensor based on HKUST-1-derived copper oxide@ mesoporous carbon composite.* Sensors and Actuators B: Chemical, **2020**. 305: p. 127478.
39. Khairy, M., H.A. Ayoub, and C.E. Banks, *Non-enzymatic electrochemical platform for parathion pesticide sensing based on nanometer-sized nickel oxide modified screen-printed electrodes.* Food chemistry, **2018**. 255: p. 104-111.

40. Rhouati, A., M. Majdinasab, and A. Hayat, *A perspective on non-enzymatic electrochemical nanosensors for direct detection of pesticides.* Current Opinion in Electrochemistry, **2018**. 11: p. 12-18.
41. Malik, S., et al., *Nanomaterials-based biosensor and their applications: A review.* Heliyon, **2023**.
42. Yaqub, A., et al., *Efficient preparation of a nonenzymatic nanoassembly based on cobalt-substituted polyoxometalate and polyethylene imine-capped silver nanoparticles for the electrochemical sensing of carbofuran.* ACS omega, **2022**. 7(1): p. 149-159.
43. Morales-Narváez, E., et al., *Graphene-based biosensors: going simple.* Advanced Materials, **2017**. 29(7): p. 1604905.
44. Ding, Q., et al., *Electrochemical detection of heavy metal ions in water.* Chemical communications, **2021**. 57(59): p. 7215-7231.
45. Li, W., et al., *Electrochemistry of individual monolayer graphene sheets.* ACS nano, **2011**. 5(3): p. 2264-2270.
46. Thirumalraj, B., et al., *Rational design and interlayer effect of dysprosium-stannate nanoplatelets incorporated graphene oxide: a versatile and competent electrocatalyst for toxic carbamate pesticide detection in vegetables.* ACS Sustainable Chemistry & Engineering, **2020**. 8(48): p. 17882-17892.
47. Jia, D., et al., *An effective surface design based on a graphene oxide decorated by silver nanoparticles for detection of carbofuran in vegetable samples.* International Journal of Electrochemical Science, **2022**. 17(6): p. 220616.
48. Mphuthi, N., L. Sikhwivhilu, and S.S. Ray, *Functionalization of 2D MoS2 nanosheets with various metal and metal oxide nanostructures: their properties and application in electrochemical sensors.* Biosensors, **2022**. 12(6): p. 386.
49. Yoon, J., et al., *Graphene/MoS2 nanohybrid for biosensors.* Materials, **2021**. 14(3): p. 518.
50. Alagarsamy, S., et al., *An ultrasensitive carbamate pesticide detection sensor based on metal molybdate encapsulated with boron doped reduced graphene oxide nanocomposite.* Colloids and Surfaces A: Physicochemical and Engineering Aspects, **2023**. 673: p. 131830.
51. Haritha, V., S. Sarath Kumar, and R. Rakhi, *Electrochemical Determination of Carbofuran Residues using WS2 Modified Electrodes.* ChemistrySelect, **2024**. 9(33): p. e202402500.
52. Liu, T., et al., *Acetylcholinesterase biosensor based on 3-carboxyphenylboronic acid/reduced graphene oxide–gold nanocomposites modified electrode for amperometric detection of organophosphorus and carbamate pesticides.* Sensors and actuators B: Chemical, **2011**. 160(1): p. 1255-1261.
53. Hashemi, P., et al., *Reduced graphene oxide decorated on Cu/CuO-Ag nanocomposite as a high-performance material for the construction of a non-enzymatic sensor: Application to the determination of carbaryl and fenamiphos pesticides.* Materials Science and Engineering: C, **2019**. 102: p. 764-772.
54. Wang, D., et al., *Single Ag nanowire electrodes and single Pt@ Ag nanowire electrodes: Fabrication, electrocatalysis, and surface-enhanced raman scattering applications.* Analytical chemistry, **2019**. 91(7): p. 4291-4295.
55. Soni, R., M. Soni, and D.P. Shukla, *Emerging techniques and materials for water pollutants detection.* Sensors in Water Pollutants Monitoring: Role of Material, **2020**: p. 277-297.
56. Zheng, X., et al., *A robust electrochemical sensor based on AgNWs@ MoS2 for highly sensitive detection of thiabendazole residues in food samples.* Food Chemistry, **2024**. 433: p. 137304.
57. Naderi, N., et al., *Enhanced optical and electrical stability of thermally carbonized porous silicon.* Materials science in semiconductor processing, **2013**. 16(2): p. 542-546.
58. Solomonenko, A.N., et al., *Adsorptive stripping voltammetric determination of carbofuran in herbs on chromatographic sorbent modified electrode.* Journal of Electroanalytical Chemistry, **2021**. 900: p. 115692.

59. Miyazaki, C.M., et al., *Combining electrochemically reduced graphene oxide and Layer-by-Layer films of magnetite nanoparticles for carbofuran detection.* Journal of Environmental Chemical Engineering, **2020**. 8(5): p. 104294.
60. Mejri, A., et al., *Reduced graphene oxide nanosheets modified with nickel disulfide and curcumin nanoparticles for non-enzymatic electrochemical sensing of methyl parathion and 4-nitrophenol.* Microchimica Acta, **2019**. 186: p. 1-9.
61. Song, Z., et al., *Preparation and electrochemical sensing application of porous conducting polymers.* TrAC Trends in Analytical Chemistry, **2021**. 135: p. 116155.
62. Namsheer, K. and C.S. Rout, *Conducting polymers: a comprehensive review on recent advances in synthesis, properties and applications.* RSC advances, **2021**. 11(10): p. 5659-5697.
63. Ahn, Y., et al., *Exploring Pore Formation and Gas Sensing Kinetics Using Conjugated Polymer–Small Molecule Blends.* ACS Applied Materials & Interfaces, **2024**.
64. Jiang, X., et al., *Functional three-dimensional porous conductive polymer hydrogels for sensitive electrochemiluminescence in situ detection of H2O2 released from live cells.* Analytical chemistry, **2018**. 90(14): p. 8462-8469.
65. Jirasirichote, A., et al., *Voltammetric detection of carbofuran determination using screen-printed carbon electrodes modified with gold nanoparticles and graphene oxide.* Talanta, **2017**. 175: p. 331-337.
66. Li, Y., et al., *Electrochemical determination of carbofuran in tomatoes by a concanavalin A (con A) polydopamine (PDA)-reduced graphene oxide (RGO)-gold nanoparticle (GNP) glassy carbon electrode (GCE) with immobilized acetylcholinesterase (AChE).* Analytical Letters, **2019**. 52(14): p. 2283-2299.
67. Albalawi, I., et al., *Electrochemical synthesis of reduced graphene oxide/gold nanoparticles in a single step for carbaryl detection in water.* Sensors, **2022**. 22(14): p. 5251.

CHAPTER 4

Ag Nanowire-Decorated RGO based Nanocomposites for SERS Detection of Pollutant Molecules on Flexible Substrate.

4.1 Introduction

The contamination of freshwater sources and wastewater by pharmaceutical compounds has become a critical environmental issue, necessitating regular pollutant monitoring to enable effective mitigation strategies. Traditional analytical methods including (gas chromatography/mass spectrometry (GC/MS), atomic absorption spectroscopy (AAS), high-performance liquid chromatography (HPLC) are commonly employed to quantify trace amounts of pharmaceuticals. However, such methods have notable drawbacks: they are costly, time-intensive, often require toxic reagents, and face limitations for *on-site* analysis due to their large size and lack of portability. Furthermore, these techniques typically involve sample preparation steps, such as separation and pre-concentration, which can be particularly time-consuming, especially for polar pharmaceutical compounds [1]. Although advancements such as solid phase microextraction have made some improvements, challenges with detection accuracy persist, underscoring a need for further refinement. Additionally, achieving fast, accurate, and highly sensitive detection of diverse pharmaceuticals within complex matrices remains challenging [1] with high sensitivity, continues to be a significant issue. These limitations point to the need for developing alternative analytical methods that rely on more affordable, simpler instruments suitable for on-site applications.

Raman spectroscopy and surface-enhanced Raman spectroscopy (SERS) have shown significant promise as analytical techniques to address challenges related to sensitivity in molecular detection. SERS-based sensors, in particular, enhance the detection of analyte molecules by amplifying their molecular fingerprints, allowing detection of molecules at trace levels, overcoming sensitivity limitations of conventional Raman spectroscopy, in which signals are typically weak due to the small scattering cross-section of molecules [2, 3].

The enhancement of Raman signals in SERS is attributed to two main mechanisms: electromagnetic enhancement (EM) and chemical or charge-transfer enhancement (CE) [4].

The EM mechanism relies on the surface plasmon resonance (SPR) of metallic nanoparticles (NPs), such as Ag, Au, and Cu, which intensifies the electromagnetic field around the analyte molecules at the nanoparticle surface interface. Because both amplification mechanisms simultaneously enhance the Raman signal, developing substrates that harness both effects has become a major area of interest in SERS research [5].

Significant efforts have been devoted to the fabrication of stable and reusable SERS substrates based on metallic nanostructures capable of providing reproducible and high SERS signal enhancements. Previous reports indicate that Ag NPs [6] are particularly favourable for SERS applications compared to Au and Cu NPs, owing to their superior plasmonic characteristics and relative ease of synthesis [7]. However, challenges remain with the stability and reproducibility of Ag-based SERS signals, as Ag NPs are prone to oxidation, aggregation, and dissolution upon exposure to atmospheric oxygen and water vapor [8]. To mitigate these issues, Ag NPs can be coated with protective layers that shield them from oxidation without impairing their SERS activity. Additionally, the enhancement factor of Ag nanostructures can be further increased by coupling their SPR with other nanomaterials, combining their EM effect with CE mechanisms [4]. Graphene-based materials, including single-layer graphene and its derivatives, have gained attention as SERS substrates due to their potential for enhancing Raman signals [9]. Graphene oxide (GO) and reduced graphene oxide (RGO) have been, in fact, popular for such applications, given their high surface area and chemical reactivity, which support the development of a wide range of functional nanocomposites with (bio)molecules and nanostructures, exhibiting interesting chemical physical functionalities.

GO and RGO are well-suited for SERS substrates due to their fluorescence quenching abilities, high adsorption capacity for analytes through π-π stacking and hydrophobic interactions, and the stability of their SERS signals [10] when used as monolayers, stability attributed to charge-transfer-induced mechanisms [9] [11]. These properties have led to recent research on fabricating GO/RGO composites with noble metal NPs, aiming to enhance SERS performance by merging CE and EM effects [11, 12].

For example, L. Zhang et al. developed a GO-based sandwich nanostructure embedded with Ag nanoparticles (NPs) using self-assembly technique, achieving remarkable sensitivity in pesticide monitoring due to the creation of multiple hot spots on the surface [10] [13][16]. Similarly, W. Fan et al. explored the impact of morphology control on Ag NPs decorating GO sheets, achieving ultrasensitive single-particle SERS detection. Their work demonstrated significant Raman signal enhancement using hybrid nanostructures fabricated with Ag octahedral particles [13] [11, 12].

Particularly interesting is the integration of SERS active materials into natural substrates such as cotton, silk and wool fabrics, which show strong potential as supporting scaffolds in sensor development [7] [10, 14]. These natural materials exhibit key characteristics, including surface reactivity, mechanical flexibility, biodegradability, and biocompatibility, making them highly suitable for producing sustainable, wearable, and flexible sensors. However, despite their potential, there has been limited investigation into the application of GO or RGO as SERS [12] substrates on cellulose-based materials like paper and cotton.

In this study, we introduce a facile method for fabricating a novel, flexible and wearable SERS sensor, by modifying hydrophobic paper with histidine functionalized RGO sheets, decorated with Ag nanowires (His-RGO/Ag NWs). The hybrid nanocomposite was synthesized by modifying the self-seeding polyol approach reported for synthesizing neat Ag NWs.

The method involves reducing the $AgNO_3$ precursor with ethylene glycol (EG) in the presence of polyvinylpyrrolidone (PVP) and sodium chloride (NaCl) salt, promoting the nucleation and growth of NWs onto the functionalities of the His-RGO platform. In this synthesis, EG serves as both a reducing agent and a green solvent for the reaction mixture, NaCl maintains a low concentration of Ag atoms in the solution, thereby controlling thermodynamics and promoting the unidirectional growth of Ag NWs. PVP acts as a structure-directing agent, assisting in the preferred axis growth of Ag clusters, stabilizing them to prevent aggregation, and enabling dispersion of the nanocomposite in water or alcohols [55].

Both RGO sheets and Ag NWs offer intrinsic mechanical flexibility, making them ideal for modifying flexible substrates for wearable devices and sensors. The paper substrates were modified by the His-RGO/Ag NWs nanocomposite, and their SERS activity was tested for detecting typical SERS-active molecules as well as pharmaceutical pollutant molecules, also against paper substrates modified by neat Ag NWs.

To optimize SERS performance, the deposition of His-RGO/Ag NWs on hydrophobic paper was done by using a dip-coating method and finally improvement in SERS performance was achieved by increasing the number of drop-casting depositions.

This work has been done in collaboration with the FunNanobio Group of the Departamento de Química Física y CINBIO Universidade de Vigo, led by Jorge Perez Juste.

4.2 Materials and methods

4.2.1 Chemicals and materials

1-naphthalenethiol (1-Nat), rhodamine 6G (R6G), benzo[a]pyrene and potassium iodide (KI), dodecenylsuccinic anhydride (DDSA) and propranolol hydrochloride (PRNL) were purchased from Sigma-Aldrich. Milli-Q water was used for the preparation of all aqueous solutions (18.2 MΩ·cm organic carbon content ≥ 4 µg L^{-1}) achieved by a Milli-Q gradient A-10 system.

4.2.2 Functionalization of chromatographic paper.

A 0.5% (w/v) dodecenylsuccinic anhydride (DDSA) solution in 1-hexanol was prepared by weighing 789.6 mg of DDSA into 150 mL of 1-hexanol. The solution was stirred under a fume hood at 50°C for 1 h [15].

Subsequently, a sheet of chromatography paper (Whatman 1CHR No. 3001-861) was divided into four sections, and one piece was immersed in a glass Petri dish containing 50 mL of DDSA solution for 5 min. Following this, the paper was transferred to a separate glass container and placed in a thermostatically controlled oven set at 160°C for an additional 5 min to ensure complete solvent evaporation. This process was repeated twice.

The success of the surface modification was assessed by placing three individual 2 μL water droplets on the treated paper. If each droplet remained intact and evaporated without being absorbed, the functionalization was considered effective. Under these conditions, the water contact angle was estimated to be approximately 110°.

4.2.3 Preliminary Surface-Enhanced Raman Scattering (SERS) study of 1-NAT, R6G and benzo[a]pyrene.

The deposition of His-RGO/Ag NWs and Ag NWs onto hydrophobic paper was optimized by drop-casting four different volumes, 1, 4, 8, and 16 μl, of both the materials onto four separate hydrophobic papers, adding 1 μl at a time. Following this deposition, a 4 μl of the model molecule 1-NAT was applied to each sample, and SERS measurements were performed using a 785 nm laser with 5% power, a 10 s acquisition time, 1 accumulation, and a 20x objective.

4.2.4 Estimation of the limit of detection (LOD) of 1-NAT and R6G

To evaluate SERS performance, 4 μl of His-RGO/Ag NWs and Ag NWs were deposited onto hydrophobic paper by drop-casting, using 1-NAT and R6G as target molecules for testing. SERS measurements of 1-NAT and R6G were carried out using a 785 nm laser at 10% power and a 633 nm laser at 5% power, respectively, both with acquisition time of 10 s, 1 accumulation, and a 20x objective.

LOD for the target molecules was assessed from three aqueous solutions of different concentrations (10^{-5} M, 10^{-6} M, and 10^{-7} M), achieved diluting a stock solution in ethanol at a concentration of 10^{-4} M.

4.2.5 Characterization techniques

UV-Vis-NIR Absorption Spectroscopy: UV-Vis-NIR absorption spectra were collected by a VARIAN CARY® 5000 UV-Vis-NIR Spectrophotometer.

Transmission Electron Microscopy (TEM): A JEOL JEM 1011 electron microscope, operating at an acceleration voltage of 100 kV and equipped with a CCD camera, was used. For the analyses, the samples were prepared by dipping a 400-mesh copper TEM grid, coated with carbon, into diluted solutions. Size distribution of Ag nanostructures was analyzed using ImageJ software.

Raman Spectroscopy: Raman spectra were recorded with a LabRAM HR Horiba-Jobin Yvon spectrometer using a continuous 532 nm laser excitation source, operating at low power (1 mW) to prevent sample damage.

Fourier Transform Infrared Spectroscopy with Attenuated Total Reflectance (FTIR-ATR): Infrared spectra (4000-600 cm^{-1}) were recorded with a Varian 670 FTIR spectrometer equipped with a DTGS (Deuterated Triglycine Sulfate) detector at a spectral resolution of 4 cm^{-1}. A 2 mm diameter diamond microprism was used as the internal reflective element

Field Emission Scanning Electron Microscopy (FE-SEM): FE-SEM measurements were performed by a Zeiss Sigma microscope (Carl Zeiss Co., Oberkochen, Germany) operating in the range of 0.5–20 KV and equipped with an in-lens secondary electron detector and an INCA Energy Dispersive Spectroscopy (EDS) detector. Samples were mounted onto stainless-steel sample holders by double-sided conductive carbon tape and grounded by silver paste.

4.3 Results and discussion

4.3.1 SERS measurements

The achieved His-RGO/Ag NWs hybrid nanocomposite combines the plasmonic properties of Ag NWs with the high surface area, chemical reactivity, and Raman signal enhancement capability of His-RGO. His-RGO also serves to stabilize Ag NWs against oxidation by acting as an oxygen and moisture barrier [16]. Thus, the nanocomposite was here preliminarily tested for the SERS detection of Raman active reference molecules and then of pharmaceuticals. For purpose of comparison, the same studies have been performed on neat Ag NWs working in the same experimental conditions.

Three model molecules with distinct chemical structures namely R6G, 1-NAT and benzo[a]pyrene were chosen as analytes, using different concentrations of analyte solutions (10^{-5} M, 10^{-6} M, and 10^{-7} M). The choice of analyte structures was guided by their role in influencing chemical affinity with the SERS substrate [17, 18] a key factor for signal enhancement. Histidine enhances SERS signals via a distance-dependent charge transfer from graphene to adsorbed molecules, suggesting that stronger analyte adsorption onto the His-RGO sheets could lead to increased signal intensity [19]. Hydrophobic chromatographic paper (Figure 4.1) was chosen as a substrate for the SERS active materials in these measurements, because it presents a low fluorescence signal and a low Raman scattering, providing a cleaner background for analysis [15].

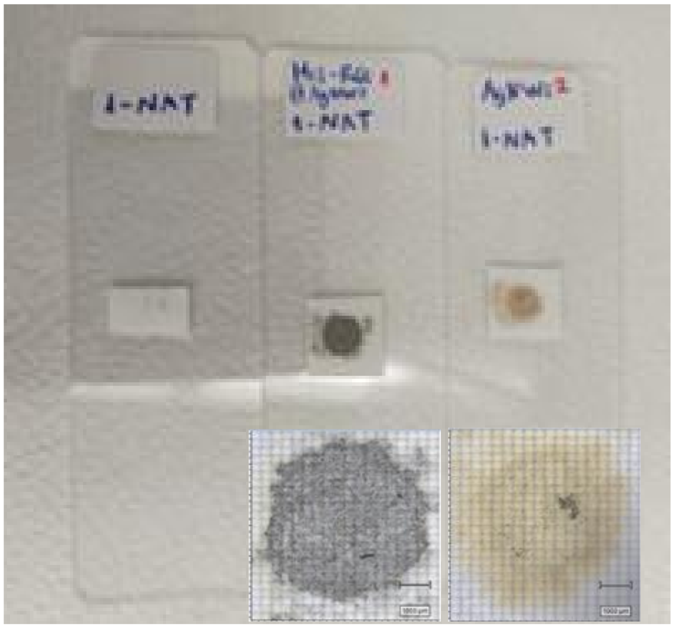

Figure 4.1 Digital photograph images of hydrophobic paper modified by drop casting 1-Nat, His-RGO/Ag NWs and Ag NWs.

Besides, the paper is composed of pure cellulose, being free from industrial additives and possible contaminants that could interfere with the SERS detection [15].

Hydrophobicity was achieved by modifying with DDSA, as reported in the experimental section of this chapter. DDSA is a widely used sizing agent due to its capability of promoting formation of a water *resistance* surface on paper [15]. The anhydride group of DDSA reacts with the hydroxyl groups of cellulose by esterification and enables grafting of aliphatic chains on the cellulose surface which reduces its wettability [15] .

4.3.2 SERS Study for 1-NAT, R6G and benzo[a]pyrene sensing

4.3.2.1 Rhodamine-6G (R6G)

R6G is a fluorescent dye, commonly used as a water tracer to study flow rates and directions, also finds applications in biotechnology, including fluorescence microscopy, flow cytometry, fluorescence correlation spectroscopy, and SERS.

In this study, the SERS properties of R6G adsorbed on His-RGO/Ag NWs and on net Ag NWs, both transferred onto paper substrates, were evaluated using laser excitations at 633 nm and 785 nm. The comparison of the resulting SERS spectra demonstrated optimal signal enhancement with the 633 nm laser excitation (Figure 4.2, green line).

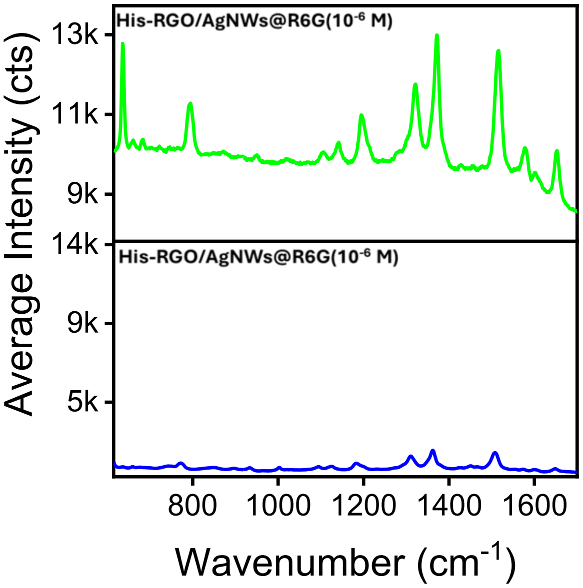

Figure 4.2 SERS spectrum of His-RGO/AgNWs@R6G acquired using a 633 nm laser line (green line) and 785 nm laser line (blue line), at 5% power, acquisition time of 10 s, 1 accumulation, and a 20x objective

No SERS signal was observed from R6G deposited solely onto His-RGO (data not reported). In contrast, the SERS spectra for R6G adsorbed onto both His-RGO/Ag NWs and Ag NWs displayed characteristic peaks at 1322, 1371, 1516, 1576, 1601, and 1652 cm^{-1} (Figure 4.3, panel B, green line, and panel A), which are assigned to the aromatic -C-C- stretching vibrations observed in the Raman spectra of R6G [12].

Panel B of Figure 4.3 (blue line) showed that the SERS spectrum of His-RGO/Ag NWs reports a shift in the peaks corresponding to the D and G bands of RGO at 1366 and 1637 cm^{-1}, respectively compared to those observed in the Raman spectrum of His-RGO/Ag NWs at 1349 and 1582 cm^{-1}, respectively (Figure 2.2 D). This shift likely arises from the change in laser excitation wavelength from 532 nm in the Raman measurements to 633 nm in SERS. This phenomenon occurs because the different energy of the incident laser resonates with different vibration modes of the sample molecules.

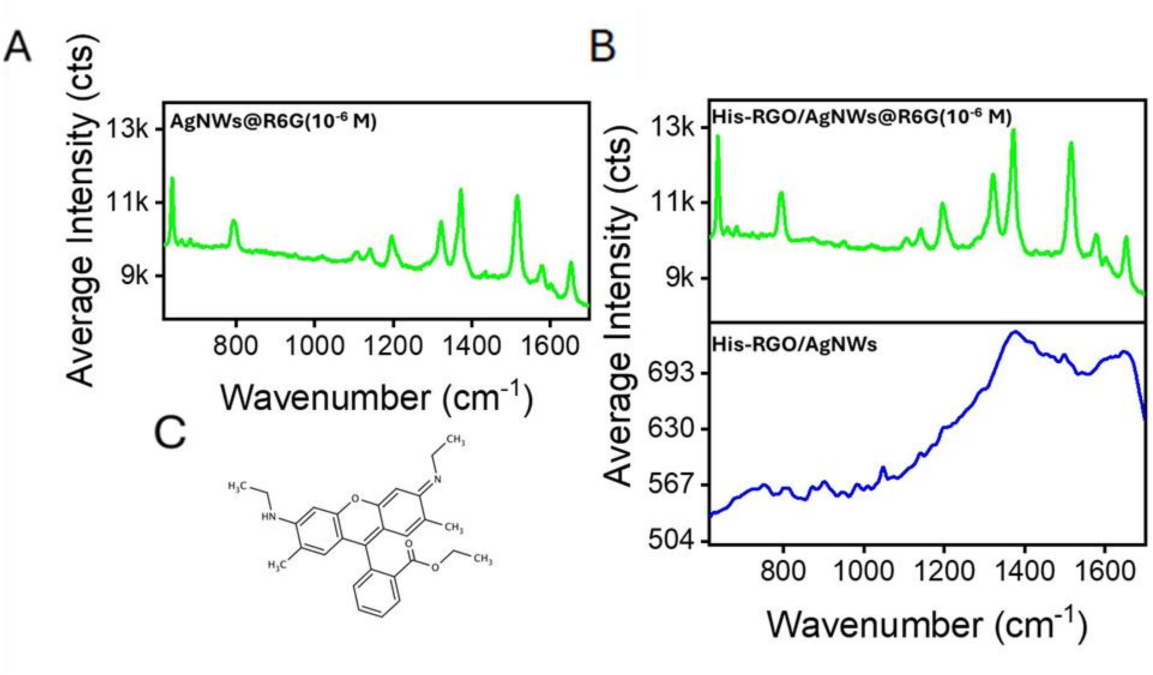

Figure 4.3 SERS spectrum of (A) AgNWs@R6G, (B) His-RGO/AgNWs@R6G (green line) and His-RGO/AgNWs (blue line). (C) Molecular structure of R6G. All SERS experiments were conducted with a 633 nm laser line at 5% power, an acquisition time of 10 s, 1 accumulation, and a 20x objective, respectively.

The SERS intensity of R6G peaks was higher on His-RGO/Ag NWs than on neat Ag NWs, indicating a synergistic enhancement effect provided by the Ag nanostructures and the RGO sheets. Since His-RGO alone did not produce a detectable SERS signal, the enhancement is attributed to the Ag NWs and the role of the His-RGO substrate. With its extensive surface area and aromatic structure, His-RGO supports the chemical adsorption of R6G molecules near the Ag NWs hot spots, helping to quench fluorescence emission and reduce background noise, thus improving the signal quality of R6G in SERS applications [11].

4.3.2.2 1-Naftalenthiol (1-Nat)

The SERS properties of 1-Nat upon deposition onto the His-RGO/Ag NWs nanocomposite and onto the Ag NWs, transferred onto hydrophobic paper, were comprehensively analysed under three laser excitation wavelengths (532, 633, and 785 nm). Among these, the 785 nm excitation produced the highest signal enhancement for 1-Nat.

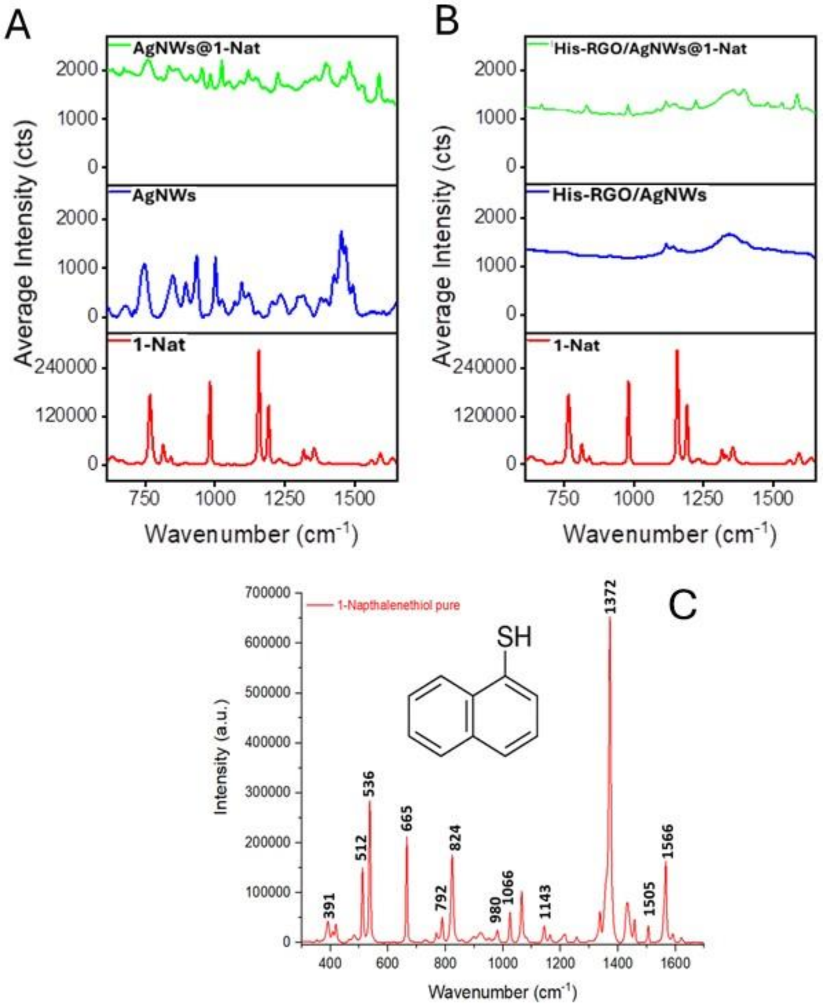

Figure 4.4 SERS spectrum of (A) AgNWs@1-Nat (green line), Ag NWs (blue line) and of 1-Nat (red line), (B) His-RGO/AgNWs@1-Nat (green line), His-RGO/Ag NWs (blue line), and 1-Nat (red line). C) Characteristic Raman spectrum of 1-Nat. All SERS experiments were conducted with a 785 nm laser line at 5% power, acquisition time of 10 s, 1 accumulation, and a 20x objective.

In the SERS spectrum of the Ag NWs (Figure 4.4, panel A blue line) [20], several distinct peaks appear at approximately 896, 1337, 1395, and 1466 cm^{-1}, corresponding to the stretching vibrations of PVP, specifically its C-N, C-C, and Ag-O bonds, attributed to PVP's coordination with the Ag NWs. Additionally, peaks at 1451 and 1668 cm^{-1}, likely associated with C-N ring and C=O bond vibrations, were identified [21].

The SERS spectrum of the nanocomposite (Figure 4.4, panel B blue line) revealed a double peak at 1116 and 1142 cm^{-1}, also present in the Ag NWs spectra, attributed to DSSA functionalization on the paper substrate [15]. The SERS spectrum of the His-RGO/Ag NWs sample (Figure 4.4 panel B blue line) shows a shift in the peaks corresponding to the D and G bands of His-RGO to 1345 and 1550 cm^{-1}, compared to those observed in its Raman spectrum at 1349 and 1582 cm^{-1} (Figure 2.2 D). Further, SERS peaks were observed at 753, 860 and 945 cm^{-1}, that can be ascribed to the vibrational modes of PVP, specifically the N-C=O band vibration of the in-plane pyrrolidone ring breathing, the C-N stretching vibration, the weak ring CH_2 twist and the in-plane C-H band vibration. These peaks are shifted with respect to the Raman peaks of neat PVP due to the coordination to the Ag NWs surface (Figure 4.4 panel B blue line).

The SERS spectra of 1-Nat deposited onto the nanocomposite showed the characteristics peaks at 833 and 981 cm^{-1} that are due to its ring breathing, at 672 and 753 cm^{-1} due to its ring deformation, and at 1066 and 1143 cm^{-1} due to the C-H bending. The latter two peaks are merged with the peaks at 1116 and 1142 cm^{-1}, which are also observed in the SERS spectra of His-RGO/Ag NWs and Ag NWs, likely due to interactions with the hydrophobic paper substrate (Figure 4.4 panel B green line) [21].

Further some Raman bands of 1-Nat on His-RGO/Ag NWs, associated with ring stretching at 1372, 1505, and 1584 cm^{-1} (Figure 4.4 panel C), are shifted in the SERS spectrum at 1392, 1531, and 1584 cm^{-1} (Figure 4.4 panel B). The bands at 1392 and 1531 cm^{-1} overlap with RGO's D and G bands at 1345 and 1550 cm^{-1}, resulting in a noticeable shift.

The most striking observation is that the SERS spectra of 1-Nat on His-RGO/Ag NWs and Ag NWs showed a higher relative intensity peak at 1584 cm^{-1} compared to those obtained from pure 1-Nat, leading to the selection of this peak as a reference in further analyses.

4.3.2.3 Benzo[a]pyrene

The SERS properties of benzo[a]pyrene deposited onto His-RGO/Ag NWs and Ag NWs on paper substrates were examined using multiple laser line excitations (532, 633, and 785 nm). In these analyses, the characteristic SERS spectrum of benzo[a]pyrene was not observed for the molecule on the nanocomposite across the different laser wavelengths tested (data not shown). This absence of signal is attributed to benzo[a]pyrene's likely chemical affinity with RGO, facilitated by its aromatic rings but not with Ag NWs. These findings indicate that His-RGO alone is not SERS-active and that SERS signals are only detectable for molecules like R6G and 1-Nat, which contain functional groups capable of binding directly to the Ag NWs surface.

4.3.3 Limit of detection (LOD) determination for 1-Nat and R6G for His-RGO/Ag NWs and Ag NWs

To evaluate the sensitivity of the His-RGO/Ag NWs and Ag NWs SERS substrates toward 1-Nat and R6G molecules and to estimate their limits of detection (LODs), the intensity versus concentration graphs were plotted for the characteristic peaks at 1584 cm⁻¹ for 1-Nat and 1365 cm⁻¹ for R6G (Figure 4.5, panel C, and Figure 4.6, panel C, respectively).

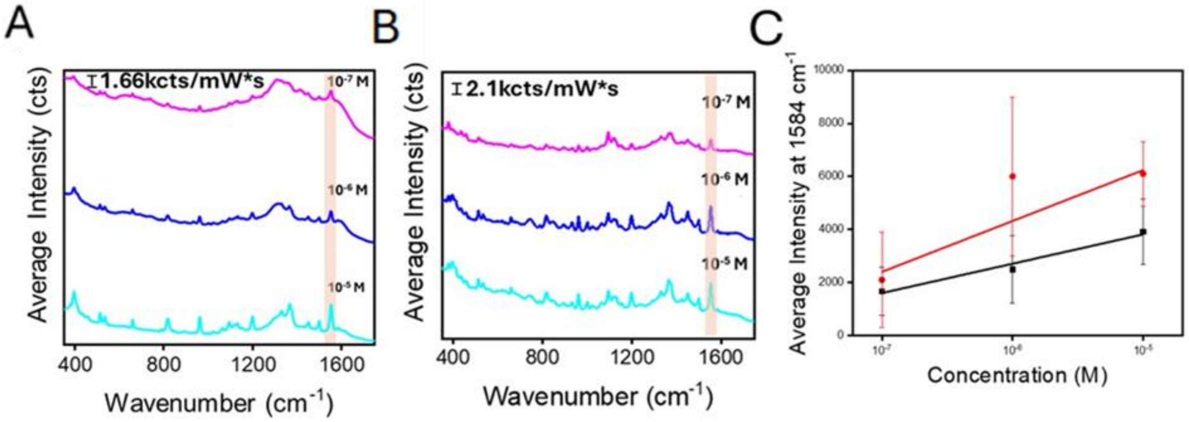

Figure 4.5 (A) SERS spectrum of His-RGO/AgNWs@1-Nat acquired for three aqueous solutions at different concentrations (10^{-5} M, 10^{-6} M, and 10^{-7} M) and (B) of AgNWs@1-Nat (C) Average SERS intensity measured at 1584 cm^{-1} vs the 1-Nat concentration for His-RGO/Ag NWs samples (black line) and AgNWs samples (red line). SERS measurements were performed with a 785 nm laser line at 10% power, acquisition time of 10 s, 1 accumulation, and a 20x objective.

In the SERS spectra of 1-Nat, the intensity of the 1584 cm⁻¹ peak decreases with concentration on both the nanocomposite and Ag NWs substrates (Figure 4.5, panel B). This trend is further reflected in the intensity versus concentration plots (Figure 4.6, panel C, with the black line for the nanocomposite and the red line for Ag NWs). Notably, at higher concentrations, the peak intensity is greater on the Ag NWs substrate (Figure 4.5, panels B-C, red line) compared to the nanocomposite (Figure 4.5, panels A-C, black line). This is because 1-Nat undergoes a sulphur-metal bond with the Ag NWs surface [22], enhancing its interaction with the NWs hotspots and hence increasing its SERS signals.

In case of the nanocomposite, the Ag NWs are likely spaced farther apart due to their attachment to histidine functionalities on the RGO sheets, which disrupts alignment along the longitudinal axis [23]. This structural difference reduces the electromagnetic field intensity at the Ag NW hotspots, consequently decreasing the SERS signal.

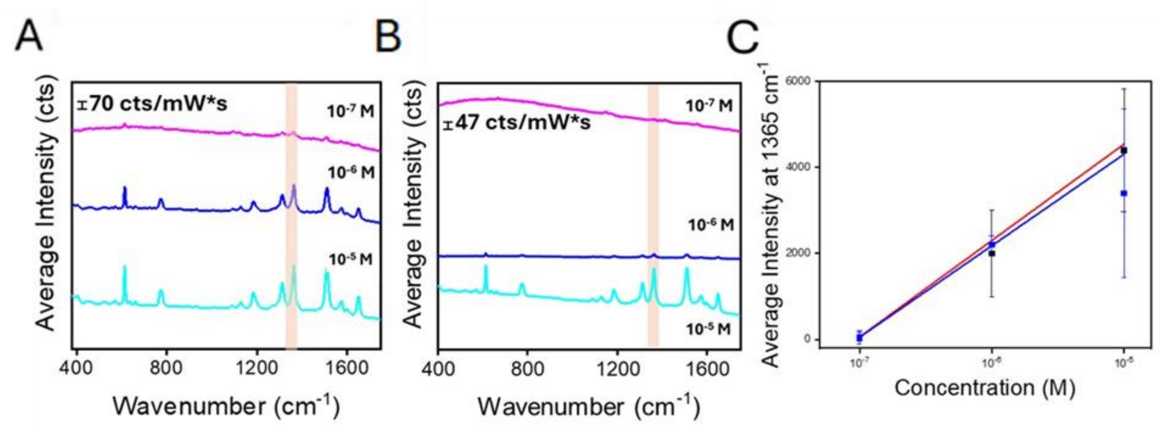

Figure 4.6 SERS spectrum of (A) His-RGO/AgNWs@R6G acquired for three aqueous solutions at different concentrations (10^{-5} M, 10^{-6} M, and 10^{-7} M) and (B) AgNWs@R6G. (C) Average SERS intensity measured at 1365 cm^{-1} vs the R6G concentration for His-RGO/Ag NWs (red line) and Ag NWs (blue line). SERS measurements were performed with a 633 nm laser line at 5% power, an acquisition time of 10 s, 1 accumulation, and a 20x objective.

Similarly, for R6G, the intensity of its 1365 cm^{-1} peak diminishes with decreasing concentration on both the nanocomposite and Ag NWs substrates (Figure 4.6, panel B). This behaviour is also confirmed by the intensity versus concentration plots (Figure 4.6, panel C, with the black line for the nanocomposite and the red line for Ag NWs). This is because R6G exhibits chemical affinity not only towards Ag, but also towards RGO. R6G, in fact, is a molecule with aromatic rings capable of interacting with His-RGO through aromatic π-π stacking and it also possesses nitrogen-containing groups that interact with Ag NWs, forming a strong chemical bond with the nanocomposite (Figure 4.6).

Both molecules 1-Nat and R6G, reach a limit of detection (LOD) of 10^{-7} M on both His-RGO/Ag NWs and Ag NWs substrates. However, as shown in Figure 4.5 and Figure 4.6, distinct chemical interactions and substrate compositions lead to slight differences in intensity trends between the two molecules, both when compared with each other and across the two substrates [18].

4.4 Conclusion

In this study, a novel hybrid nanocomposite His-RGO/Ag NWs was evaluated as a SERS substrate and compared against neat Ag NWs. The materials were tested with target molecules of differing chemical structures, including 1-naphthalenethiol (1-Nat), rhodamine 6G (R6G) and benzo[a]pyrene.

The findings showed that 1-Nat, possessing a high affinity for silver, exhibited strong SERS signals on both substrates. R6G generated even more intense SERS peaks compared to 1-Nat on both the His-RGO/Ag NWs and the neat Ag NWs. In contrast, benzo[a]pyrene produced no detectable SERS signal. This lack of response was attributed to the molecule's absence of functional groups with an affinity for silver. Although it interacts with RGO through aromatic rings, no SERS signal was produced, because RGO itself was demonstrated not SERS-active.

This study demonstrates that the His-RGO/Ag NWs hybrid nanocomposite is a promising substrate for SERS detection of molecules with specific chemical affinities, highlighting its potential for diverse analytical applications.

References

1. Muntean, C.M., et al. *Gold vs. Silver Colloidal Nanoparticle Films for Optimized SERS Detection of Propranolol and Electrochemical-SERS Analyses*. Biosensors, **2023**. 13, DOI: 10.3390/bios13050530.
2. Roschi, E., et al. *Surface-Enhanced Raman Spectroscopy for Bisphenols Detection: Toward a Better Understanding of the Analyte–Nanosystem Interactions*. Nanomaterials, **2021**. 11, DOI: 10.3390/nano11040881.
3. Li, A., et al., *A SERS-active sensor based on heterogeneous gold nanostar core–silver nanoparticle satellite assemblies for ultrasensitive detection of aflatoxinB1.* Nanoscale, **2016**. 8(4): p. 1873-1878.
4. Chen, B., et al., *Tuning surface-enhanced Raman scattering activity of silver nanowires.* Optik, **2021**. 244: p. 167537.
5. Wang, L., et al., *SERS-based test strips: Principles, designs and applications.* Biosensors and Bioelectronics, **2021**. 189: p. 113360.
6. Pilot, R. and M. Massari, *Silver nanoparticle aggregates: Wavelength dependence of their SERS properties in the first transparency window of biological tissues.* Chemical Physics Impact, **2021**. 2: p. 100014.
7. Yang, J., et al., *Flexible and reusable SERS substrate for rapid conformal detection of residue on irregular surface.* Cellulose, **2021**. 28(2): p. 921-936.
8. Rycenga, M., et al., *Controlling the Synthesis and Assembly of Silver Nanostructures for Plasmonic Applications.* Chemical Reviews, **2011**. 111(6): p. 3669-3712.
9. Olar, G.C., et al., *SERS-active substrates based on graphene oxide or reduced graphene oxide and silver nanoparticles.* Materials Today: Proceedings, **2020**.
10. Zhang, D., et al., *Advances in flexible surface-enhanced Raman scattering (SERS) substrates for nondestructive food detection: Fundamentals and recent applications.* Trends in Food Science & Technology, **2021**. 109: p. 690-701.
11. Nair, A.K., et al., *Multifunctional nitrogen sulfur co-doped reduced graphene oxide – Ag nano hybrids (sphere, cube and wire) for nonlinear optical and SERS applications.* Carbon, **2018**. 132: p. 380-393.
12. Naqvi, T.K., et al., *Silver nanoparticles decorated reduced graphene oxide (rGO) SERS sensor for multiple analytes.* Applied Surface Science, **2019**. 478: p. 887-895.
13. Shiohara, A., Y. Wang, and L.M. Liz-Marzán, *Recent approaches toward creation of hot spots for SERS detection.* Journal of Photochemistry and Photobiology C: Photochemistry Reviews, **2014**. 21: p. 2-25.
14. Bhattacharjee, S., et al., *Nanoparticles incorporated graphene-based durable cotton fabrics.* Carbon, **2020**. 166: p. 148-163.
15. Godoy, N.V., et al., *Ultrasensitive inkjet-printed based SERS sensor combining a high-performance gold nanosphere ink and hydrophobic paper.* Sensors and Actuators B: Chemical, **2020**. 320: p. 128412.
16. Li, X., et al., *Silver nanoparticles protected by monolayer graphene as a stabilized substrate for surface enhanced Raman spectroscopy.* Carbon, **2014**. 66: p. 713-719.
17. Carrasco-Flores, E.A., et al., *Vibrational spectra and surface-enhanced vibrational spectra of 1-nitropyrene.* Appl Spectrosc, **2004**. 58(5): p. 555-61.
18. Liu, X., et al., *Functionalizing metal nanostructured film with graphene oxide for ultrasensitive detection of aromatic molecules by surface-enhanced Raman spectroscopy.* ACS Appl Mater Interfaces, **2011**. 3(8): p. 2944-52.
19. Amicucci, C., et al., *Cost Effective Silver Nanowire-Decorated Graphene Paper for Drop-On SERS Biodetection.* Nanomaterials (Basel), **2021**. 11(6).

20. Zhang, T., Y. Zhao, and K. Wang *Polyimide Aerogels Cross-Linked with Aminated Ag Nanowires: Mechanically Strong and Tough*. Polymers, **2017**. 9, DOI: 10.3390/polym9100530.
21. Xu, S., X. Cao, and Y. Zhou, *Polyvinylpyrrolidine-functionalized silver nanoparticles for SERS based determination of copper(II).* Microchimica Acta, **2019**. 186(8): p. 562.
22. Sun, F., et al., *Multi-functional, thiophenol-based surface chemistry for surface-enhanced Raman spectroscopy.* Chem Commun (Camb), **2017**. 53(33): p. 4550-4561.
23. Goh, M.S., et al., *A Chemical Route To Increase Hot Spots on Silver Nanowires for Surface-Enhanced Raman Spectroscopy Application.* Langmuir, **2012**. 28(40): p. 14441-14449.

CHAPTER 5

Conclusions

This thesis systematically investigates the synthesis and optimization of a novel hybrid nanocomposite comprising RGO sheets functionalized with histidine (His-RGO), and subsequently decorated with Ag nanowires (NWs). Through precise control over the size and morphology of the Ag nanostructures anchored onto the His-RGO platform, achieved by fine-tuning key experimental parameters, the resulting His-RGO/Ag NWs nanocomposites have been effectively tailored for applications in two key technological fields: (i) electrochemical sensors for carbofuran detection and (ii) surface-enhanced Raman scattering (SERS) substrates for drug detection.

The physicochemical properties of the hybrid nanocomposites were carefully tailored by optimizing critical synthesis parameters, including concentration of Ag precursor, pH of the reaction medium, and selection of suitable reducing agents and stabilizers. Adjusting these variables allowed for precise engineering of the material's functionalities, enabling enhanced, application-specific performance in the targeted domains.

Electrochemical sensor based on screen printed carbon electrodes modified by His-RGO/Ag NWs, were tested for the detection of carbofuran. To improve the sensitivity and selectivity of the electrodes, a layer of PEDOT:PSS was deposited onto the SPCE/His-RGO/Ag NW, through electrochemical polymerization. The achieved SPCE/His-RGO/Ag NW/PEDOT:PSS showed a high sensitivity for carbofuran with LODs of 17.3 nM among the lowest reported in literature for nanocomposites based on metal NPs and graphene derivatives, with relatively good %RSD of repeatability, reproducibility and good storage stability.

Finally, the His-RGO/Ag NW hybrid nanocomposite demonstrated high efficacy as a SERS substrate for the sensitive detection of model SERS molecules like 1-naftol, rhodamine 6G (R6G), benzo[a]pyrene. The controlled formation of Ag NWs on the RGO sheets significantly enhanced the SERS signal, highlighting the material's potential for application in flexible sensors designed for environmental monitoring and drug detection.

In summary, this work demonstrated that precise optimization of the synthesis parameters for the His-RGO/Ag nanocomposite enabled the development of a versatile material suitable for applications also onto on flexible, cellulose-based substrates, across diverse fields, such as healthcare and sensor technology. The findings emphasize the significant potential of RGO-based hybrid nanocomposites in advancing sustainable nanotechnology solutions across various disciplines. Future research could be focused on exploring additional functionalities of the nanocomposite material to extend its applicability across a broader range of technology fields with particular focus on aerospace sector.